

University of Alberta

Grid Design and Scale up of Geological Heterogeneity

by

Seyedehfatemeh Razavi

A thesis submitted to the Faculty of Graduate Studies and Research
in partial fulfillment of the requirements for the degree of

Master of Science

in

Mining Engineering

Department of Civil and Environmental Engineering

©Seyedehfatemeh Razavi

Fall 2013

Edmonton, Alberta

Permission is hereby granted to the University of Alberta Libraries to reproduce single copies of this thesis and to lend or sell such copies for private, scholarly or scientific research purposes only. Where the thesis is converted to, or otherwise made available in digital form, the University of Alberta will advise potential users of the thesis of these terms.

The author reserves all other publication and other rights in association with the copyright in the thesis and, except as herein before provided, neither the thesis nor any substantial portion thereof may be printed or otherwise reproduced in any material form whatsoever without the author's prior written permission

In the Name of God, the Most Compassionate, the Most Merciful

“The acquisition of knowledge is a duty incumbent on every male and female.”

Prophet Muhammad (PBUH)

“The ink of the scholar is more holy than the blood of martyr.”

Prophet Muhammad (PBUH)

“The superiority of a learned man over an ignorant worshipper is like that of the full moon over all the stars.”

Prophet Muhammad (PBUH)

To my matchless supervisor, Prof. **Clayton V. Deutsch** for his wonderful supervision and outstanding support.

And to my gentle and caring husband, my thoughtful parents, my merciful parents in-law, my lovely siblings and in-laws, and my kind-hearted grandparents, for their love and support.

Fatemeh, August 2013

Abstract

Geological heterogeneity is often represented by assigning rock properties to grids of different block size. Some geological features are represented as discrete objects at the chosen grid block size and others are represented as continuous properties. There is a transition between the discrete and continuous where the size of the features is too small to be represented discretely and too large to be represented continuously. This is linked to the notion of REV, that is, it is impossible to choose a grid size where geological features are at REV scale. An extended view of modeling regimes is proposed by modifying the classical REV plot presented by Bear. The challenge of geostatistical modeling in transition regime is addressed. A continuous framework is considered with particular attention to the spatial continuity since the scale of variability is larger than the scale of modeling. Numerical experiments are conducted on various geological models.

Acknowledgments

I would like to convey my honest gratitude to my amazing supervisor Prof. Clayton V. Deutsch for his patience, continuous encouragement, kind support, precious discussion and powerful leadership throughout my research.

I truly appreciate the productive and peaceful working environment, and financial support by the Centre of Computational Geostatistics (CCG) and the University of Alberta.

Thanks to my friend, Mrs. Hajar Amidian for her time and valuable comments on my thesis writing edition.

Especial thanks to Dr. John Manchuk for sharing his professional experience and his great comments.

Thanks to all CCG students, graduates, staff, and affiliates.

After all, I express my sincere thanks to my thoughtful husband, Mehdi for his love and my lovely family for their priceless support.

Table of Contents

1	Introduction.....	1
1.1	Problem Definition.....	1
1.2	Literature Review.....	2
1.2.1	Review on Mesh Types and Mesh Generators	2
1.2.2	Review on Solvers	3
1.2.3	Review of Reservoir Modeling, Upscaling and the Notion of an REV.....	4
1.3	Research Outline.....	8
2	General Points on Gridding and Flow Simulation on Grids.....	10
2.1	Structured and Unstructured Grids	10
2.2	Examples of Using Unstructured Grids for Fractured Media.....	11
2.3	Some Available Programs to Mesh Complex Geological Media	12
2.4	Delaunay Triangulation and Tetrahedralization	13
2.5	Unstructured Mesh Generation for a 2D Fractured Media	14
2.6	An Example of Unstructured 3D Mesh Generation by TetGen for a DFM.....	15
2.7	Grid Population with Petrophysical Properties.....	16
2.8	Flow Simulation on Structured/Unstructured Grids.....	17
2.9	Mathematical Background and Numerical Modeling.....	17
2.9.1	Continuity Equation	17
2.9.2	Darcy's Law (Vazquez, 2007).....	18
2.9.3	Pressure Equation	19
2.9.4	Pressure Equation Discretization	20
2.10	Transmissibility Estimation on Unstructured Grids	21
2.11	Connectivity Lists	22
2.12	Solving the Pressure Equation: The Coefficient Matrix Structure	24
2.13	Biconjugate Gradients Stabilized Method for Solving Systems of Equations...	25
2.14	Convergence Analysis	25
2.15	Conclusion.....	26
3	Scaling up of Effective Absolute Permeability.....	27

3.1	Motivation for Scale up.....	27
3.2	FLOWSIM Program.....	28
3.3	Single Phase Flow Upscaling	28
3.4	Motivation.....	28
3.5	Problem Formulation: Pressure Matrix in the FLOWSIM program	29
3.6	Solving the Pressure Equations.....	33
3.6.1	Direct Solver.....	34
3.6.2	Iterative (indirect) Solvers: LSOR, SIP.....	34
3.6.2.1	Linear Successive Over Relaxation.....	34
3.6.2.2	Strongly Implicit Procedure.....	35
3.7	Stopping Criterion	35
3.8	Applying the Algorithms.....	36
3.9	Stopping (Convergence) Criteria – Original Version	36
3.10	Case Studies	37
3.11	Conclusion.....	45
4	Representation of Geologic Features with Grids.....	46
4.1	A Classical Definition of Representative Elementary Volume (REV).....	46
4.2	Definition of Discrete, Transition and Continuous Regimes.....	48
4.3	Modifications on the Classic REV Plot.....	50
4.4	Criterion to Determine the Discrete – Transition Boundary.....	52
4.5	Criterion to Determine the Transition-Continuous Boundary	54
4.6	Dimensionless Length Scale Definition	55
4.7	General Review on Geological Models Put to Test.....	56
4.8	Evaluation of the Regime Boundaries on Small Models with Non Isotropic Objects	56
4.8.1	Boundary A: Evaluating the Discrete Length for Small models	58
4.8.2	Boundary B: Evaluating the Continuous Length for Small Models	60
4.8.3	Locating the Boundaries A and B on the REV Plots.....	61
4.9	Definition of the Transition Regime on a Large Model.....	64
4.9.1.	Boundary A: Evaluating the Discrete Length for Large Model.....	67
4.9.2.	Boundary B: Evaluating the Continuous Length for the Large Model	68

4.9.3.	Locating the Boundaries A and B on the REV Plot	70
4.10	Proposed Modified REV Plot	72
4.11	Conclusion.....	73
5	Practical Modeling Considerations for the Transition Regime	75
5.1	Motivation.....	75
5.2	Problem Definition.....	77
5.3	Generating Training Images (High Resolution Synthetic Models)	78
5.4	Histograms and Variograms of Generated Training Images	79
5.5	REV Plots Applicable to Select a Grid Size in Transition Regime.....	82
5.6	Quick Look at Variance Reduction through Upscaling.....	85
5.7	Plots of the Models at the Selected Grid Size in Transition.....	86
5.8	Histograms and Variograms of the Upscaled Models in Transition, Scenarios 1, 2 and 3.....	87
5.9	Continuous Simulation at Grid Size in the Transition Regime	90
5.10	Variogram and Histogram Reproduction	91
5.11	Scatter Plots of Simulated Permeability in Y-direction	93
5.12	Flow Simulation on the Scenarios and Simulated Models to Compare.....	94
5.13	Conclusion.....	105
6	Conclusions	107
	Bibliography	109

List of Tables

Table 2.1: Necessary Connectivity Lists	22
Table 3.1: Indices of the Pressure Matrix Diagonals.....	32
Table 3.2: Seven Diagonals of the Matrix in the FLOWSIM Program	33
Table 3.3: Dimension of the Pressure Matrix Diagonals.....	37
Table 3.4: Exact Solutions Resulted by GBAND.....	39
Table 3.5: CPU Time (Seconds) and the Number of Iterations to Converge.....	39
Table 3.6: CPU Time (Seconds) and the Number of Iterations to Converge.....	40
Table 3.7: CPU Time (Seconds) and the Number of Iterations to Converge.....	40
Table 4.1: Sample Volumes and Output Model Size Applicable for Small Models.....	58
Table 4.2: Dimension-less Length Scales for the Lower Boundary of the Transition Regime	60
Table 4.3: Estimated Discrete Length	60
Table 4.4: Dimension-less Length Scales for the Upper Boundary of the Transition Regime	61
Table 4.5: Estimated Continuous Lengths.....	61
Table 4.6: Sample Volumes and Resulted Output Model Size.....	66
Table 4.7: Estimated Discrete Length for Large Model.....	68
Table 4.8: Estimated Continuous Length for the Large Model	69
Table 4.9: General Range for Lower and Upper Boundaries of the Transition Regime....	72
Table 5.1: Shale Breaks' Sizes in Training Images	78
Table 5.2: Isotropic Sample Volumes.....	82
Table 5.3: Effective Values (mD) and Averages for Scenarios A, B and C	83
Table 5.4: Calculating the Boundaries of Transition Regime for Scenarios A, B and C.....	84
Table 5.5: Picking a Grid size in Transition Regime for Training Images.....	84

List of Figures

Figure 2.1: Structured grids.....	10
Figure 2.2: 2D Domain gridded by structured and unstructured grids.....	11
Figure 2.3: Delaunay criterion in 2D	13
Figure 2.4: Distribution of points on fractures and background (Razavi et al, 2011).....	14
Figure 2.5: Unstructured mesh generated based on the Delaunay criterion (Razavi et al, 2011)	15
Figure 2.6: An example of input 3D DFM with 7 fracture planes in TetGen (Razavi et al, 2011)	16
Figure 2.7: TetGen output visualized by TetView: a DFM with 7 fractures (Razavi et al, 2011)	16
Figure 2.8: Matrix-fracture connection to calculate transmissibility in case of unstructured grids (Razavi et al, 2011)	23
Figure 2.9: Matrix-matrix connection to calculate transmissibility in case of unstructured grids (Razavi et al, 2011)	23
Figure 2.10: a) Intermediate CV which is the intersection of 6 fractures with different thicknesses b) Three intersecting fracture CVs (Razavi et al, 2011)	24
Figure 2.11: Transmissibility matrix for a DFM meshed by unstructured grids.....	25
Figure 3.1: Left: Fine resolution model, Right: Coarse resolution with effective properties	28
Figure 3.2: Calculating K_{effX} : grid faces in Y and Z directions are no flow boundaries. ...	30
Figure 3.3: Calculating K_{effY} : Grid faces in X and Z directions are no flow boundaries. ...	31
Figure 3.4: Calculating K_{effZ} : Grid faces in X and Y directions are no flow boundaries. ...	31
Figure 3.5: Each grid block has 6 neighbors.....	32
Figure 3.6: Geological models under investigation.....	38
Figure 3.7: K_{effX} and P_X convergence for case 1	41
Figure 3.8: P_Z convergence: LSOR vs. SIP (Model HSB10.out).....	42
Figure 3.9: P_Z convergence: LSOR vs. SIP (Model HSB11.out).....	42
Figure 3.10: P_Y convergence: LSOR vs. SIP (Model4.out)	43

Figure 3.11: KeffZ convergence: LSOR vs. SIP (Model7.out).....	43
Figure 3.12 :PZ convergence: LSOR vs. SIP (Model7.out)	44
Figure 4.1: The representative elementary volume concept applied to porosity (Bear, 1972)	47
Figure 4.2: An example of the grid block size and the geological feature size in the discrete regime	48
Figure 4.3: An example of the grid block size and the geological feature size in the continuous regime	48
Figure 4.4: Representation of different regimes considering fixed grid size and various feature sizes	49
Figure 4.5: Discrete and continuous representation of the geological features: Fixed geological feature size and various grid block sizes.....	51
Figure 4.6: Schematic of the proposed model to modify the classic REV plot	52
Figure 4.7: Histogram of the point data.....	53
Figure 4.8: Histograms of the 3 upscaled models.....	53
Figure 4.9: Object and sample volume to define dimensionless length scale.....	55
Figure 4.10: a) non isotropic objects b) isotropic objects	55
Figure 4.11: Images of the models under test with no scale.....	56
Figure 4.12: Histogram of the point data: 30% low permeability grids and 70% high permeability grids	57
Figure 4.13: Objects scales versus whole models scales (all in meter).....	58
Figure 4.14: Proportion plots: First criteria for small models.....	59
Figure 4.15: Variance ratio: Boundary B criterion for small models.....	60
Figure 4.16: REV plots for the first model in X and Y directions (Small model with small objects), KeffX (mD) and KeffY (mD) vs. Grid size (m)	62
Figure 4.17: REV plots for the small model with bigger objects in X and Y directions	63
Figure 4.18: Plot of upscaled models at discrete and transition regimes.....	64
Figure 4.19: Large model with isotropic objects at 3 scales.....	65
Figure 4.20: Proportion plot for arithmetic averaging.....	68
Figure 4.21: Variance ratio plot for AA results.....	69
Figure 4.22: REV plot for the big model including ~150 million data	70

Figure 4.23: Model in the discrete regime showing edge effect, 250 × 250 × 1 model (Grid size: 4m × 4m × 1m)	71
Figure 4.24: Models in the transition regime	72
Figure 4.25: Proposed modified REV plot considering the levels of reservoir heterogeneity.....	74
Figure 5.1: Feature is partially present, completely present and multiple present in the grids.....	75
Figure 5.2: Mind-map for the practical modeling application at the transition regime...	76
Figure 5.3: The shaded area will be replaced with different geological models	77
Figure 5.4: Geological synthetic models generated by ELLISPIM, scenarios A, B and C...	79
Figure 5.5: Histogram of training images, same for A, B and C scenarios	80
Figure 5.6: Variograms in X and Y-directions for scenarios A, B and C	81
Figure 5.7: Effective values at different sample volumes for scenario A in X and Y- directions	83
Figure 5.8: Variance versus sample volume size in X-direction	85
Figure 5.9: Variance versus sample volume size in Y-direction	86
Figure 5.10: Pixel plot of the upscaled scenarios A, B and C	87
Figure 5.11: Distribution of Y permeability for scenario 2 (Reference distribution)	88
Figure 5.12: Fitted variograms for scenario 1, LHS: Horizontal variogram and RHS: Vertical variogram (in Transition)	89
Figure 5.13: Fitted variograms for scenario 2, LHS: Horizontal variogram and RHS: Vertical variogram (in Transition)	89
Figure 5.14: Fitted variograms for scenario 3, LHS: Horizontal variogram and RHS: Vertical variogram (in Discrete Regime)	89
Figure 5.15: Plots of simulated Y permeability, realizations # 10 & 90	91
Figure 5.16: Variogram and histogram reproduction, simulated model 1	92
Figure 5.17: Variogram and histogram reproduction, simulated model 2	93
Figure 5.18: Scatter plots of effective values (mD) for 100 realizations.....	93
Figure 5.19: Horizontal and vertical flooding tests on a geological model.....	95
Figure 5.20: Pixel plot of Keff in X and Y-directions for Scenario 2.....	95

Figure 5.21: Flow response (pressure distribution (bar)), scenario B and 2 discrete vs. coarser scale under horizontal and vertical flooding tests at 512 by 512 grid resolution (Considering both KeffX and KeffY in flow simulation).....	96
Figure 5.22: Scatter plots and correlation coefficients for flow reponses, scenarios B and 2	97
Figure 5.23: Homogenous flow response (bar) on 64 by 64 grid resolution	98
Figure 5.24: Comparison of pressure distribution (bar) on scenarios 1, 2 and 3 under horizontal and vertical flooding tests, 64 by 64 grid resolution (Considering both KeffX and KeffY of scenarios to get flow responses).....	99
Figure 5.25: Comparison between the pressure (bar) on simulated vertical K models and scenarios 1 and 2 in Y-direction (all in transition regime) and considering JUST KeffY of scenarios to get flow responses and to compare.	101
Figure 5.26: Pressure scatter (Cross) plot for scenario 1 and simulated model 1, horizontal flooding test (Considering only KeffY to get pressure distribution)	103
Figure 5.27: Pressure scatter plot for scenario 1 and simulated model 1, vertical flooding test (Considering only KeffY to get pressure distribution).....	103
Figure 5.28: Pressure scatter (Cross) plot for scenario 2 and simulated model 2, horizontal flooding test (Considering only KeffY to get pressure distribution)	104
Figure 5.29: Pressure scatter plot for scenario 2 and simulated model 2, vertical flooding test (Considering only KeffY to get pressure distribution).....	104

1 Introduction

1.1 Problem Definition

The development and management of petroleum reservoirs is an economically intensive activity. Choosing the sequence of development, the placement of wells and the operating strategy of the wells is important to the technical and economic success of the project. Flow simulation is often used to forecast the reservoir response for specific scenarios of development which permits optimization of the development strategy. A key input to flow simulation is a numerical description of the reservoir. The numerical model defines the geometry and internal properties of the reservoir. This numerical model should represent important geological features that vary at different scales.

Flow simulation, however, can only handle on the order of one million discretized grid blocks. Given the size of most reservoirs the grid blocks are necessarily quite large. There is geological variability at smaller scales. This is why upscaling the geological model is an essential and unavoidable step to obtain the flow simulation model. One problem addressed by this research is the calculation of effective properties of flow simulation grid blocks.

Geological features are captured by the effective properties at the grid block scale. For a fixed grid size, large geological features are represented as discrete volumes and small features are represented continuously as proportions or effective properties at the grid block size. This continuous representation is related to the classic notion of a representative elementary volume (REV). If geological features are represented discretely, discrete modeling techniques such as object based or indicator methods may be used. If they are represented continuously, continuous modeling approaches such as Gaussian approaches may be used. However, some features are in transition from discrete to continuous representation. Quantifying the applicability of the discrete and continuous representation of the geological features and also the transition between the discrete and continuous representation, are considerable problems. Then, for

geological features in transition, modeling is a challenge and there is a need to choose and apply a suitable modeling approach.

1.2 Literature Review

This review discusses topics related to what is covered in upcoming chapters of the thesis including grid mesh types, mesh generators, public programs applicable to mesh complex geological structures, solvers for the systems of equations used for upscaling, and the notion of an REV.

1.2.1 Review on Mesh Types and Mesh Generators

Mesh generation or grid generation is the discretization of the domain of interest in points or nodes where a solution is to be obtained. Nodes are connected to form elements or volumes (Ferziger, 2002). There are three major types of the grids based on the connectivity of the mesh. Mesh (grids) could be structured, unstructured or hybrid. Grids could be 2D or 3D. In structured gridding, the neighboring grid connections are known but there is irregular connectivity in the case of unstructured grids and the grid connectivity would be determined and explicitly stored. In hybrid gridding, both structured and unstructured gridding are applied within the same domain. Grids are generated by applying a suitable grid generation algorithms. To generate structured grids, several techniques can be applied to map the physical domain to a computational domain. Delaunay triangulation, advancing front and octree are the three main algorithms to automatically generate tetrahedral and triangular unstructured grids (Thompson, 2002). There are several public programs and software available to generate structured and unstructured grids automatically.

DistMesh is a simple MATLAB code for generating unstructured triangular and tetrahedral meshes that uses a Delaunay triangulation and tetrahedralization algorithm. It was developed by the Department of Mathematics at MIT. As of 2004 Per-Olof Persson and Gilbert Strang provided a detailed description of the program on the DistMesh website.

TetGen and Triangle are two well-tested mesh generators for 3D tetrahedral and 2D triangular meshing. TetGen was developed by the Numerical Mathematics and Scientific Computing group at WIAS (www.wias-berlin.de) which generates conforming Delaunay tetrahedra with volume control. Triangle was developed by the Computer Science Division at Berkley University (Triangle website). MeshPy combines TetGen with Triangle into a practical package, and was developed at the Institute of Mathematical Sciences at New York University. A detailed description could be found on the MeshPy website.

Gridgen, Gambit, Fluent, Comsol and Gridpro are among the popular CFD softwares that are applied to generate grids (www.cfd-online.com). CMG Builder (www.cmgl.ca), Petrel and FloGrid (www.slb.com) are among well-known softwares in the petroleum industry that also provide possibilities to mesh geological media.

1.2.2 Review on Solvers

System of equations are created by discretized flow equations. Such systems are sometimes solved by direct methods such as Gauss elimination or LU decomposition. The pressure equation that must be solved for effective permeability calculation is quite large and sparse. The CPU and storage cost of direct methods are fairly high. Therefore, iterative solution methods are commonly employed. In an iterative method, one should guess a solution (which is the starting point) and use the equation to systematically improve it (Ferziger, 2002). If the number of iterations is small and each iteration is cheap, an iterative solver may cost less than a direct method which is usually the case in CFD related problems including the pressure equation in upscaling.

Several efforts have been made to develop linear solvers and the pre-conditioners that improve the performance of flow simulators by using a fast solver. In 1981, Watts applied the preconditioned conjugate gradient method to solve the pressure equation and compared the results with the Strongly Implicit Algorithm (SIP). He showed that SIP is faster than preconditioned conjugate gradient for 3D problems but slower for 2D ones (Watts and James, 1981). In 1988, Eisenstat described a collection of block preconditioners to use for solving large, sparse, linear systems of equations by iterative

methods, and compared their performance with several point preconditioners in solving some systems appearing in numerical reservoir simulation. Brand presented the successful application of an incomplete LU (ILU) factorization technique coupled with generalized conjugate-gradient (as an acceleration) to solve a set of equations (Brand et al, 1990). In the field of Mathematics in 2001 at the University of Texas, Eaton completed his PhD research related on the multigrid preconditioner. He discussed how a multigrid preconditioner was successfully applied for a 2D flow problem (Eaton, 2001). Furthermore, several solver packages have been used in Integrated Parallel Accurate Reservoir Simulators (IPARS). Generalized minimum residual (GMRES) with various preconditioners like Linear Successive Over Relaxation, Incomplete Lower Upper and Algebraic Multi Grid are the most popular methods in IPARS (most used for parallel simulations) (Klie and Wheeler, 2005).

The Algebraic Multigrid method is another efficient solver and preconditioner for the flow equation system that has gained attention. For example, a package named SAMG (Algebraic Multigrid Methods for Systems) has been developed in this area by Fraunhofer (Klaus Stüben and Tanja Clee, 2007). Mishev discussed how AMG could be one of the most efficient solvers that is handling linear systems produced by the discretization of the pressure equation in Implicit Pressure Explicit Saturation (IMPES) and Sequential Implicit formulations. The AMG can be implemented in parallel algorithms. HYPRE is an available library of high performance preconditioners to solve large sparse linear systems. It includes several solvers and preconditioners that are applicable in parallel multiphysics and multiscale simulation.

1.2.3 Review of Reservoir Modeling, Upscaling and the Notion of an REV

Reservoir performance evaluation is done by applying a numerical model of the static/dynamic behaviour of the reservoir. The spatial distribution of the rock properties and heterogeneities have to be carefully represented in the numerical model to have the greatest predictive capability (Koltermann and Gorelick, 1996). There are two aspects to be considered: (1) generating a high resolution numerical geological model, and (2) upscaling the high resolution model to a grid suitable for flow simulation. There

is also the important decision of how to choose the scales of the numerical geological and numerical flow models. Sub-meter scale lithological properties and heterogeneities are often rescaled to representative values seeing that computational limitations often do not allow us to use them directly in a full-field reservoir simulator. Some issues when rescaling heterogeneities can be seen in the following papers; Worthington (1993 & 2004), Corbett (1992 & 1998), Delleur (2006). Four conceptual scales associated with averaging properties in porous rock media have been proposed by Haldorsen & Lake (Haldorsen and Lake, 1984). The notion of a Representative Elementary Volume (REV) has been introduced by Bear (1972) at which the parameter of interest is both statistically stationary and homogeneous.

An REV represents a large enough volume of the property field that really small scale variations are captured within the volume, yet representative heterogeneity is represented between volumes at the REV scale. The concept of an REV has been discussed by many researchers in relation to the calculation of effective petrophysical properties (Hassanizadeh, 2004), (Flint, 2009), (Netinger, 1994), (Nordahl and Ringrose, 2005). Porosity, being an additive property, is mainly upscaled by simple averaging schemes while the upscaling of permeability, a non-additive property, should generally be performed on practical models where sedimentological heterogeneities are revealed clearly. Variograms could also be of great help to characterize permeability (McKinley, 2004) and percolation theory (Begg and King, 1985) and effective media theory (Durlflosky, 1991) are common methods to estimate effective properties. Deterministic modeling of sedimentary structures is presented in detail by Anggraeni, (1999), Pickup (1994), Jackson (2005).

Jackson characterized the effective permeability of facies using 3D models. He showed that the key controlling point is the connectivity and continuity between low and high permeable layers which is not easy to capture these key factors in different length scales (Jackson, 2005). He also discussed that averaged effective permeability is a function of sample volumes while flow direction and facies types are major points in selecting the suitable averaging scheme to reduce the introduced error resulted by upscaling

techniques (Jackson, 2003). McKinley characterized permeability by variogram analysis (McKinley, 2004).

In the following papers, flow barriers are modeled stochastically and the anisotropy is presented by using different correlation lengths in the vertical and horizontal directions. The effect of the block-size corresponding to the scale of heterogeneity has been discussed as well (Begg and Carter, 1989), (Desbarats, 1989), (Deutsch, 1989). Ozdemir and Ozguc determined REV for porosity with this assumption that porosity varies exponentially at well regions of the porous medium (Ozdemir, 1997). Leung and Srinivasan assessed uncertainty introduced by scale up in reservoir models when the REV scale is larger than the volume support size (Leung, 2009 and 2011). The relation between statistical moments (mean, variance and integral scale) of the upscaled permeability to the permeability of homogenous porous media is discussed when the flow is steady in (Peter and Gedeon, 1991).

Lake and Srinivasan used the variance of the mean of a random variable and the changes in horizontal and vertical permeability to get robust estimation of uncertainty in scaled up values (Lake, 2004). The effect of geological heterogeneity on flow has been investigated for continuous and discrete domains considering geostatistical approaches by Eaton. REV is used to reinterpret hydrofacies as scale-dependant hydrogeologic units (Eaton, 2006).

There is discussion on the correlation length and the effect of scale on flow in Hunt (2009), Bloschl (1995), Evesque (2000), Müller (2010). Sorek investigated that how the REV scale could affect phase balance equation when dealing with different types of fluids in a heat transfer phenomena (Sorek, 2010). Yong presented a new method for 3D conductivity upscaling in heterogeneous porous media. He showed that his method is more successful than traditional upscaling techniques and also porosity upscaling is critical when dealing with contaminant transport. Upscaled porosity in such cases is beyond the traditional porosity obtained on the REV scale. The similarities and differences between conductivity and porosity upscaling are also discussed by Yong (2004). Vogel and Brown quantify REV and a scale disparity factor to find a sample size.

The sample size is used to determine a meaningful semivariogram when correlation lengths are specified. Directional semivariograms and a scale disparity factor are used to get vertical and horizontal correlation lengths in small and large scales, considering that REV analysis is scalar in nature and semivariograms are based on vector analysis (Vogel, 2003).

Three volume averaging methods as REV tests are presented by Brown, Hsieh and Lucero including prismatic volume averaging, stacked slice averaging and a qualitative test. They tried to evaluate proper core sample size in the laboratory and found all core sizes suitable for the experiments comparing their respective REV size, while showing that one single core is not enough for the experiments (Brown, 2000). The authors applied their proposed method to determine REV based on porosity and phase volume fraction in two-phase systems (Clausnitzer, 1998). Rooij focused on upscaling from REV-scale to a larger scale beyond the REV considering water flow through porous media with different degrees of heterogeneity. He investigated the validity of Darcy's law under the superposition principle (Rooji, 2008). Data quality implications of an REV have been examined by Robinson and Estabrook for porosity and water saturation in an unsaturated porous media (Costanza-Robinson, 2011). Gray and Miller proposed the thermodynamically constrained averaging theory (TCAT) approach to deal with inconsistencies and ill-defined variables in porous media modeling (Gary, 2004). Nachabe and Morel also discuss how to scale aquifer flow equation. They demonstrate that the small-scale macroscopic variability of aquifer transmissivity affects the megascopic behavior of the flow in both space and time (Nachabe, 1999). The flow of two fluids has been studied theoretically by Quintard (1989) at pore level with Stokes equations and also local volume averaging has been applied for the derivation of Darcy-scale equations over a large region compared to the length scale of heterogeneities. The numerical results have been compared statistically with the experimental data as well. Zhang systematically studied the scale dependency of the permeability and porosity and assessed the concept of statistical REV on a reservoir model based on the lattice Boltzmann simulations. A single statistical REV is defined, while deterministic REV isn't defined since the scale of the whole domain changes (Zhang, 2000).

Ringrose provided a review on current limitations of the implementation of multiscale modelling (2012). The author discussed how many scales should be modeled and upscaled and on which scales, one should focus. Nordahl and Ringrose evaluate the representative elementary volume for permeability at the lithofacies scale with a new insight. They show that REV varies with changing in lithofacies types and also depends on the measured property (vertical and horizontal permeability) (Nordahl and Ringrose, 2008).

1.3 Research Outline

The first step of numerical modeling is discretizing the domain with grids. The grid shape could have different degrees of flexibility to discretize complex geological media based on finite difference, finite element or finite volume methods. Structured and unstructured grids are two major grid types that are discussed in the **second chapter**. The mathematical background of a flow simulator applicable for both structured and unstructured grids are explained. Also, two examples of 2D and 3D discrete fracture networks meshed by unstructured grids are presented (Razavi et al, 2011).

A common problem in geostatistical reservoir modelling is the calculation of effective permeability to represent a high resolution regular grid. The FLOWSIM program has been used since the mid 1980s for this purpose. **Chapter three** reviews the implementation of the FLOWSIM program and recommends some changes including applying another iterative solver (SIP - the strongly implicit procedure) and convergence criteria that permit reliable results without excessive computational effort. The results are checked with a direct solver.

Small scale heterogeneities are captured in effective properties at the grid block scale. Reservoir features (heterogeneities) that are large with respect to the grid size can be represented as discrete objects, that is, each grid block is in or out of the feature. Reservoir features that are smaller than the grid block size must be represented as proportions of the features within the grid block, that is, each grid block contains a continuous proportion of the feature. For a fixed grid size, large features are represented discretely and small features are represented continuously. Some features

are in transition between the discrete and continuous regime. The grid size that becomes large with respect to the feature size is sometimes referred to as representative elementary volume (REV). The classical REV plot was proposed by Bear (1972). Transition from the discrete domain, where there is little mixing, to continuous domain, where they are all mixed, is important to investigate as it is necessary to consider the most suitable modeling approach. The scales of the discrete, transition and continuous regimes are quantified. In **chapter four**, for this purpose, some models at different sizes and with different object sizes are constructed and the progression from discrete to transition and also from transition to continuous is explored. A modified version of the classical REV plot is also presented.

If geological features are represented discretely, discrete modeling techniques such as object based or indicator methods may be used. If they are represented continuously, continuous modeling approaches such as Gaussian approaches may be used. But the transition regime is a challenge because there is significant variability between grid blocks and within grid blocks. There is a need to adapt the modeling approach for the transition. The **fifth chapter** of the thesis shows the challenge of modeling in transition.

Chapter six is the final chapter and provides a conclusion and discusses possibilities for future work.

2 General Points on Gridding and Flow Simulation on Grids

The flow of fluids through a petroleum reservoir is simulated by solving flow equations that require the spatial domain to be discretized by structured or unstructured grids.

2.1 Structured and Unstructured Grids

In case of structured grids, the neighbors of each grid are easily known and hence, they have clear data structure and grid connectivity list. Structured grids can be orthogonal Cartesian or boundary-fitted non-orthogonal curvilinear grids. Cartesian grids are the simplest grids to work with, but they may not effectively discretize complex geometries, Figure 2.1a. Curvilinear grids may be more adaptable to complex geometries and may be preferred, Figure 2.1b. Figure 2.1 shows schematic illustrations of structured grids with no particular scale.

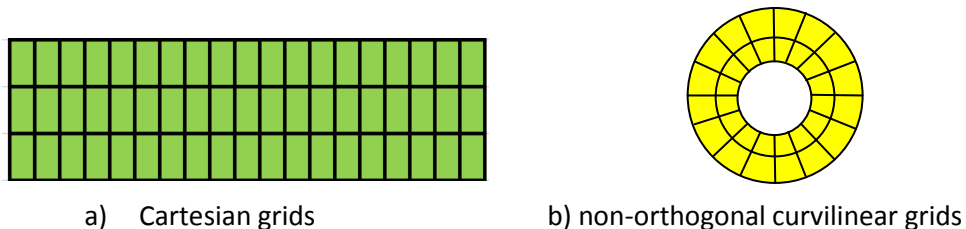


Figure 2.1: Structured grids

Unlike structured grids, unstructured grids do not have an explicit data structure and creating the connectivity list requires more computational effort; however, unstructured grids provide flexibility in mesh generation and discretization of the complex geometries. One advantage of unstructured grids is the possibility of controlling the grid resolution through refinement. Considering the geometrical simplicity and the accessible procedures for the numerical simulation of physical problems (Liseikin, 2010), unstructured grids are generally composed of triangles in two dimensions and tetrahedrons in three dimensions. Figure 2.2 shows a simple square meshed with structured and unstructured grids that is conceptual with no specific scale.

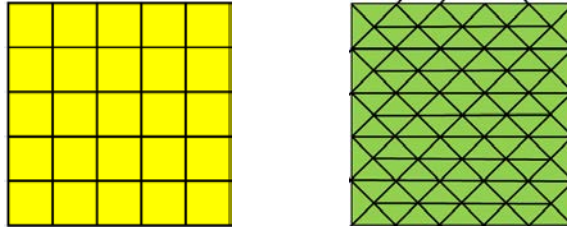


Figure 2.2: 2D Domain gridded by structured and unstructured grids

There are three common methods to construct unstructured grids including octree methods, Delaunay procedures and Advancing Front techniques (Liseikin, 2010). Delaunay tessellation is a geometric decomposition tool to generate triangular and tetrahedral grids that has found wide use in engineering applications. Two and three-dimensional Delaunay tessellations are used for the analysis of porous media, and the modeling of flow in porous media (Thompson, 2002). Liseikin's work (Liseikin, 2010) is a good reference to gain information about the two other methods for unstructured mesh generation. There are many research and commercial programs for grid generation (www.cfd-online.com).

2.2 Examples of Using Unstructured Grids for Fractured Media

The geological model should be discretized for flow simulation purposes and numerical modeling is used to predict flow behavior and simulate transport phenomena. One of the origins of complexity in a geological medium is the existence of a large number of fractures where an efficient discretization of the fractured media requires significant effort.

A research code has been developed to generate an unstructured triangular mesh for a randomly generated discrete fracture network in 2D. The software TetGen, which is an open access program to construct triangular and tetrahedral grids, is used to generate a mesh for a 3D discrete fracture network (Razavi et al, 2011).

There are two approaches to model flow and mass transport in fractured porous media: (1) a dual continuum model proposed by Warren & Root in 1963, and (2) a discrete

fracture model (DFM). A DFM is a reasonable method to model laboratory scale fractured porous media (Ito, 2003).

In the case of open fractures, flow moves through the fractures and, consequently, creating grids aligned with the fractures can be important. There are various open access programs to mesh complex geological media, see below.

2.3 Some Available Programs to Mesh Complex Geological Media

DistMesh is a simple MATLAB code to generate unstructured triangular and tetrahedral meshes which applies Delaunay's triangulation and tetrahedralization to construct the grids. The program was developed by the Department of Mathematics at MIT and the code could be modified based on specific needs. A detailed description of the program is provided by Per-Olof Persson and Gilbert Strang (DistMesh website).

G23FM is another grid generator applicable for 2D and 3D fractured media. It is a flexible tool that gives different options during mesh generation like adding points, controlling size of triangles, refinement and scaling (Mustapha, 2010). It was developed by a computer science specialist at McGill University.

FracMesh is a structured mesh generator that is applicable in 2D and 3D and was developed by the Earth Sciences Division at Berkley. The most complicated part of a fracture network gridding is creating the connectivity list. FracMesh produces these connectivity lists that are necessary for input to multiphase flow simulation (Ito, 2003).

TetGen and Triangle are two well-tested mesh generators for 3D tetrahedral and 2D triangular meshing. TetGen was developed by Numerical Mathematics and Scientific Computing group at WIAS (<http://www.wias-berlin.de>). Triangle was developed by the Computer Science Division at Berkley. MeshPy was developed at the Institute of Mathematical Sciences at New York University; it combines TetGen with Triangle into one package.

In the next section, Delaunay triangulation and tetrahedralization will be explained which are very common to construct unstructured grids and also are the basis of most mesh generators.

2.4 Delaunay Triangulation and Tetrahedralization

Delaunay triangulation and tetrahedralization is applied based on a criterion. According to this criterion, neighbouring points are connected to form triangular or tetrahedral cells in such a way that the circumcircle through the three vertices of a triangular cell in two-dimension and the circumsphere through the four vertices of a tetrahedral cell in three-dimension do not contain any other point. This condition is called Delaunay criterion. The left circumcircle through the vertices of a triangular cell in Figure 2.3 contains another point and it invalidates the first while the right circumcircle through the vertices of the triangle doesn't contain the other point and it follows the Delaunay criterion.

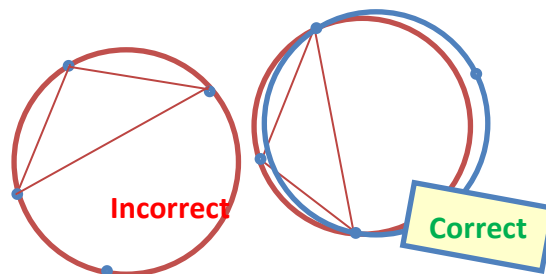


Figure 2.3: Delaunay criterion in 2D

Applying Delaunay criterion in 2D entails that the minimum angle of the triangles in the triangulation will be maximized and the maximum circumradius will be minimized. This avoids skinny triangles (Liseikin, 2010). The nice properties of Delaunay triangulation are not true in 3D, since a measurement for optimality in 3D is not agreed upon. Slivers are special types of badly-shaped tetrahedrons which are flat and nearly degenerate and they cause instability and inconsistency. In 3D, slivers could survive even after Delaunay refinement. To measure the quality of tetrahedrons, two criteria are considered: 1) the aspect ratio of an element which should be as small as possible and is defined as a ratio of the maximum side length to the minimum, and 2) the radius edge ratio which is the

ratio of the radius of the circumsphere of the tetrahedron to the length of the shortest edge. This value should be small for a well-shaped tetrahedron. The Delaunay criterion is applied in the next sections to generate triangular and tetrahedral mesh for 2D and 3D sample fractured media.

2.5 Unstructured Mesh Generation for a 2D Fractured Media

Fractures could be represented as lines including two endpoints in 2D and planes including four endpoints in 3D. Considering a 2D fractured model with numerous random fractures, the following steps have been followed to get the final discretized model: 1) select a domain size and establish the fracture endpoints, 2) distribute points in the background, 3) remove background points that are close to the fractures, 4) generate a mesh based on the Delaunay criterion and visualize in MATLAB by applying the “DelaunayTri” and “triplot” commands, respectively. A sample 2D model is presented in Figure 2.4 and Figure 2.5 that shows the point distribution on the fractured 2D model and the generated Delaunay mesh.

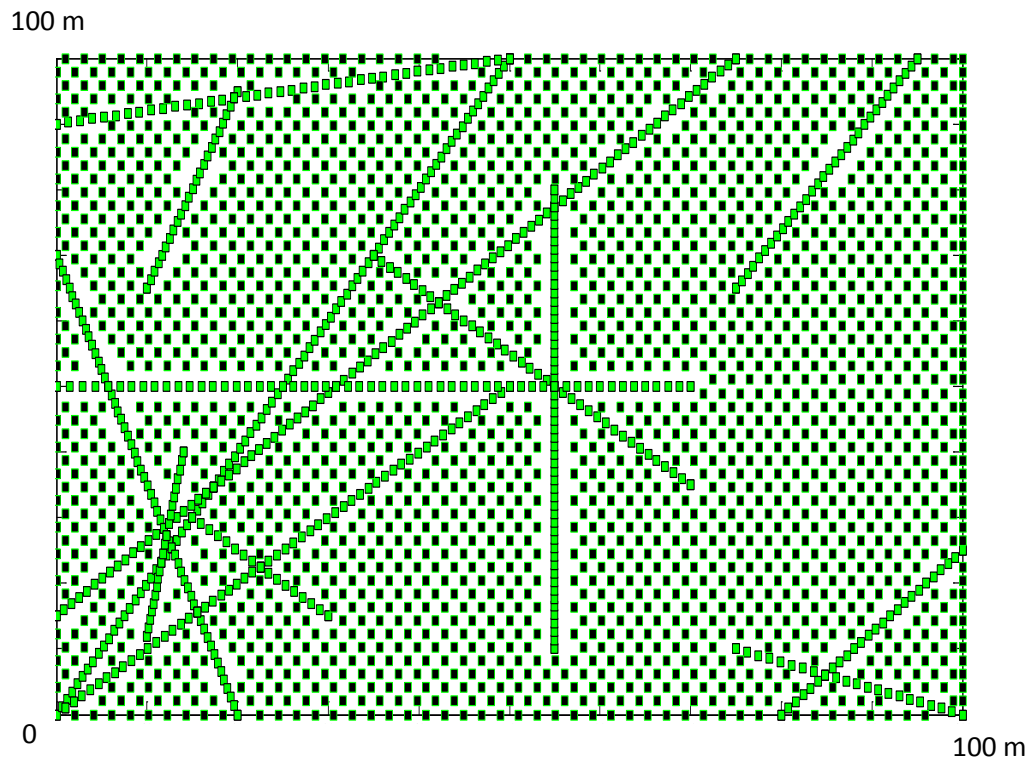


Figure 2.4: Distribution of points on fractures and background (Razavi et al, 2011)

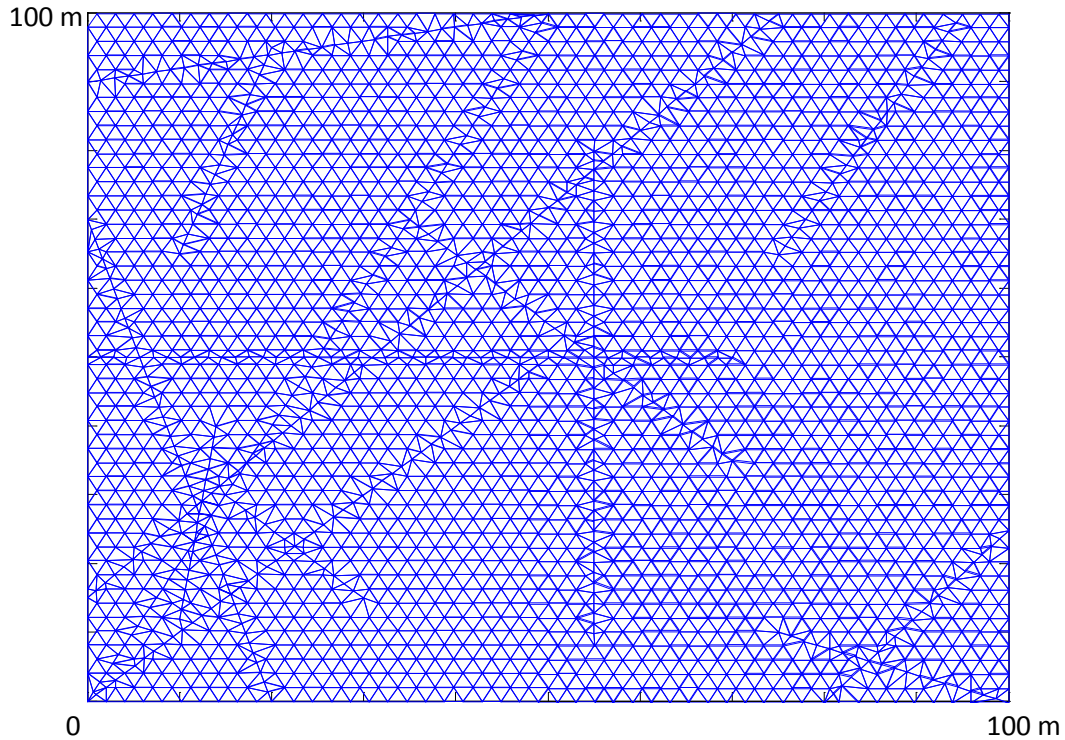


Figure 2.5: Unstructured mesh generated based on the Delaunay criterion

(Razavi et al, 2011)

The mesh looks reasonable around the fractures and at the intersections of the fractures. Subsurface flow modeling around the fractures is affected by gridding and unstructured grids may be preferable since the grids can present the characteristics of fractures more realistically in modeling. Detailed information on the developed program has been documented in a research paper (Razavi et al, 2011).

2.6 An Example of Unstructured 3D Mesh Generation by TetGen for a DFM

TetGen generates tetrahedral meshes suitable for numerical simulation that use finite volume or finite element methods. Tetrahedralization is based on the Delaunay criterion. The quality of the tetrahedrons is measured by the two criteria mentioned above: (1) the aspect ratio of the element and (2) the radius edge ratio. Some of the degenerate tetrahedra slivers can be removed by TetGen using the local flip technique. Figure 2.6 shows an example of input 3D DFM suitable for TetGen. The model includes 7 fracture planes where each is defined as a facet. TetGen output is visualized by TetView. The unstructured mesh that includes all tetrahedra generated by TetGen is shown in

Figure 2.7. The fracture planes are presented in green and Delaunay tetrahedra are presented in red in the left figure. The right mesh in Figure 2.7 shows only the boundary facets of the mesh. The edges of the fractures are presented as green lines. The grids are aligned with the fracture planes. Generating the fracture planes, detecting the intersections between fracture planes, creating TetGen input file, getting output and visualization are explained in (Razavi et al, 2011).

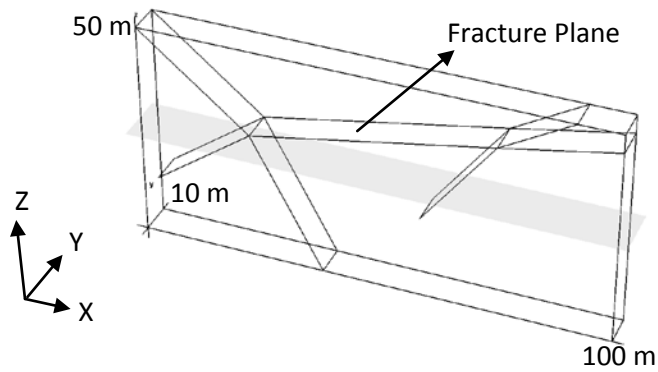


Figure 2.6: An example of input 3D DFM with 7 fracture planes in TetGen (Razavi et al, 2011)

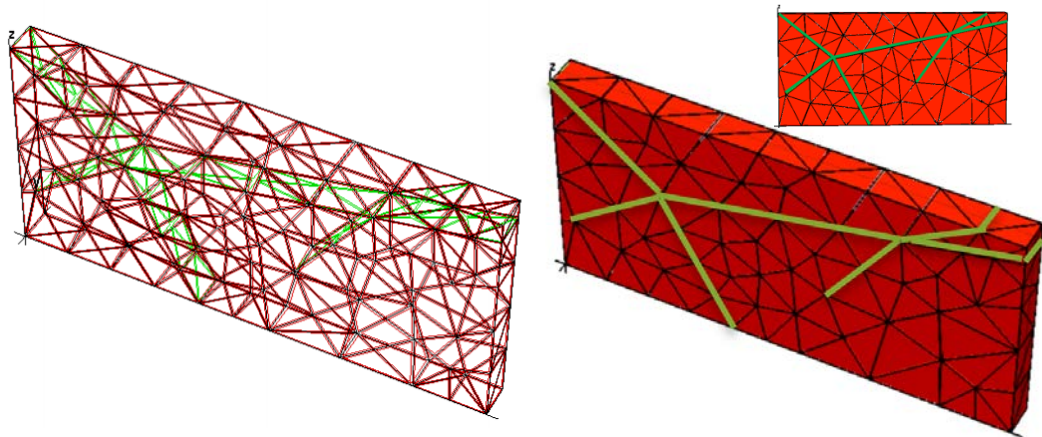


Figure 2.7: TetGen output visualized by TetView: a DFM with 7 fractures (Razavi et al, 2011)

2.7 Grid Population with Petrophysical Properties

The generated grids should be populated with petrophysical properties. Geostatistical modeling of petrophysical properties could be conducted by using a GSLIB-like program called PSGSIM (Manchuk, 2010) that performs sequential Gaussian simulation of

continuous variables and sequential indicator simulation of categorical properties on irregular sets of points such as unstructured grids. These sets of points are locations in the triangular/tetrahedral control volumes in 2D/3D such as:

- A) At the center of the unique circumcircle/circumsphere of each triangle/tetrahedron or,
- B) At the centroid, named also geometric center, center of mass, center of gravity or barycenter of each triangle/tetrahedron.

Detailed information is available (Manchuk, 2010).

The next section will focus on the important step after gridding, that is, flow modeling on the structured and unstructured grids.

2.8 Flow Simulation on Structured/Unstructured Grids

In this section, the finite volume form of the mass conservation law that is applied to model single phase flow in a 3D discrete fractured model meshed by unstructured tetrahedral grids is reviewed. Unstructured grids help handle complex fractured media. The transmissibility should be calculated for all connections in the fractured model including matrix-matrix, fracture-fracture and matrix-fracture connections. Thus, flow is measured along and between fractures. The flow simulator is predominantly based on connectivity lists. Creating the connectivity lists requires significant preprocessing effort especially for a 3D model.

2.9 Mathematical Background and Numerical Modeling

The goal is finding the solution of the pressure equation that is obtained based on the fundamental law of mass conservation and Darcy's law (Bajaj, 2009).

2.9.1 Continuity Equation

“Conservation laws are resulting by considering a known quantity of control mass (CM) and its extensive properties such as mass, momentum and energy. We have to deal with the flow within a certain spatial region called control volume (CV) rather than a control

mass. So, the conservation laws should be transformed into a CV form and with the intensive variables rather than extensive properties which this transformation is done by Reynolds' Transport Theorem (RTT). RTT states that the rate of changing in the amount of extensive property in the CM, is the rate of the property change within the CV in addition to the net flux of it through the CV boundary due to fluid motion relative to the CV boundary" (Ferziger, 2002). Considering Ω as CV with ϕ property as porosity, $\partial\Omega$ is the surface of CV and n is the normal vector at any point of the surface. Based on the mass conservation law on Ω , we have:

$$(\text{Rate of inflow} - \text{Rate of outflow}) + \text{Source} = \text{Accumulation}$$

$$\int_{\partial\Omega} (-\rho u) \cdot n dS + \int_{\Omega} \tilde{m} d\Omega = \int_{\Omega} \frac{\delta}{\delta t} (\phi\rho) d\Omega \quad (2.1)$$

where in Equation 2.1, ρ is fluid density (lb/ft³), u is Darcy velocity (ft/day) and \tilde{m} is source/sink term (unit mass/ (unit volume \times unit time)).

By applying divergence theorem to the first term of the left hand side of the Equation 2.1 which is convective term, the surface integral is transformed to a volume integral; and the differential coordinate-free form of the continuity equation will be obtained as follows, Equation 2.2 (Bajaj, 2009).

$$-\nabla \cdot (\rho u) + \tilde{m} = \frac{\delta}{\delta t} (\phi\rho) \quad (2.2)$$

Nest section is about the Darcy's Law.

2.9.2 Darcy's Law (Vazquez, 2007)

Modeling of filtration in porous media is performed by Darcy's law for low flow velocities (Aarnes, 2007). Flow apparent velocity, u , is related to gravity forces and pressure through the following formula:

$$u = -\frac{K}{\mu} (\nabla p + \rho g \nabla z) \quad (2.3)$$

K is permeability, μ is viscosity, g is gravitational constant and z is the spatial coordinate.

There are some assumptions behind Darcy's law:

- 1) Flow is laminar. For turbulent flow, which occurs at high velocities, the pressure gradient increases at a greater rate compared to the flow rate,
- 2) Flow regime is steady state and the pressure of the reservoir does not change with time,
- 3) Isothermal condition is considered in which temperature change results in a change in viscosity,
- 4) The fluid is incompressible. Compressible fluids have a different pressure gradient as compared to the incompressible fluids,
- 5) Formation is considered to be homogeneous with incompressible rock (constant porosity) and isotropic permeabilities.

The pressure equation is obtained in the next section based on the continuity equation and Darcy's law.

2.9.3 Pressure Equation

By neglecting gravity forces, considering horizontal flow, in Equation 2.3 and combining it with continuity equation, Equation 2.2, the pressure equation is obtained.

$$\nabla \cdot \left(\rho \frac{K}{\mu} \nabla p \right) + \tilde{m} = \frac{\delta}{\delta t} (\phi \rho) \quad (2.4)$$

Considering incompressible fluid and rock, Equation 2.4 is written as follows:

$$-\nabla \cdot \left(\frac{K}{\mu} \nabla p \right) = \frac{\tilde{m}}{\rho} = \tilde{q} \quad (2.5)$$

\tilde{q} is the volumetric source term (Bajaj, 2009).

2.9.4 Pressure Equation Discretization

A cell-centered finite volume method is presented that is named Two Point Flux Approximation (TPFA). This is one of the simplest discretization techniques to solve the pressure equation; it uses two points to approximate the flux. TPFA is exact for orthogonal or K-orthogonal systems with anisotropic permeability. The neighboring cells' average pressures are used to estimate the flux through the interface between the adjoining cells. Consider the integral form of Equation 2.5:

$$\int_{\Omega_i} (\tilde{q} - \nabla \cdot u) dV = 0 \quad (2.6)$$

By applying divergence theorem, the volume integral will be transformed to surface integral and Equation 2.7 is obtained.

$$\int_{\partial\Omega_i} (-\lambda \nabla p) \cdot n dS = \int_{\Omega_i} \tilde{q} dV \quad (2.7)$$

λ is the ratio of permeability to viscosity named fluid mobility. $\partial\Omega_i$ is the total area of i^{th} CV which is the summation of areas of the CVs' interfaces, $\partial\Omega_{ij}$ s.

f_{ij} is the flux through the interface $\partial\Omega_{ij}$ (the common face between cell i and cell j) that should be estimated across the interface from a set of neighboring cell pressures.

$$\partial\Omega_{ij} = \Omega_i \cap \Omega_j \quad (2.8)$$

$$f_{ij} = - \int_{\partial\Omega_{ij}} (\lambda \nabla p \cdot n) dS = T_{ij} (P_i - P_j) \quad (2.9)$$

T_{ij} is defined as the transmissibility of the surface $\partial\Omega_{ij}$. To get the total flux through the cell, the summation of the Equation 2.9 should be calculated over all the interfaces of the CV. By placing Equation 2.9 in Equation 2.7, the TPFA scheme for the pressure

equation is obtained. j is the number of faces of each CV. The procedure is identical for any CV shape, structured or unstructured, and any dimension.

$$\sum_j T_{ij}(P_i - P_j) = \int_{\Omega_i} \tilde{q} dV = Q \forall \Omega_i \cap \Omega_j \quad (2.10)$$

Applying Equation 2.10 with structured grids is straightforward. The transmissibility calculation for unstructured grids is a challenge that will be considered below.

2.10 Transmissibility Estimation on Unstructured Grids

In this section, a discrete fracture model that is discretized by unstructured grids is considered for transmissibility estimation on unstructured grids. Karimi-Fard presented a simplified DFM useful for transmissibility calculation on an unstructured mesh (Karimi-Fard, 2003).

The simplifications help to calculate transmissibility for fracture-fracture, matrix-fracture and matrix-matrix connections with the TPFA technique. In the model, the place of the unknowns is at the barycenter of the grids. The 3D simulator will be based on the connectivity lists. The connections between all the control volumes (CVs) should be specified. For any CV, flow at the interface $\partial\Omega_{ij}$, is calculated as follows:

$$T_{ij}(P_i - P_j) = Q_{ij} \quad (2.11)$$

where T_{ij} is the transmissibility at the interface $\partial\Omega_{ij}$ and P_i is the pressure at cell i . T_{ij} is defined as follows: (Karimi-Fard, 2003)

$$T_{ij} = \frac{\alpha_i \alpha_j}{\alpha_i + \alpha_j}, \quad \alpha_i = \frac{AK_i}{D_i} n_i \cdot d_i \quad (2.12)$$

T_{ij} is calculated for all interfaces. α is evaluated for each grid cell. A is the area of the interface between the adjacent cells. n_i is unit normal to the interface inside CV_i . d_i is

unit vector along the line joining the center of the triangle to the center of interface. D_i is the distance between the centroid of the interface and the centroid of the cell i . K_i is the permeability of CV_i .

2.11 Connectivity Lists

Connectivity information between the unstructured elements in 2D/3D are required to solve the pressure equation for single phase flow. In a 3D Delaunay mesh, each tetrahedron is linked with 4 adjacent tetrahedrons and in a 2D Delaunay mesh; each triangle is linked with 3 adjacent triangles with equal flux through the common interface. Note that fractures are represented by lines in 2D and planes in 3D. The following connectivity lists have to be created for 2D and 3D mesh.

Table 2.1: Necessary Connectivity Lists

Connectivity Lists: 2D/3D
A set of neighboring CVs for each CV
A set of CVs sharing common edge (2D) / face (3D)
Boundary CVs
Boundary edges/faces
Fracture edges/faces
CVs connected to the fractures named fracture CVs
Fracture-fracture connectivity list
Boundary fracture CVs

For a 2D DFM meshed by Delaunay triangular grids, Bajaj's work (2009) is a suitable source to study. Investigating the connections for transmissibility approximation is mainly divided to 3 steps: Matrix-Matrix connection, Matrix-Fracture connection, Fracture-Fracture connections that is also called fracture intersections. As mentioned before, to think about the connections, the simplified discrete fracture model proposed by Karimi-Fard (Karimi-Fard, 2003) is applied for 3D DFM, see Figure 2.8, Figure 2.9 and Figure 2.10. The figures show schematic illustration of different connections without any specific scale. Grid domain and computational domain are separated in Karimi-Fard's

model. Nodes are 0D objects. Segments defined by 2 nodes are 1D objects. Convex polygons defined by segments are 2D objects. Convex polyhedral defined by convex polygons are 3D objects. Figure 2.8 shows the matrix-fracture connection in the grid domain and computational domain in 2D and 3D. Figure 2.9 shows grids in 2D and 3D in case of matrix-matrix connection.

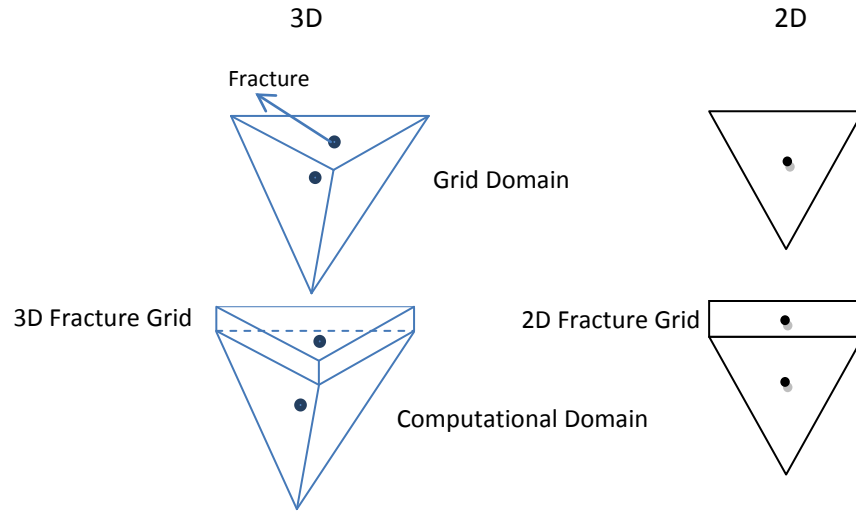


Figure 2.8: Matrix-fracture connection to calculate transmissibility in case of unstructured grids (Razavi et al, 2011)

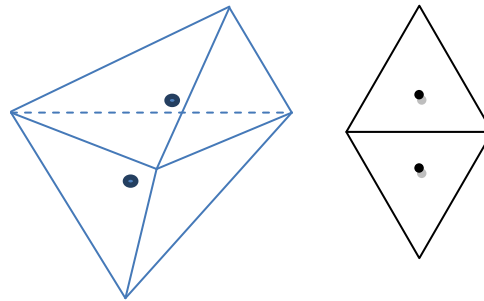


Figure 2.9: Matrix-matrix connection to calculate transmissibility in case of unstructured grids (Razavi et al, 2011)

To handle the intersections, an intermediate control volume (Figure 2.10a) is considered for numerical connections between two or more fractures. It helps to consider flow redirection and thickness variation. Since fracture intersection CVs (Figure 2.10b) are small and cause instability in the calculations, they have to be eliminated (Karimi-Fard, 2003). Figure 2.10 shows an intermediate control volume considering 6 fractures with

various thicknesses and three fracture intersection CVs. For detailed information on making the connectivity lists, see (Razavi et al, 2011).

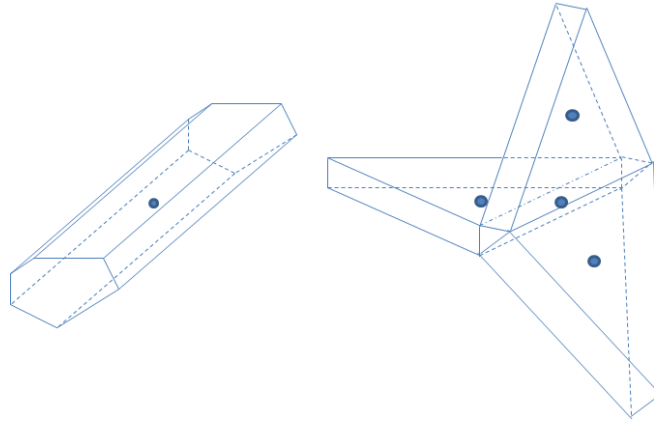


Figure 2.10: a) Intermediate CV which is the intersection of 6 fractures with different thicknesses b) Three intersecting fracture CVs (Razavi et al, 2011)

2.12 Solving the Pressure Equation: The Coefficient Matrix Structure

The pressure equation, Equation 2.10, is applied for all cells. This results in a system of equations and a matrix of coefficients including transmissibility values. For structured grids, the coefficient matrix is symmetric but in the case of unstructured grids, symmetry is not preserved and the matrix is not well defined (Bajaj, 2009).

The dimension of this matrix is $N \times N$ where N is the sum of the number of tetrahedrons in an unstructured 3D mesh plus the number of fractures in the domain. It consists of matrix-matrix transmissibility, matrix-fracture transmissibility and fracture-fracture transmissibility matrix which are all assembled together in one matrix, Figure 2.11.

By applying the information presented in the data lists including the fractures and matrix permeabilities, normal vectors, areas and centroids of the faces of tetrahedrons, centroid (barycentre) of each tetrahedron, etc and also connectivity lists information, the assembled transmissibility matrix including matrix-matrix assembly, fracture-matrix assembly and fracture-fracture assembly is calculated. The next step is to select a solver to solve the pressure equations.

Matrix - Matrix Assembly	Matrix -Fracture Assembly
Transient of Matrix - Fracture Assembly	Fracture - Fracture Assembly

Figure 2.11: Transmissibility matrix for a DFM meshed by unstructured grids

2.13 Biconjugate Gradients Stabilized Method for Solving Systems of Equations

To solve the non-symmetric coefficient matrix at each time step, the Biconjugate Gradients Stabilized method (BCGSTAB) could be used. It is an iterative method and is available in MATLAB by $X = \text{bicgstab}(A, b)$. It attempts to solve the system of linear equations $AX = b$ for X , which are the pressure values including the matrix and fracture pressures. The N by N coefficient matrix A is a matrix that is square, large and sparse. The column vector b has length N and includes source/sink and boundary condition terms. By calculating the pressure values at each time step, b is updated and new values for pressures are obtained. The coefficient matrix does not change. The right hand side values will be zero for fracture grids; source/sink and boundary condition terms will be considered for matrix grids only. As an example, for an isolated flow system, the condition $u \cdot n = 0$ should be satisfied at the reservoir boundary (Aarnes J., 2005); where u is the Darcy velocity and n is the normal vector of the boundary surface.

2.14 Convergence Analysis

The accuracy of the solution could be tested by a solution obtained from a very fine mesh reference solution. Different degrees of grid refinement could be considered at this stage. By increasing the mesh refinement, the solution should converge to the

reference solution. In this case, single phase flow equations are solved to find the pressure solution. For convergence analysis, the mean pressure error can be computed (Bajaj, 2009):

$$E(p) = \frac{||P_{ref} - P||^2}{||P_{ref}||^2} \quad (2.13)$$

P_{ref} and P are pressure values on the reference and non-reference mesh respectively.

2.15 Conclusion

The chapter reviewed structured and unstructured grid types and also described how the finite volume form of mass conservation law is applied to model single phase flow. The finite volume simulator is mainly based on the connectivity lists. Creating the connectivity lists requires some preprocessing effort especially for 3D unstructured grids. For a discrete fracture model by listing the connections, the transmissibility is calculated in three separate parts, for matrix-matrix, matrix-fracture and fracture-fracture connections and flow simulation follows the transmissibility calculation.

3 Scaling up of Effective Absolute Permeability

A common problem in Geostatistical reservoir modeling is the calculation of effective permeability of coarse grids to represent higher resolution heterogeneity. The FLOWSIM program (Deutsch, 1989) has been used since the mid 1980s for this purpose. This chapter reviews its implementation and recommends some changes including the application of a new iterative solver (SIP - the strongly implicit procedure) and consideration of new convergence criteria that permit reliable results without excessive computational effort. The results are checked with a direct solver.

3.1 Motivation for Scale up

To optimize reservoir performance and forecast recovery, reservoir simulation is conducted on a numerical model that includes reservoir properties and geometry as input data. There is a significant scale difference between the flow simulation model and the data used to construct the geologic model; the geologic model (geomodel) has many more grid cells to represent high resolution features seen in the original data. The geomodel often captures complex geological features with approximately 10^7 grid cells (Chen, 2009).

In reality, multiple realizations should be considered to quantify uncertainty. To facilitate the use of multiple realizations, the geomodel is upscaled to a coarser resolution for fast simulation. By upscaling, the heterogeneous medium is replaced with a more homogenous medium at the chosen grid size where small scale heterogeneities are represented with upscaled effective values. In subsurface flow modeling, the most important property to upscale is permeability, due to its first order influence on predicted rates and flow performance. Comprehensive reviews of current methods are given in Farmer (2002), Durlofsky (2005), and Gerritsen and Durlofsky (2005). Figure 3.1 shows a simple schematic of permeability upscaling.

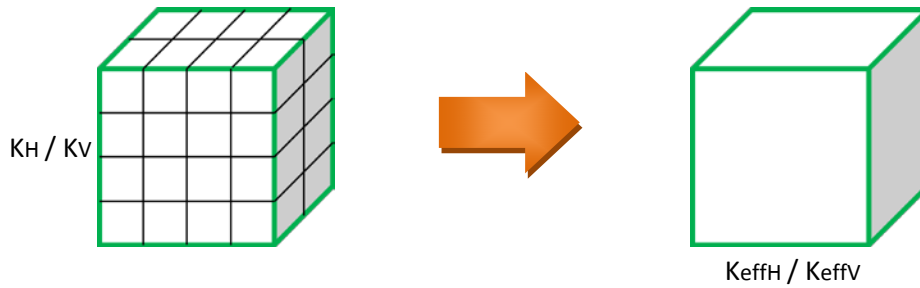


Figure 3.1: Left: Fine resolution model, Right: Coarse resolution with effective properties

3.2 FLOWSIM Program

FLOWSIM is a program for single phase flow-based permeability scale-up within a stratigraphic layer. The program takes a fine scale 3-D Cartesian grid of permeability and scales it to a coarser 3-D Cartesian grid of effective permeabilities. The effective permeability in each direction is calculated by solving the steady-state single-phase flow equations with no flow boundary conditions (Deutsch, 1989 and 1999).

3.3 Single Phase Flow Upscaling

Volumetric fractions such as porosity average linearly, that is, the effective porosity is calculated as an arithmetic average of the constituent porosities. To get the effective directional permeability values, however, the single phase flow upscaling technique is used within the FLOWSIM program. Upscaling is not applied on relative permeability which is a two-phase flow parameter. This method is referred to as single-phase upscaling (Durlafsky, 2005). There are many confounding factors in the scale up of relative permeabilities and current best practice is to use facies dependent relative permeability curves with scaled up absolute permeability.

3.4 Motivation

The FLOWSIM program considers Linear Successive Over Relaxation (LSOR) to solve the pressure equation and compute effective absolute permeability. There are other solvers that could be considered.

The Strongly Implicit Procedure (SIP) is another iterative solver that is recommended for flow related problems with large sparse matrix (Weinstein and Stone, 1969). There are also direct solution techniques. The GBAND direct solver (Aziz and Settari, 1979) has been added to the FLOWSIM program to get the exact solution of the pressure equations albeit at greater computational cost. Knowledge of the exact solution permits simpler analysis of the convergence of iterative solvers to the exact solution. Comparative studies are conducted on different permeability fields to study the effectiveness of the LSOR and SIP algorithms.

3.5 Problem Formulation: Pressure Matrix in the FLOWSIM program

The input to the FLOWSIM program is a fine scale 3D Cartesian grid of the permeability in X, Y and Z directions (K_x , K_y and K_z) and it is scaled to a coarser 3D Cartesian grid of effective permeability that are denoted as K_{effX} , K_{effY} and K_{effZ} . The arithmetic, geometric and harmonic averages are also reported for checking. As mentioned earlier, the effective permeability in each direction is calculated by solving the steady-state single-phase flow equations with no flow boundary conditions (Deutsch, 1989).

The effective permeability in the X direction is calculated by Equation 3.1 that is derived from Darcy's Law. The n_x , n_y and n_z are model discretization numbers in X, Y and Z directions and q_{ave} is the average of cumulative input and output flow rates. p_{in} and p_{out} are pressures of input and output boundary grids which are set respectively to 0 and 100 for the calculations.

$$K_{effX} = 2q_{ave} \frac{n_x}{n_z n_y (p_{in} - p_{out})} \quad (3.1)$$

$$q_{ave} = \frac{(q_{in} + q_{out})}{2} \quad (3.2)$$

q_{in} and q_{out} are the cumulative input and output flow rates which are calculated by Equations 3.3 and 3.4.

$$q_{in} = \sum_{inlet\ blocks} (p_{in} - p_i) k_i \quad (3.3)$$

$$q_{out} = \sum_{outlet\ blocks} (p_i - p_{out}) k_i \quad (3.4)$$

p_i and k_i are the pressure distribution and permeability distribution on the grids. To obtain q_{in} and q_{out} , we need to know the pressure distribution of the model which is where the solver is used. The solver solves a large system of pressure equations and the pressure field necessary to calculate the effective permeability is obtained. The resulting pressure field has values between p_{in} and p_{out} . It is worth to mention that q_{in} and q_{out} have to be the same; any difference is an indication of numerical instability.

Calculations are conducted in the X, Y and Z directions separately to get the effective permeability in each direction. Figure 3.2, Figure 3.3 and Figure 3.4 show one model when calculating the effective permeability in different directions.

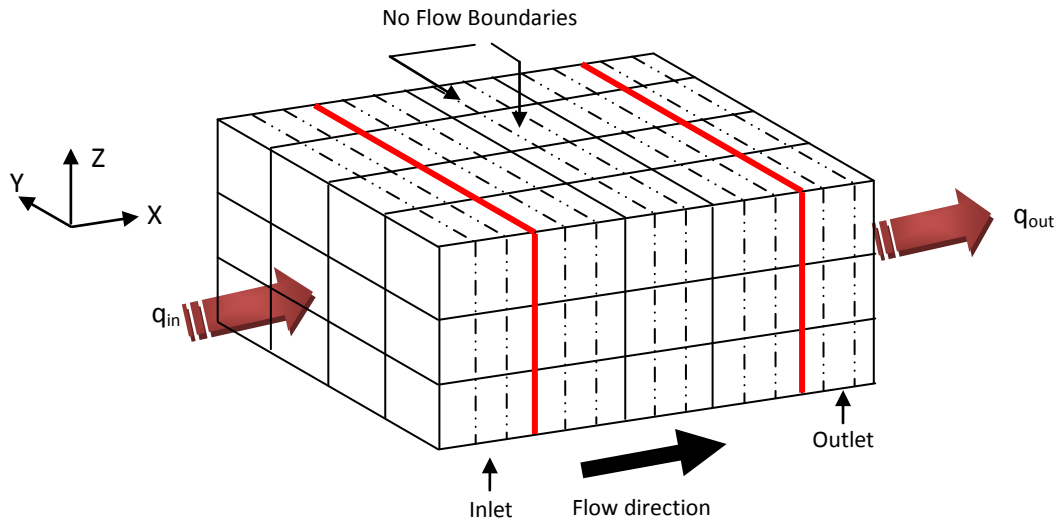


Figure 3.2: Calculating K_{effX} : grid faces in Y and Z directions are no flow boundaries.

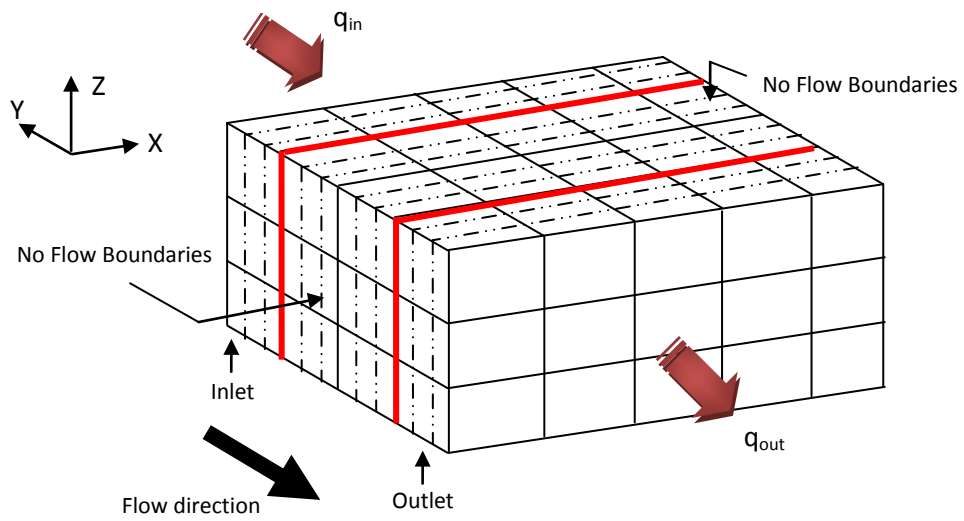


Figure 3.3: Calculating KeffY: Grid faces in X and Z directions are no flow boundaries.

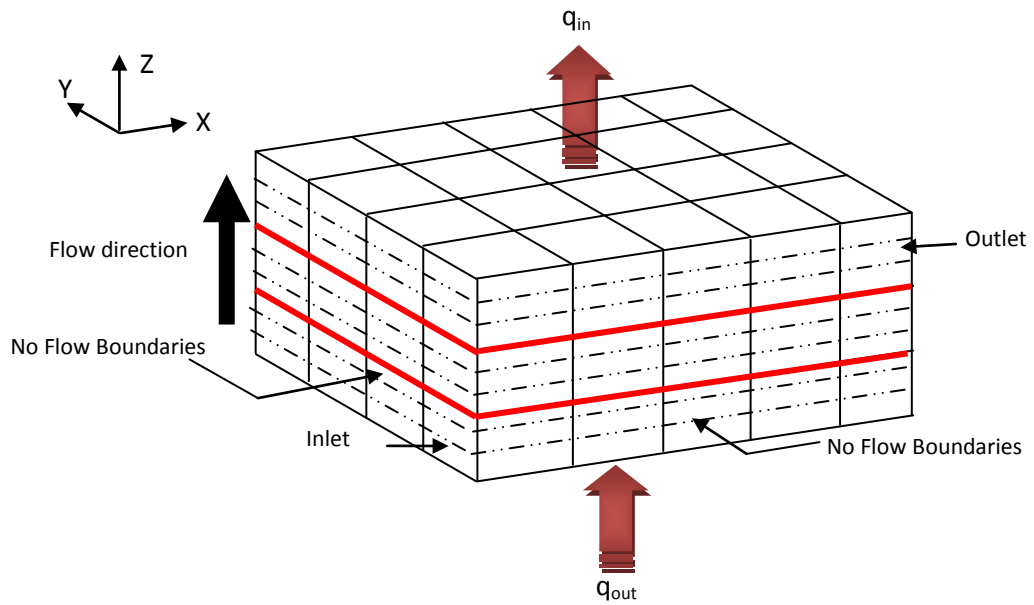


Figure 3.4: Calculating KeffZ: Grid faces in X and Y directions are no flow boundaries.

In a structured 3D model, there are six neighbors for each grid block except at the boundaries of the model. The pressure at the block center is related to the pressures of the adjacent blocks through the pressure equation, Figure 3.5. There is a separate pressure equation for each grid block in the model which results in a 7 diagonal pressure matrix for each set of boundary conditions. Grid indexing is an important point that should be considered carefully not only in making the pressure equation but also when applying the linear solver. Different indexing will affect the values on the matrix diagonals. If (i, j, k) is the index of the grid at the center, the indices of the diagonals are shown in Table 3.1.

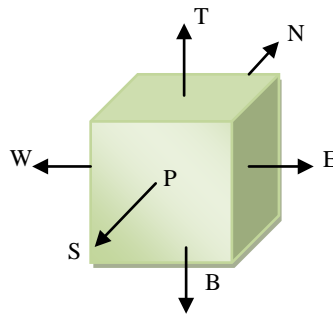


Figure 3.5: Each grid block has 6 neighbors.

Table 3.1: Indices of the Pressure Matrix Diagonals

Diagonal	Index	Corresponding Array
Bottom diagonal	$(i, j, k - 1)$	AB
South diagonal	$(i, j - 1, k)$	AS
West diagonal	$(i - 1, j, k)$	AW
Main diagonal	(i, j, k)	AP
East diagonal	$(i + 1, j, k)$	AE
North diagonal	$(i, j + 1, k)$	AN
Top diagonal	$(i, j, k + 1)$	AT

In the FLOWSIM program, a 1D index for each grid center with a 3D index (i, j, k) is calculated by:

$$ip = (k - 1) \times nx \times ny + (j - 1) \times nx + i \quad (3.5)$$

The above indexing results in the pressure Equation 3.6 for each grid block with the ip index:

$$\begin{aligned}
 &P(ip - nx \times ny) \times AB(ip) + P(ip - nx) \times AS(ip) + P(ip - 1) \\
 &\quad \times AW(ip) + P(ip) \times AP(ip) + P(ip + 1) \times AE(ip) \\
 &\quad + P(ip + nx) \times AN(ip) + P(ip + nx \times ny) \times AT(ip) \\
 &= 0
 \end{aligned} \tag{3.6}$$

If the 1D index is calculated as it is in Equation 3.7, then the pressure equation would change to that which is presented by Equation 3.8.

$$ip2 = (k - 1) \times nx \times ny + (i - 1) \times ny + j \tag{3.7}$$

$$\begin{aligned}
 &P(ip2 - nx \times ny) \times AB(ip2) + P(ip2 - 1) \times AS(ip2) + P(ip2 - ny) \\
 &\quad \times AW(ip2) + P(ip2) \times AP(ip2) + P(ip2 + ny) \times AE(ip2) \\
 &\quad + P(ip2 + 1) \times AN(ip2) + P(ip2 + nx \times ny) \times AT(ip2) \\
 &= 0
 \end{aligned} \tag{3.8}$$

By writing the pressure equation (Equations 3.6 or 3.8) for all grids, a pressure matrix which is a large sparse matrix is generated. In the next section, the linear solvers to solve the system of pressure equations are described. The required seven diagonals are summarized in Table 3.2.

Table 3.2: Seven Diagonals of the Matrix in the FLOWSIM Program

Diagonals	AE	AW	AN	AS	AT	AB	AP
FLOWSIM	dxp	dxm	dyp	dym	dzp	dzm	D0

3.6 Solving the Pressure Equations

The performance of the two iterative solvers, SIP and LSOR are compared in this section. Comparative studies are conducted on different geological models to investigate the effectiveness of the two algorithms with respect to convergence to the exact solution.

The exact solution is obtained by applying the GBAND algorithm which is a direct solver suitable for banded matrices.

3.6.1 Direct Solver

GBAND is a direct solver for the solution of banded matrices without pivoting. The input of the algorithm is a one dimensional array containing the band of the diagonal matrix sorted by rows. The required dimension of the array is:

$$\text{Band dimension} = O \times (2 \times M + 1) - M \times M - M \quad (3.9)$$

Where M is the number of diagonals above the main diagonal and O is the number of the equations. The number of the diagonals above and below the main diagonal is the same. Detailed information can be found in the book of Aziz and Settari (Aziz and Settari, 1979).

3.6.2 Iterative (indirect) Solvers: LSOR, SIP

3.6.2.1 Linear Successive Over Relaxation

Successive over relaxation (SOR) is a popular iterative method that is an accelerated version of the Gauss Seidel algorithm. Considering a 2D model with 5 points, if each iteration starts in the lower left (southwest) of the domain, the successive over relaxation method can be written as follows:

$$P_i^{n+1} = w \frac{P_i - A_{j-1} P_{j-1}^{n+1} - A_{i-1} P_{i-1}^{n+1} - A_{j+1} P_{j+1}^n - A_{i+1} P_{i+1}^n}{A_i} + (1 - w) P_i^n \quad (3.10)$$

n is the iteration counter and w is the over-relaxation factor for acceleration, it must be greater than 1. P is the pressure and A is the corresponding diagonal value. It is hard to find the optimum value for the over-relaxation factor in complex problems. In general, the value is larger for larger grids. The number of iterations will be proportional to the number of grid points in one direction, when the optimum value of the over relaxation

factor is used. When w has the value of 1, SOR reduces to the Gauss Seidel method. It is specifically designed for algebraic equations and usually converges in a small number of iterations (Ferziger, 2002).

3.6.2.2 Strongly Implicit Procedure

The Strongly Implicit Procedure (SIP) is an incomplete lower-upper decomposition method which has found use in CFD problems. It was proposed by Stone (Stone, 1968). Stone improved the convergence of incomplete lower upper decomposition SIP. The Strongly Implicit Procedure usually converges in a small number of iterations as well. The SIP method is also suitable as a preconditioner for conjugate gradient methods and as a smoother for multigrid method (Ferziger, 2002). A 3D vectorized version of SIP has been given by Leister and Peric in 1994 (Leister and Peric, 1994). The rate of convergence in Stone's method can be improved by changing Stone's parameter (α), which is a problem dependent parameter, from iteration to iteration. Investigating the dependence of the convergence behavior on the α parameter between 0.92-0.94 were found to give results close to the optimum ones for a wide range of problems. These values are suggested for general use (Leister and Peric, 1994). In the FLOWSIM program, the value of α has been determined based on descriptions in Weinstein's paper (Weinstein and Stone, 1969).

3.7 Stopping Criterion

A stopping (convergence) criterion is needed to determine when to stop the iteration process. Ideally, the distance of the last iteration to the true solution could be known. The difference between a computed iterative solution and the true solution of a linear system is a measure of the error. In practice, we do not have the true solution, but we can solve it in test cases to establish the convergence properties of the different iterative methods. It would be reasonable to choose the iterative algorithm with less CPU time for the same convergence properties.

3.8 Applying the Algorithms

All the calculations are conducted on the modified FLOWSIM program that currently includes three solvers: LSOR, SIP and GBAND. The goal is to investigate the convergence behavior of the SIP and LSOR algorithms when dealing with various permeability fields with different levels of complexity. The rapid convergence of an iterative method is the key factor for its effectiveness. The convergence is defined as the reduction of the iteration error below some specific value of tolerance (Ferziger, 2002).

3.9 Stopping (Convergence) Criteria – Original Version

The stopping criterion for the algorithms is the maximum change made to the pressure field in a given iteration. If the change is low enough (less than the input residual), then the pressure field is considered to be close enough to the exact solution. When we know the exact solution by applying a direct solver, then we can easily check if the iterative algorithms have reached the exact solution or not. We considered the permeability error as a stopping criterion. When it is below 0.1 %, the algorithms stop. The required level of accuracy for pressure from iteration to iteration has been also considered as 0.1% that gives acceptable results. The iteration errors are calculated by Equations 3.11 and 3.12. $Kerror(i)$ and $Perror(i)$ are presented as the permeability error and pressure error at each iteration respectively. The permeability convergence and pressure convergence are presented through plotting the errors versus iterations while converging to the exact solution.

$$Kerror(i) = \frac{|Keff_i^{calc} - Keff^{true}|}{Keff^{true}} \cdot 100 \quad (3.11)$$

$$Perror(i) = \frac{1}{N} \sum_{n=1}^N \frac{|P_n^i - P_n^{true}|}{P_n^{true}} \cdot 100 \quad (3.12)$$

N is total number of the grids. $Keff^{true}$ and P_n^{true} are exact effective permeability values and exact pressure field obtained by GBAND algorithm. $Keff_i^{calc}$ is the effective

value calculated by an iterative algorithm at each iteration and P_n^i is the pressure distribution obtained at iteration i by the iterative solver.

3.10 Case Studies

Four 3D cases are put to test. The first, third and fourth cases are generated in MATLAB and the second case is a 10 by 10 by 11 model generated by the SGSIM program in GSLIB. The first and fourth cases are 10 by 10 by 10 models and the third one is a 10 by 10 by 11 model. Figure 3.6 show the geological models under investigation. For the 1st, 2nd and 4th cases, 1mD and 1000mD are assigned respectively to the low and high permeability grid cells.

The error plots for each model are generated in MATLAB by loading the output files of the FLOWSIM program. To apply the GBAND algorithm, it is necessary to know the dimensions of the diagonals. The 7 diagonals' dimensions based on the chosen indexing in pressure equation are presented in Table 3.3.

Table 3.3: Dimension of the Pressure Matrix Diagonals

Indexing	$ip = (k - 1) \times nx \times ny + (j - 1) \times nx + i$	$ip2 = (k - 1) \times nx \times ny + (i - 1) \times ny + j$
Dimension	$dim(AB) = (nx \times ny \times nz) - (nx \times ny)$	$dim(AB) = (nx \times ny \times nz) - (nx \times ny)$
	$dim(AS) = (nx \times ny \times nz) - (nx)$	$dim(AS) = (nx \times ny \times nz) - (1)$
	$dim(AW) = (nx \times ny \times nz) - (1)$	$dim(AW) = (nx \times ny \times nz) - (ny)$
	$dim(AP) = (nx \times ny \times nz)$	$dim(AP) = (nx \times ny \times nz)$
	$dim(AE) = (nx \times ny \times nz) - (1)$	$dim(AE) = (nx \times ny \times nz) - (ny)$
	$dim(AN) = (nx \times ny \times nz) - (nx)$	$dim(AN) = (nx \times ny \times nz) - (1)$
	$dim(AT) = (nx \times ny \times nz) - (nx \times ny)$	$dim(AT) = (nx \times ny \times nz) - (nx \times ny)$

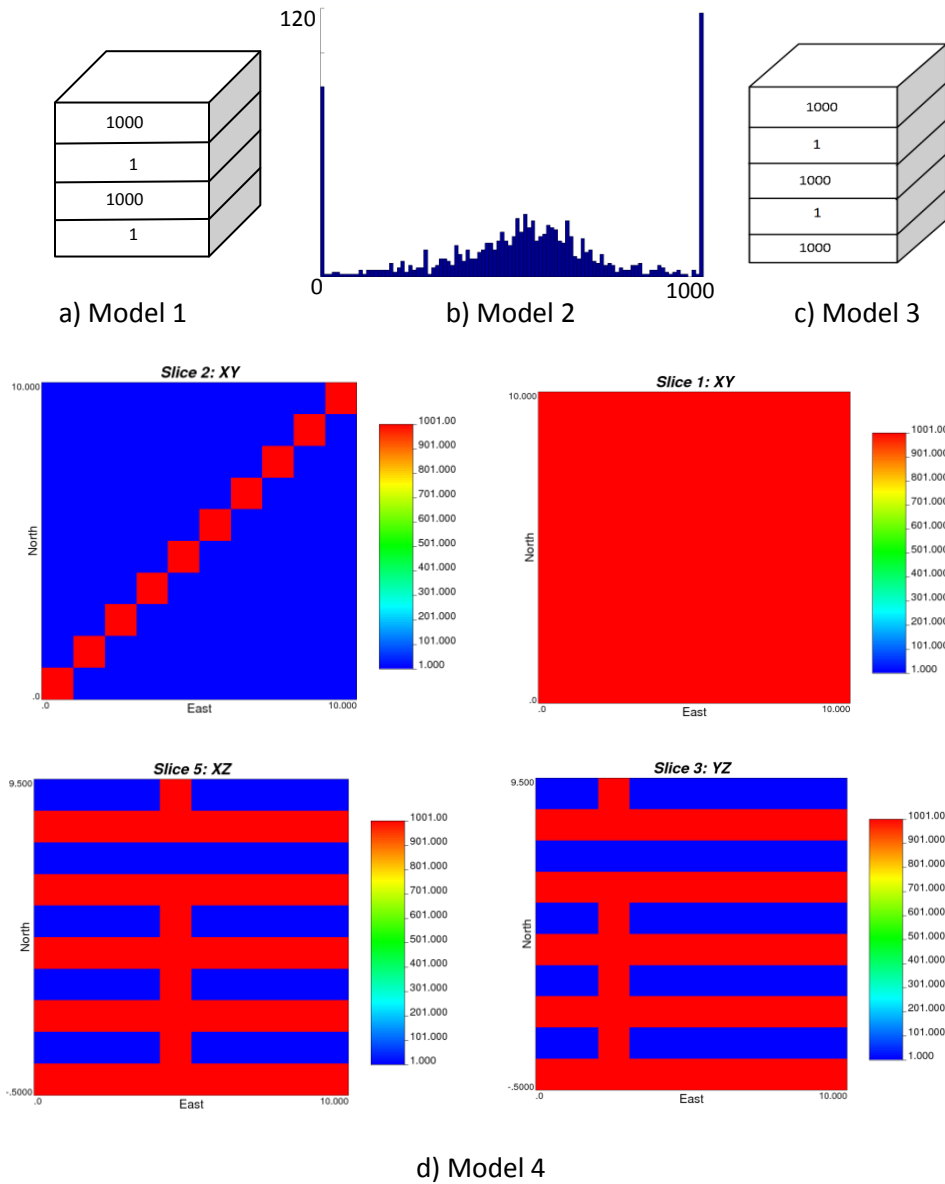


Figure 3.6: Geological models under investigation

Knowing the exact solution calculated by the GBAND algorithm, the permeability error and the pressure error (when compared to the exact solution) are calculated in each iteration. Note that the error is different in the X, Y and Z directions. Furthermore, the CPU time is recorded for all calculations. The resulting graphs and tables are presented for each case separately. The following steps are taken in each case:

- 1) Run FLOWSIM by applying GBAND to get the exact pressure profiles and exact upscaled permeability values in X, Y and Z directions.

2) Input the exact pressure solution and effective permeability solution to the FLOWSIM in X, Y and Z directions to measure the error when applying the LSOR and SIP.

3) Run LSOR with 10000 iterations to get the permeability and pressure convergence error report in all directions.

4) Once again run LSOR by considering the stopping criteria and measuring the CPU time in all directions.

5) Run SIP with 10000 iterations to get the permeability and pressure convergence error report in all directions.

6) Once again run SIP by considering the stopping criteria and measuring the CPU time in all directions.

The calculated effective permeabilities by SIP and LSOR in all directions are the same as the exact effective permeability calculated by the direct solver, see Table 3.4. The measured CPU time when running the algorithms is tabulated in Table 3.5, Table 3.6 and Table 3.7. Kh is obtained by arithmetic averaging of KeffX and KeffY. Ka, Kg and Kha are arithmetic, geometric and harmonic averages respectively. A summary of the error plots for different cases are presented in the next section.

Table 3.4: Exact Solutions Resulted by GBAND

	KeffX	KeffY	KeffZ	Kh	Ka	Kg	Kha
Case 1	500.5	500.5	1.718	500.5	500.5	31.623	1.998
Case 2	545.909	545.909	1.890	545.909	545.909	43.288	2.197
Case 3	436.977	440.731	357.521	438.854	538.079	185.906	0.014
Case 4	501.945	501.945	7.891	501.945	540.460	41.687	2.171

Table 3.5: CPU Time (Seconds) and the Number of Iterations to Converge

Case 1: Stopping Criterion (SC) <= 0.1%

	CPU time X	CPU time Y	CPU time Z	niterX / S.C.	niterY / S.C.	niterZ / S.C.
SIP	0.0468	0.0468	27.895	12 / 0.00055	12 / 0.00055	> 10e5/13.45
LSOR	0.0624	0.0624	31.637	48 / 0.00072	48 / 0.00072	> 10e5 /13.99
GBAND	0.234	0.2184	0.234	Direct Solver		

Table 3.6: CPU Time (Seconds) and the Number of Iterations to Converge

Case 2: $SC \leq 0.1\%$

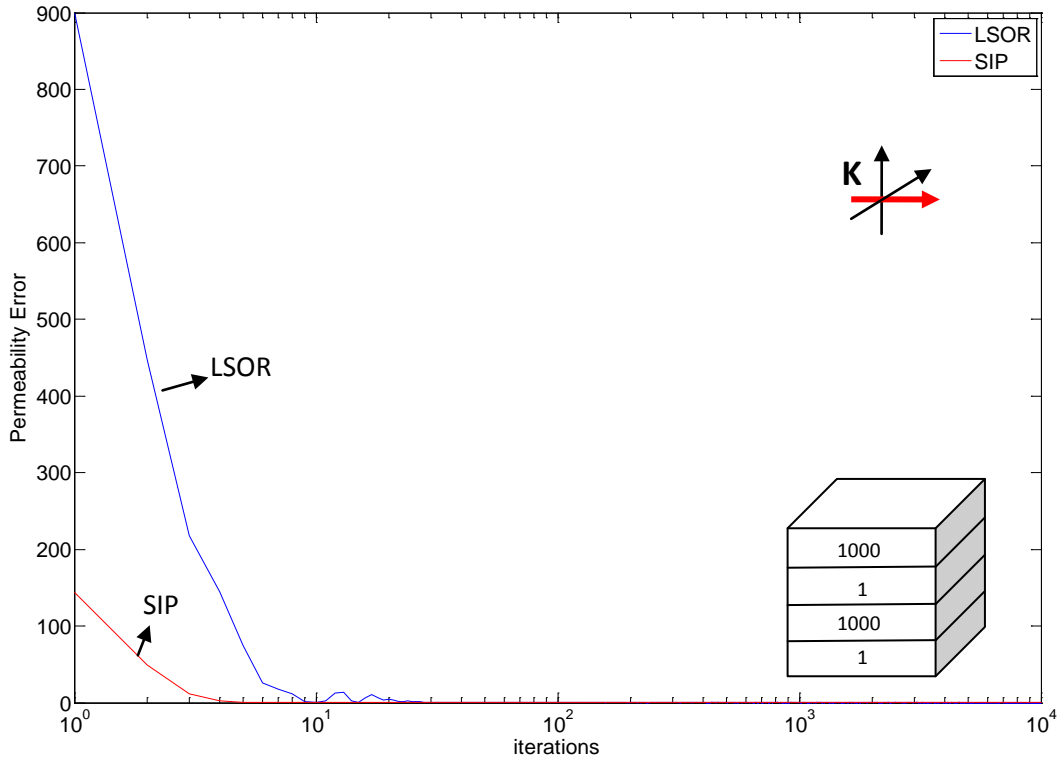
	CPU time X	CPU time Y	CPU time Z	niterX	niterY	niterZ
SIP	0.0312	0.0312	0.2496	11	11	499
LSOR	0.0312	0.0312	0.5616	48	48	1511
GBAND	0.2675	0.231	0.2675	Direct Solver		

Table 3.7: CPU Time (Seconds) and the Number of Iterations to Converge

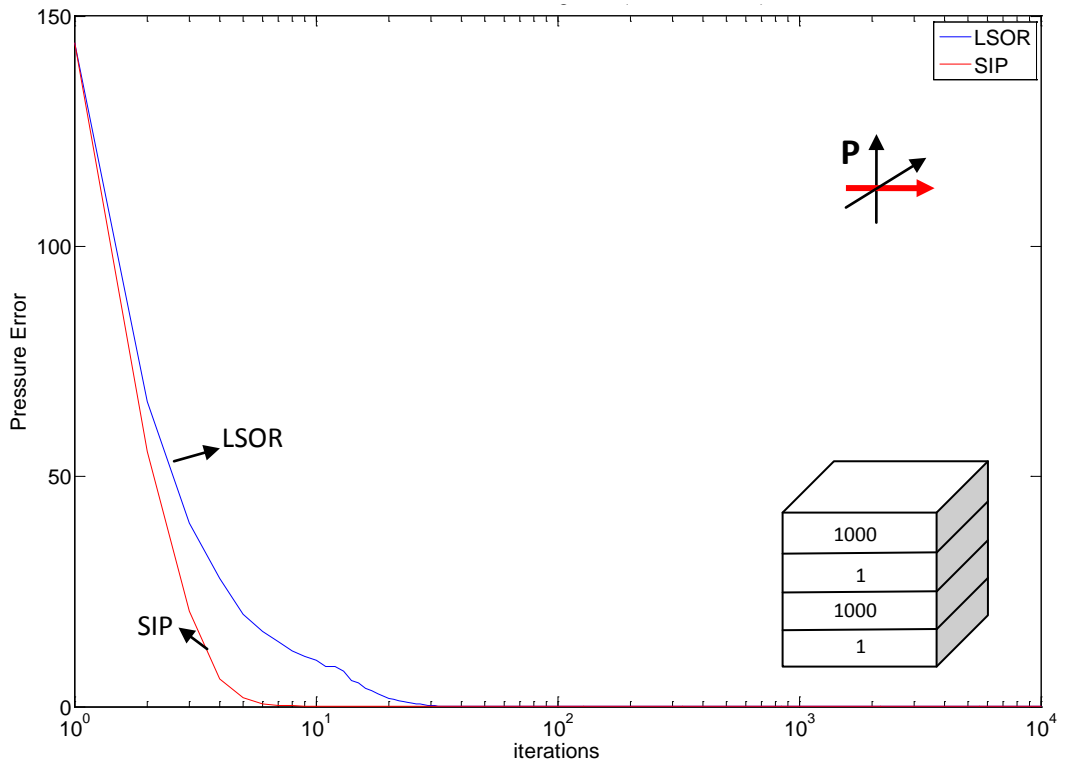
Case 3: $SC \leq 0.1\%$

	CPU time X	CPU time Y	CPU time Z	niterX	niterY	niterZ
SIP	0.0312	0.0468	0.0468	21	14	24
LSOR	0.0312	0.0468	0.0312	44	49	51
GBAND	0.2496	0.2496	0.2496	Direct Solver		

Comparative studies are conducted for all models on the pressure and permeability convergence to the exact solution for the iterative algorithms and in X, Y and Z directions. Since the error plots are similar for the models, only some representative ones are presented. The SIP and LSOR error plots have been shown in red and blue, respectively.



a) KeffX convergence: LSOR vs. SIP (Model HSB10.out)



b) PX convergence: LSOR vs. SIP (Model HSB10.out)

Figure 3.7: KeffX and PX convergence for case 1

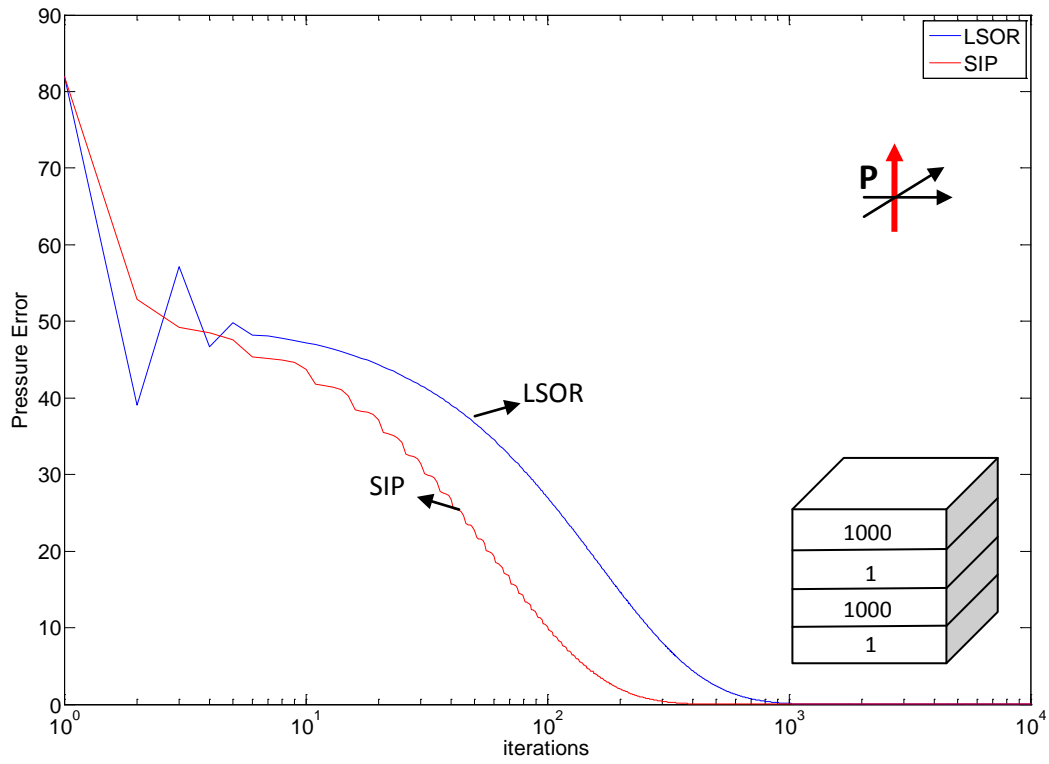


Figure 3.8: PZ convergence: LSOR vs. SIP (Model HSB10.out)

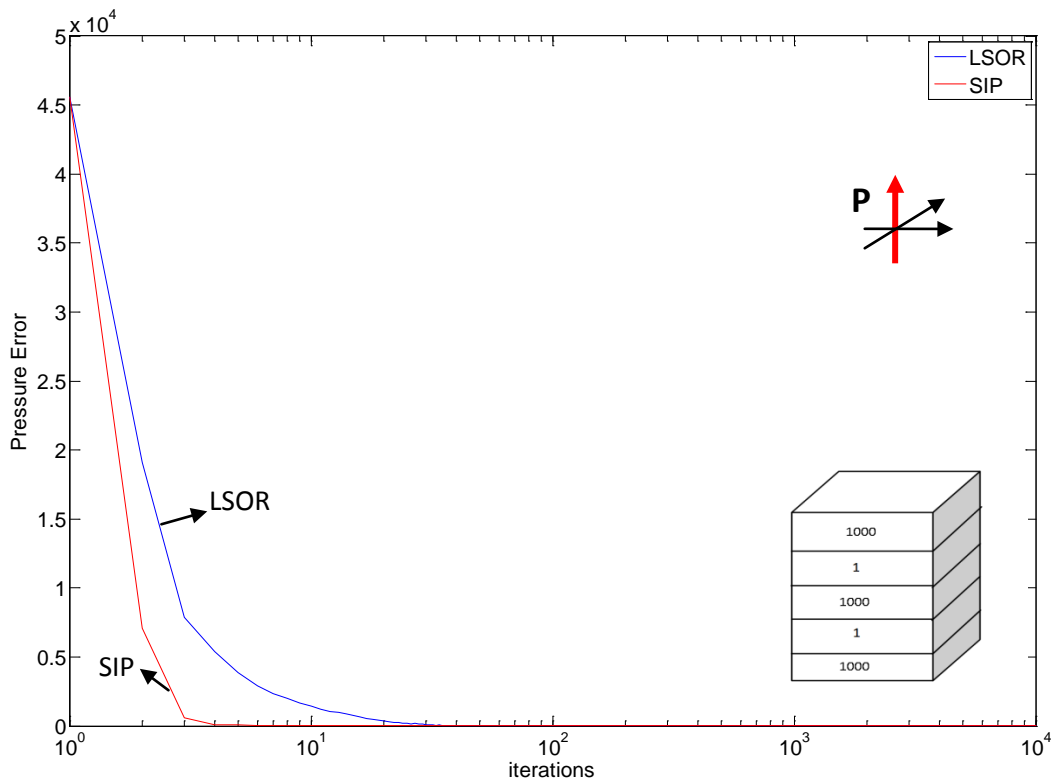


Figure 3.9: PZ convergence: LSOR vs. SIP (Model HSB11.out)

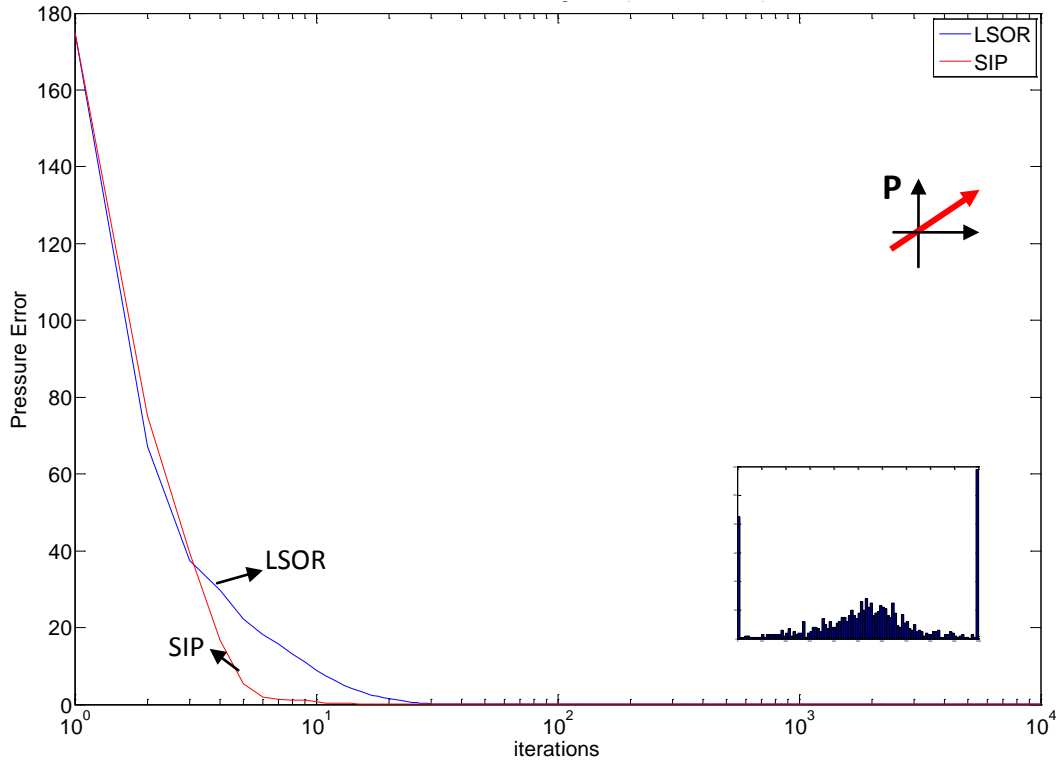


Figure 3.10: PY convergence: LSOR vs. SIP (Model4.out)

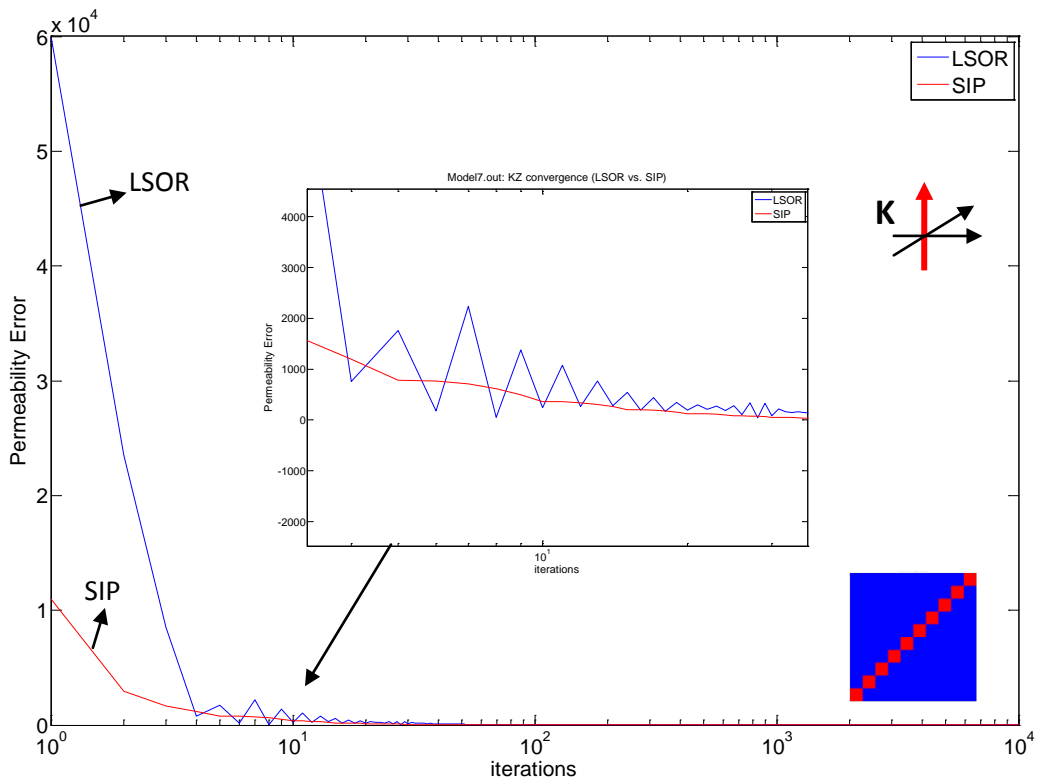


Figure 3.11: KeffZ convergence: LSOR vs. SIP (Model7.out)

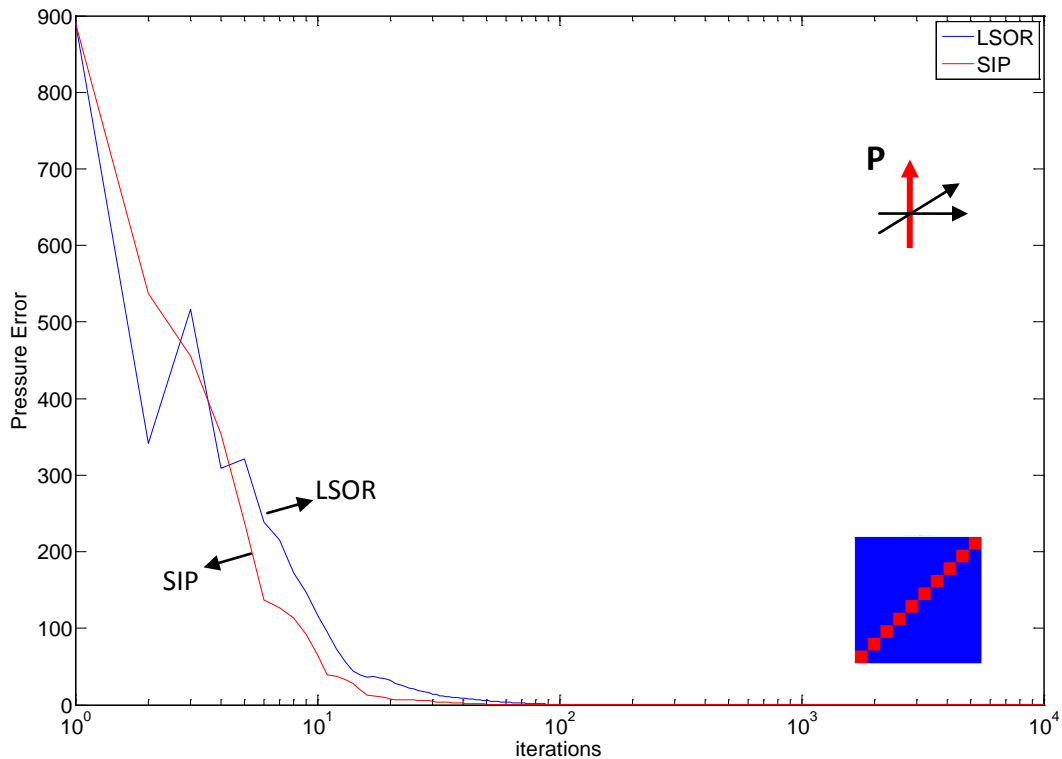


Figure 3.12 :PZ convergence: LSOR vs. SIP (Model7.out)

Looking at these results, the following points are worthy of mention:

a) Calculations in the Z direction of the first case (Figure 3.6) is not an easy problem since the algorithms need more iterations to converge; see Figure 3.8.

b) The difference between the pressure convergence behaviour of the algorithms for the first, second and 4th cases in Z direction is interesting. By looking at Figure 3.12 for the fourth case, Figure 3.8 for the first case and Figure 3.9 for the third case, we observe that when there are low permeability layers in the model, the algorithms require more effort to satisfy the stopping criterion and also the algorithms have unpredictable and relatively unstable behaviour when converging to the exact solution. When in each layer there are a few low permeability grids, as in the fourth case, the algorithms converge to the exact solution more easily compared to the first case where the entire bottom layer is low permeability. The difference between the first and second cases is in an additional low permeability layer at the bottom of the first case that results in a different behaviour of the algorithms, see Figure 3.8 and Figure 3.9. Figure 3.10 also shows stable convergence of the algorithms to the exact solution in case of the model generated with SGSIM program.

3.11 Conclusion

In this chapter, a comparative study has been conducted on two iterative algorithms in the FLOWSIM Program to show the performance of the linear successive over relaxation and strongly implicit algorithms. SIP and LSOR are iterative solvers which are widely used to solve very large and sparse systems of linear equations. The exact solution of the system of the pressure equations is obtained by applying the direct solver, GBAND, in the FLOWSIM program. The pressure convergence and permeability convergence to the exact solution have been investigated for the SIP and LSOR. CPU time has been also measured when applying SIP, LSOR and GBAND. Based on the presented case studies, it is clear that:

- 1) Looking at Table 3.4 to Table 3.7, the direct solver generally takes much longer than iterative solvers. In case of first model Z direction, direct solver's CPU time is less compared with iterative algorithms.
- 2) Looking at Figure 3.7 to Figure 3.12, both iterative algorithms are converging to the exact pressure solution for all cases at different directions.
- 3) The memory cost of the algorithms is relatively insignificant since only the banded part of the matrix is kept.
- 4) Looking at Figure 3.7 to Figure 3.12, the level of the residuals for SIP reduces higher orders in less iterations and SIP converges faster than LSOR for the examined cases.
- 5) SIP required less computational effort (less iterations) than LSOR while the CPU time for each inner iteration of SIP is more expensive than LSOR.
- 6) Looking at the K convergence graphs, SIP is more stable with fewer fluctuations while converging to the exact solution. Less CPU time and stability convergence could be mentioned as considerable advantages of the SIP.

In conclusion, the FLOWSIM program should be used with the SIP solver as it converges quicker.

4 Representation of Geologic Features with Grids

Full field reservoir flow simulation considers on the order of one million grid blocks. Small scale heterogeneities at scales less than meters cannot be explicitly represented by these blocks. These small scale features are captured in effective properties at the grid block scale. Reservoir features (heterogeneities) that are large with respect to the grid size can be represented as discrete objects, that is, each grid block is in or out of the feature. Reservoir features that are smaller than the grid block size must be represented as proportions of the features within the grid block, that is, each grid block contains a continuous proportion of the feature. For a fixed grid size, large features are represented discretely and small features are represented continuously. Some features are in transition from discrete to continuous. The grid size that becomes large with respect to the feature size is sometimes referred to as representative elementary volume (REV). Transition from the discrete domain, where there is little mixing, to the continuous domain, where they are all mixed, is important to investigate since it is important to adopt the most suitable modeling approach. One goal of this work is to quantify the scales of the discrete, transition and continuous regimes. For this purpose, some models at different domain and object sizes are constructed and the progression from discrete to transition and also from transition to continuous is explored. A modified version of the classical REV plot proposed by Bear (1972) is proposed. The proposed model is presented for a fluvial depositional system.

4.1 A Classical Definition of Representative Elementary Volume (REV)

A representative elementary volume (Zhang, 2000) is a volume within which the statistics of the quantity of interest are homogenous and stationary. A representative elementary volume was originally defined by Bear (1972). Based on Bear's theory, it should be large enough to capture a representative amount of heterogeneity. The notion of an REV relates to the concept of a length scale. Different factors influence the determination of the length scale of a process, including geological heterogeneity, transport phenomena and fluid flow, and chemistry and process design (Gates and

Wang, 2012). Our focus in this research is on geological heterogeneity and its direct effect on flow.

Figure 4.1 illustrates the classical explanation of REV plot (Bear, 1972). The plot shows the average of porosity on the Y-axis and the averaging volume V on the X-axis. Any other petrophysical property could be on the Y-axis. The plot illustrates that the average of the property becomes stable and constant at intermediate V which is called REV, and then fluctuates as V approaches zero (Lake et al, 2004).

The REV and any volume larger than that are considered as part of a continuous property regime where mixing is complete and continuous modeling approaches such as Gaussian simulation are applicable. In the classical REV point of view, the focus was on this part of the REV plot. As mentioned earlier, we will define discrete and transition regimes before reaching the continuous regime and propose a modified plot including three regimes; discrete, transition and continuous regimes while considering geological features' scales.

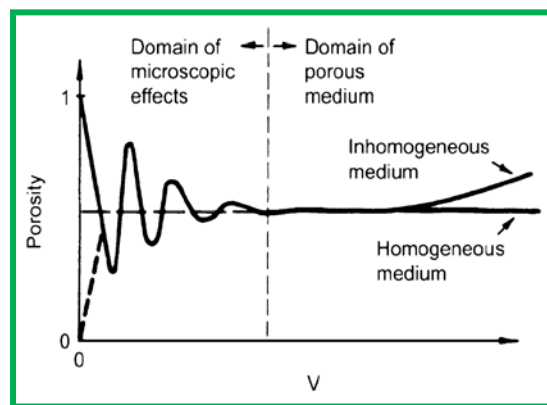


Figure 4.1: The representative elementary volume concept applied to porosity (Bear, 1972)

The "sample volume" used in the upcoming sections is a label for different grid block sizes that the point scale variability is upscaled to. An REV is a special size of the sample volume.

4.2 Definition of Discrete, Transition and Continuous Regimes

In this section, three regimes are defined: discrete, transition and continuous regimes. The size of the sample volume and the size of the geological features determine the regime.

In the case each grid block is located in or out of the feature, the dominant regime is the discrete regime and the geological feature is represented discretely, see Figure 4.2. In the discrete regime, there is little or no mixing. Grid block is the square in blue (darker color) and the geological feature has a rectangular shape in yellow (lighter color).

In the discrete regime, variability is between the grid blocks while it is homogeneous within the grid blocks. Figure 4.2 shows an example.

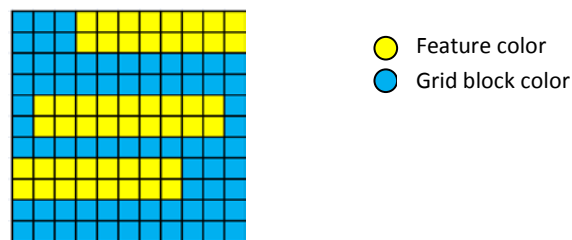


Figure 4.2: An example of the grid block size and the geological feature size in the discrete regime

In the continuous regime, there is variability within the grid blocks. In this case, the grid is large enough and the feature is small enough that, in most cases, the features are inside the grid, see Figure 4.3. In this case, continuous modeling is needed.

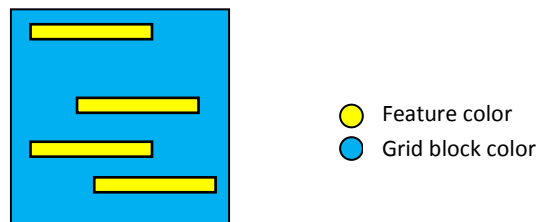


Figure 4.3: An example of the grid block size and the geological feature size in the continuous regime

In the case of the transition regime, both variability within and between grid blocks occurs. Figure 4.4 shows the change from discrete to continuous regimes. In the transition regime, features cross multiple grid blocks. The features are neither inside the grid blocks nor large with respect to the grid blocks.

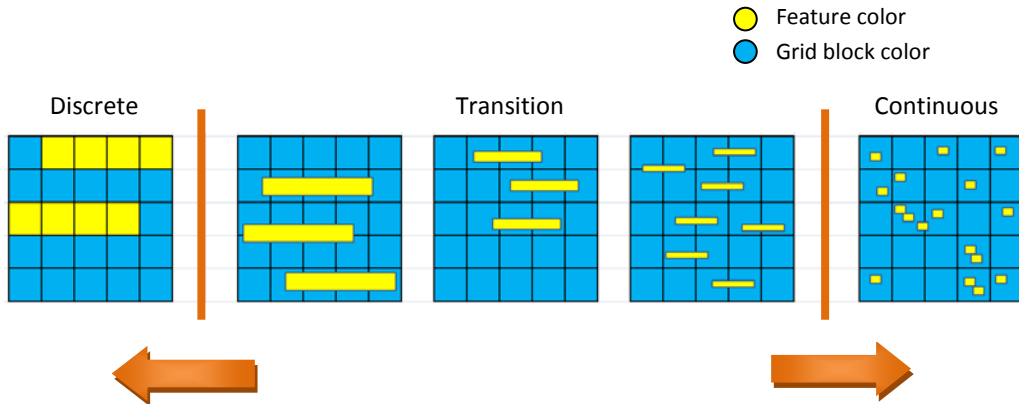


Figure 4.4: Representation of different regimes considering fixed grid size and various feature sizes

There are two equivalent methods to investigate the different regimes; fixing the grid size and changing the size of the features, as applied in Figure 4.4 or fixing the size of the feature and changing the grid size. Both these methods are fundamentally the same.

Figure 4.5 shows the regimes considering fixed feature size and various grid block sizes. A model with circular features is presented, Figure 4.5a. Part “b” of Figure 4.5 shows the grid blocks $1/15$ times the object size. The grids are mostly in or out of the circular feature; therefore, this is considered to be in the discrete regime. Grid blocks in red and light green are in the discrete regime as they are either inside or outside of the object. The grids in dark green are partly inside and partly outside of the object. Therefore, there is little mixing in this grid size but the geological feature could still be presented discretely. The mixing starts at the edges of the geological features. The grid sizes less than that are in discrete regime.

In the transition regime, some grids start to mix and some are discrete. By increasing the size of the grids, the mixing percentage is increased and at a highly significant mixing percentage, each grid block contains a continuous proportion of the feature.

Considering a grid 5 times bigger than the feature size, circular features that are smaller than the grid block size must be represented by the proportions of the features within the grid block, see Figure 4.5c. This system should be modeled continuously, as geological features cover a continuous percentage of the grid block. Grid sizes between these two sizes could be categorized as in the transition regime.

There is always some mixing of some features at a specific scale, thus upscaling and averaging are inevitable. The transition regime is a significant regime relative to the well understood discrete and continuous regimes. Putting thresholds on the boundaries of the transition regime will help understand it better. The numbers will be evaluated based on the grid block size and feature size. The upper boundary of the transition zone, that is the border between the transition and the continuous regimes, could be referred to as the representative elementary volume size.

In previous sections, the general concepts behind the research in this chapter were explained. In upcoming sections, the experiments that have been conducted on various models to evaluate the transition regime and propose a modified representation of the classical REV plot shown in Figure 4.1 will be presented.

4.3 Modifications on the Classic REV Plot

The proposed model includes three regimes discrete, continuous and a transition between the discrete and continuous regimes.

The modified REV plot looks like Figure 4.6 which is applicable to different geological systems. The Y-axis represents the scale of the geological features and the X-axis represents the grid block size. Boundaries of the regimes (Bold green lines) are evaluated. Evaluation of the grid block size vs. the geological feature size guides us to get the boundaries of the transition regime which are determined by the slope of the bold green lines in a logarithmic scale, Figure 4.6.

a) Model with circular geological features

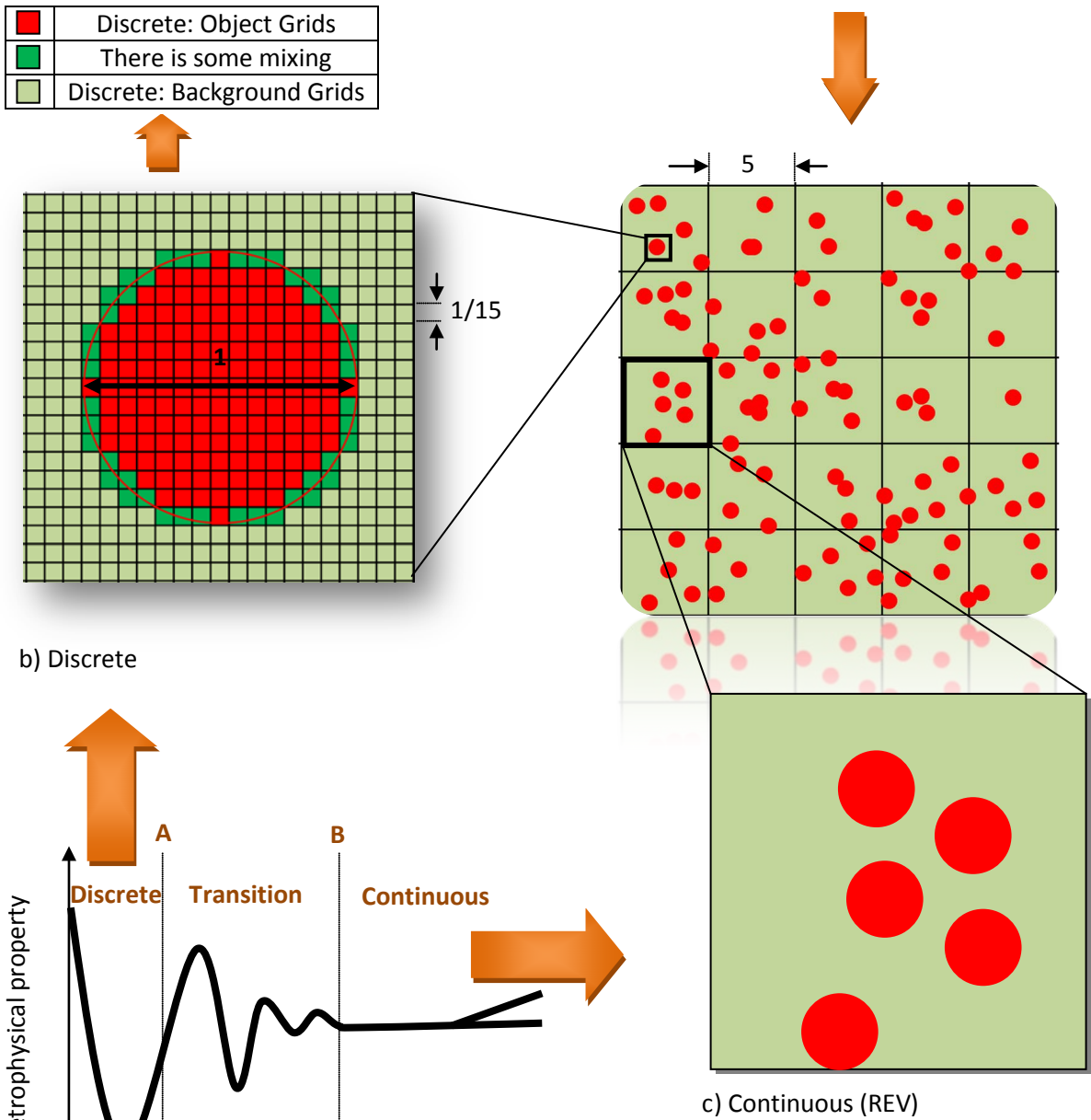


Figure 4.5: Discrete and continuous representation of the geological features: Fixed geological feature size and various grid block sizes

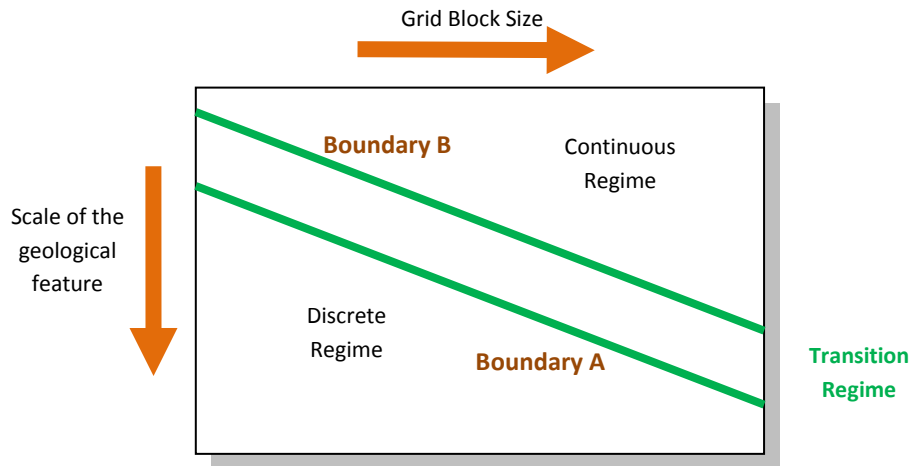


Figure 4.6: Schematic of the proposed model to modify the classic REV plot

In the next section, the criteria to characterize the thresholds of the regimes are defined to recognize: a) The discrete regime from the transition regime which is called the lower boundary of the transition regime, and b) The transition regime from the continuous regime which is called the upper boundary of the transition regime.

4.4 Criterion to Determine the Discrete – Transition Boundary

Looking back at Figure 4.6, to quantify boundary at “A”, the histogram of the point data and the increasing proportion of the upscaled values that fill in the area between the distributions of the point data, are considered. The proportion of the effective permeability between the distribution of the point data increases. The increase in the proportion in this area could be a criterion to determine the “A” boundary of the transition zone. The grid size that contains significant mixing determines the lower boundary of the transition zone. An arbitrary threshold of 15% of the grid cells having some mixing could be chosen as a reasonable value. To understand the criterion better, consider the histogram of a sample point data presented for a binary model, Figure 4.7. By upscaling, the proportion of the averaged values between the point data increases as it is shown in the histograms of averaged data at three different scales in Figure 4.8.

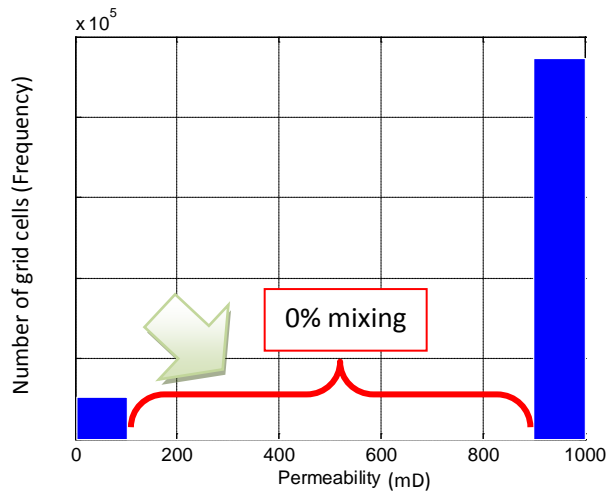


Figure 4.7: Histogram of the point data

The point is that when averaging starts, mixing starts as well. But significant mixing is important to help us determine discrete length and the start of the transition regime.

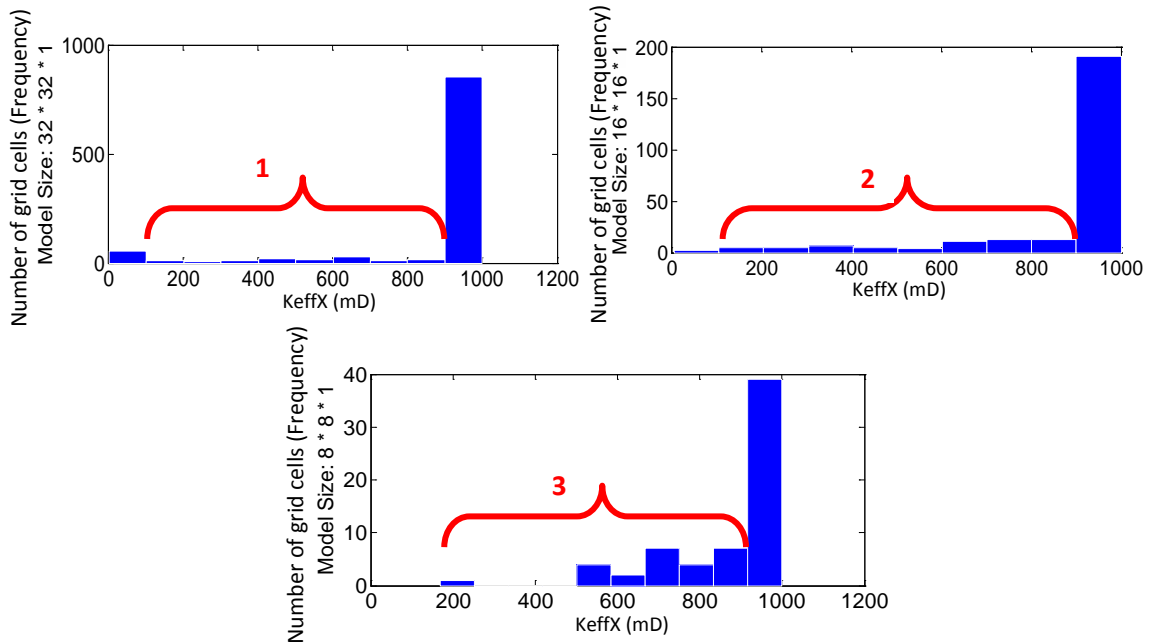


Figure 4.8: Histograms of the 3 upscaled models

Mixing occurs differently in different directions, that is, the X, Y and Z directions for a 3D model. Three sample histograms, showing three upscaled models that originated from point data in Figure 4.7, are presented in Figure 4.8 to explain the increase of mixing proportion in X direction. They help to improve the understanding of the criterion that

will be applied in the next sections. The histograms show clearly how the proportions are concentrated at the middle of the point distribution. The proportion of the mixed values increases respectively in histograms numbered 1, 2 & 3 ($1 > 2 > 3$) as the size of the selected grid for scale up increases from 1 to 3 ($1 > 2 > 3$). 15% mixing is the feasible value where in less than that the dominant regime is the discrete regime and in higher than that the dominant regime is the transition regime.

The criterion to distinguish the lower boundary of the transition zone was explained in this section. To apply the criterion, the geological feature size and the grid block size have to be connected which happens by defining a dimensionless length scale and will be explained in section 4.6.

4.5 Criterion to Determine the Transition-Continuous Boundary

Referring back to Figure 4.6, to define B boundary, the ratio of the variance of the upscaled model over the maximum variance, $\frac{\delta^2}{\delta_{max}^2}$, is evaluated. δ_{max}^2 is equal to the variance of the point data which is the original distribution. δ^2 is calculated for the upscaled model at the chosen grid block size. The criterion is considered as 2% that is when the variance of the upscaled model is about 2% of the variance of the point data. In that case, the continuous regime could dominate the transition regime and continuous length is evaluated. The percentage of blocks where there is some mixing, could also be considered as the criterion to evaluate the transition-continuous boundary. At the discrete-transition boundary, there is minimum mixing and at the transition-continuous boundary, there is very high percentage of mixing. The criteria are somewhat arbitrary and the thresholds could be pushed higher or lower for different applications.

Once again to apply this criterion, there is a need to define the dimensionless length scale to connect the geological feature size and the grid block size.

4.6 Dimensionless Length Scale Definition

A dimensionless length scale is defined as the maximum ratio of the length of the grid (sample volume) in each direction divided by the object size in that direction. In Figure 4.9, the object is 2D and non-isotropic.

$$\text{Dimensionless length scale} = \text{Max} (L_x/a_x , L_y/a_y)$$

“ a_x ” is the object length in X direction. “ L_x ” is the grid block size in X direction. In case of isotropic objects, a_x and a_y have the same size. For isotropic sample volumes L_x and L_y are equal as well. Figure 4.10 shows the models with isotropic and non-isotropic objects (geological features).

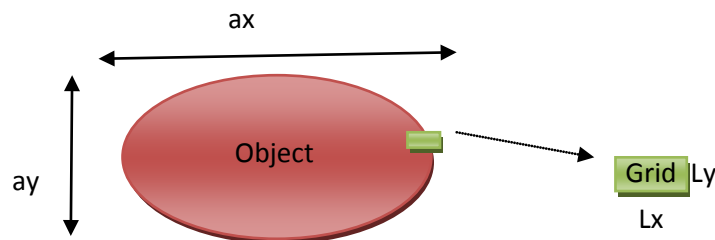


Figure 4.9: Object and sample volume to define dimensionless length scale

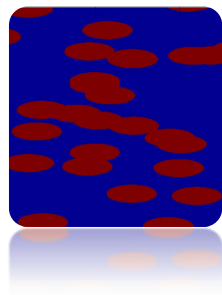
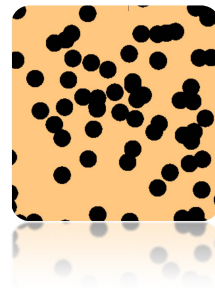


Figure 4.10: a) non isotropic objects



b) isotropic objects

The dimensionless length scale in 3D is taken as:

$$\text{Max} (L_x/a_x , L_y/a_y , L_z/a_z).$$

By applying the dimensionless scale, it does not matter if the objects in the model or the sample volumes are isotropic or not. In practice, it may be reasonable to keep the three different ratios because the grid size may be clearly large in one direction, but small in another – with respect to the size of the geological features.

4.7 General Review on Geological Models Put to Test

Three synthetic geological models are generated by the object based modeling technique. As mentioned before, we try to evaluate the regimes and the boundary of the transition regime quantitatively on each case based on the defined criteria in the previous sections. Models are all two dimensional that is the number of grids in Z direction is considered as 1 ($n_z = 1$). Figure 4.11a shows the pixel plot of the models that are put to test and explained one by one in detail in the next sections.

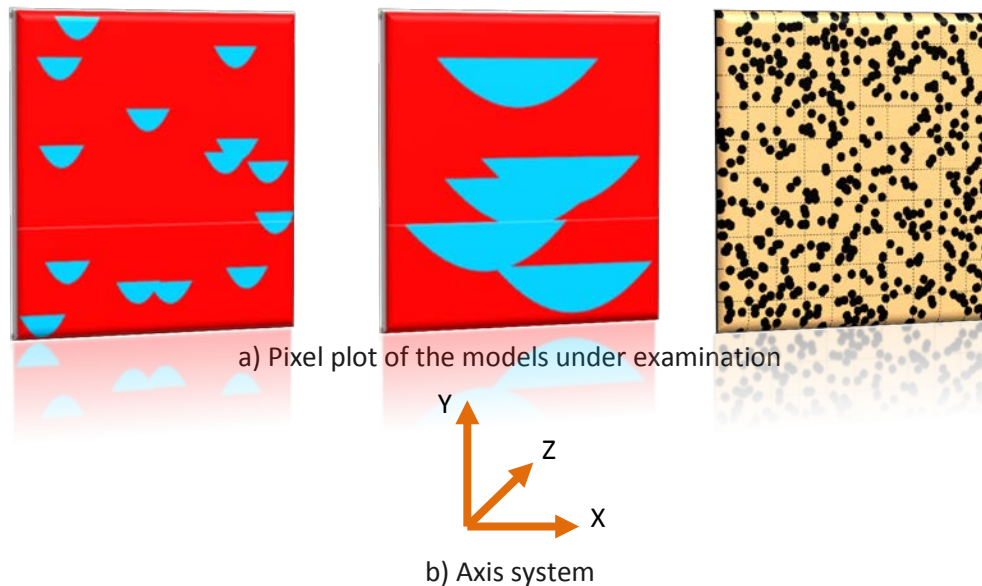


Figure 4.11: Images of the models under test with no scale

In the first and second models that are the small ones with less grids, objects are non-isotropic and channel shaped and in the third model (the big one), objects are isotropic circular objects. The axes system is shown in Figure 4.11b.

4.8 Evaluation of the Regime Boundaries on Small Models with Non Isotropic Objects

A program has been written in MATLAB to generate 2D object based models; 512 grid blocks in each direction were considered. The ELLIPSIM program from GSLIB was also considered to generate larger models. The objects are distributed randomly in the

models and are also low permeable parts of the models that cover 30% of the entire domain in both small models. Subsequently, permeability is assigned to the grids; 1 mD for low permeability objects and 1000 mD for high permeability grids. Histograms of small models are shown in

Figure 4.12 4.12. Y-axis is the frequency of the grid cells and X-axis is the permeability values (millidarcy). Afterwards, boundaries A and B of the transition regime are evaluated for the small models.

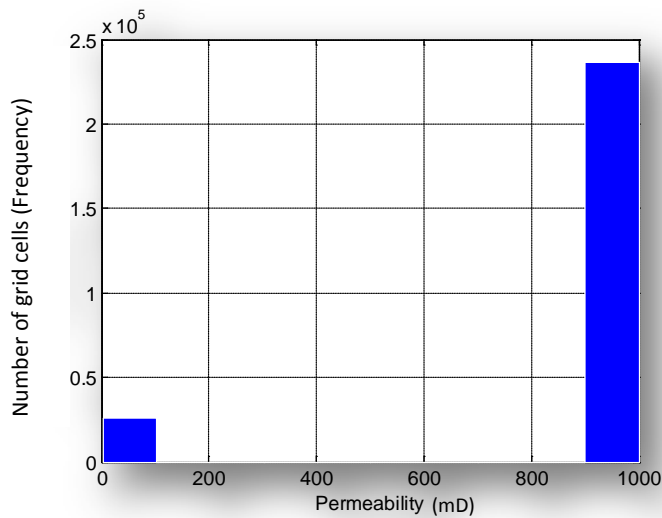


Figure 4.12: Histogram of the point data: 30% low permeability grids and 70% high permeability grids

Object size versus model size is presented in Figure 4.13. The objects are non-isotropic and 9 isotropic sample volumes are considered for scale up. The isotropic sample volumes are listed in Table 4.1. For example, for the model with 512 grid blocks in each direction, when sample volume is 8 by 8 by 1, the upscaled output model is a 64 by 64 by 1 model.

In the left model in Figure 4.13, the object size is about 1/6 times the domain size and relatively small compared to the domain size. In the right model the object size which is about half of the domain is considered big relative to the size of the domain. It could be interesting to examine these two different cases to get a better estimation of the grid

sizes at different regimes. We are interested to connect the size of the grids to the size of the geological feature.

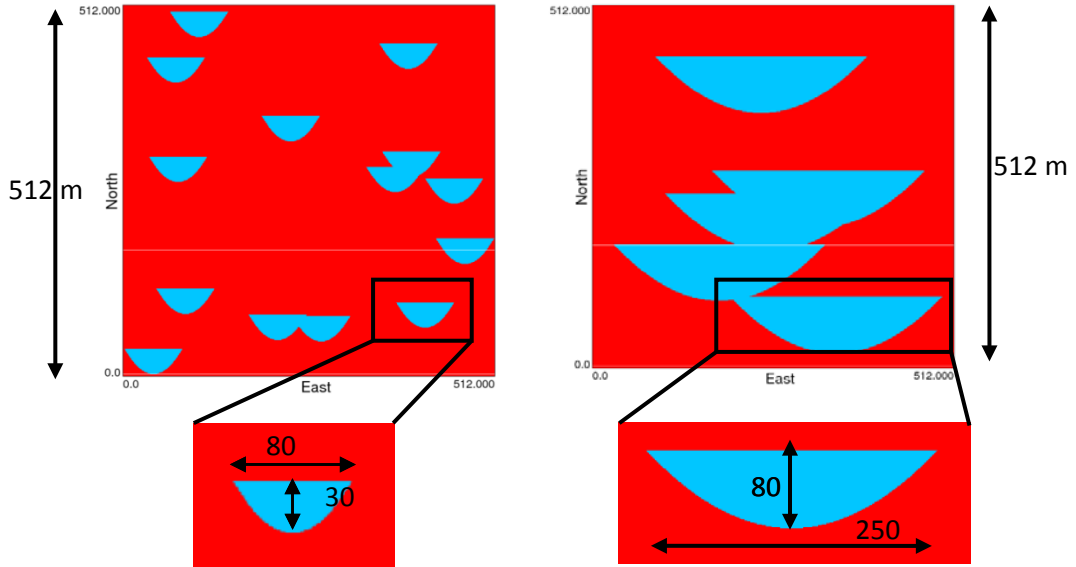


Figure 4.13: Objects scales versus whole models scales (all in meter)

Table 4.1: Sample Volumes and Output Model Size Applicable for Small Models

Scale ID	Isotropic Sample Volumes (m × m)	Output Model Size (# of cells)
1	2 × 2	256 × 256
2	4 × 4	128 × 128
3	8 × 8	64 × 64
4	16 × 16	32 × 32
5	32 × 32	16 × 16
6	64 × 64	8 × 8
7	128 × 128	4 × 4
8	256 × 256	2 × 2
9	512 × 512	1 × 1

4.8.1 Boundary A: Evaluating the Discrete Length for Small models

The mixing percentage is investigated by plotting the proportion of the mixed permeabilities when upscaling to a particular scale. Given that the criterion is

constituted of 15% mixing, Figure 4.14 shows the mixing proportion plots for both small models. Y-axis, that is proportion, is calculated as the proportion of the permeability values obtained by averaging and is not equal to the original permeability values. $\pm 5\%$ tolerance from the original values helps us to pick the mixed values. Each mixing percentage is calculated at a special sample volume size and X-axis is the corresponding scale ID, Table 4.1.

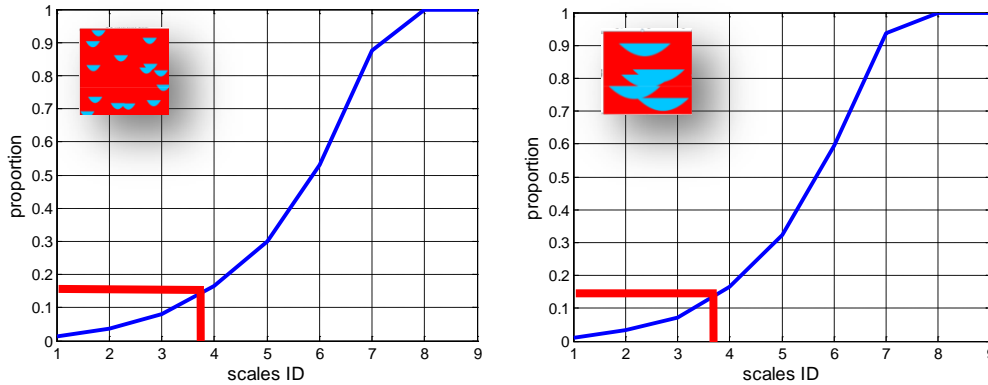


Figure 4.14: Proportion plots: First criteria for small models

Looking at Figure 4.14, the criteria is satisfied at scales somewhere between 3 and 4 for both models. Referring back to Table 4.1, scale ID 3 and 4 are equivalent to 8 and 16 grid block sizes respectively. Recall that the dimensionless scale is calculated by the division of the grid block size by object size. The dimensionless length scale in X and Y directions are shown by DL_x and DL_y respectively. Objects are non-isotropic while sample volumes are isotropic, that is grid size in X and Y directions have the same size. Grid block sizes, object sizes and dimensionless scales are listed in Table 4.2. Based on the criterion that we have defined, 15% mixing occurs when grid block size is between 0.27 to 0.53 of the object size for the first case and has a value between 0.1 to 0.2 for the second model. This means that when the grid block size is about 0.15 (between 0.1 and 0.2) of the object size for the second case, mixing is significant and the transition regime will be the dominant regime where the discrete regime ends. Table 4.3 shows the estimated discrete lengths for small models.

Table 4.2: Dimensionless Length Scales for the Lower Boundary of the Transition Regime

	Grid block size (m)	Object size in X direction (m)	DLx = Grid block size_x / object size_x	Object size in Y direction (m)	DLy = Grid block size_x / object size_x
1 st model	8	80	0.1	30	0.27
	16	80	0.2	30	0.53
2 nd model	8	250	0.032	80	0.1
	16	250	0.064	80	0.2

Table 4.3: Estimated Discrete Length

Discrete Length Approximation	
 1st small model	0.1-0.53 times object size
 2nd small model	0.032-0.2 times object size

4.8.2 Boundary B: Evaluating the Continuous Length for Small Models

To evaluate the upper boundary of the transition regime, the variance ratio is assessed and plotted for both small cases, Figure 4.15. The criterion is satisfied when the variance of the up-scaled model is about 2% of the variance of the point data that is the maximum variance.

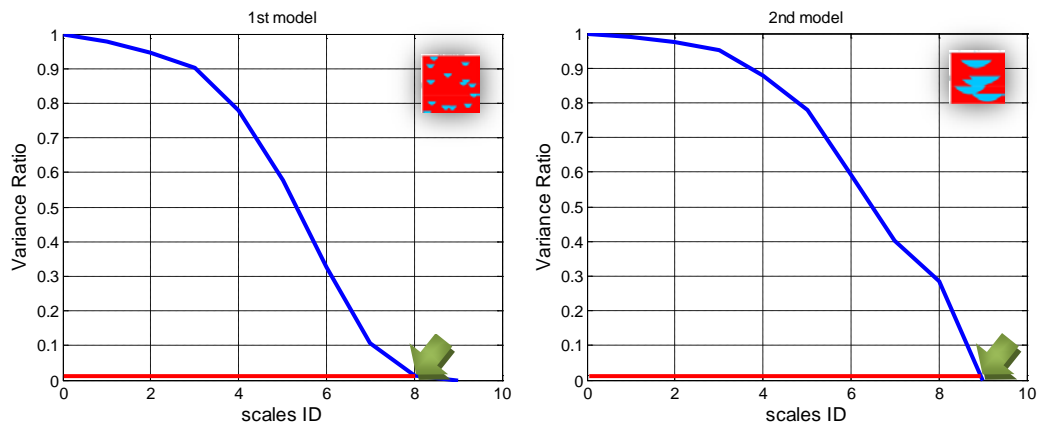




Figure 4.15: Variance ratio: Boundary B criterion for small models

Looking at Figure 4.15, 2% is satisfied at scale ID 8 for the first case and scale ID 9 for the second case that correspond to 256 and 512 grid block sizes respectively. Based on the object sizes and grid block sizes, dimensionless length scale at corresponding scales, where the criterion is satisfied, are presented in Table 4.4. Table 4.5 shows continuous length for both models.

Table 4.4: Dimensionless Length Scales for the Upper Boundary of the Transition

Regime					
	Grid block size (m)	Object size in x direction (m)	DLx	Object size in Y direction (m)	DLy
1 st model	256	80	3.2	30	8.53
2 nd model	512	250	2.05	80	6.4

Table 4.5: Estimated Continuous Lengths

		Continuous Length Approximation
	1st small model	3.2-8.53 times object size
	2nd small model	2.05-6.4 times object size

This means that for the first small model when the size of the grid is about 3 times bigger than the size of the object, the continuous regime starts. For the second case, the continuous regime happens at a grid size about 2 times bigger than the size of the geological feature in that model. The criteria are somewhat arbitrary and the thresholds could be pushed higher or lower for different applications.

4.8.3 Locating the Boundaries A and B on the REV Plots

Point data and all upscaled values at related grid sizes are plotted in one graph that we call it the REV plot in this work as it relates to the classic REV notion. The upscaled values are calculated by applying the FLOWSIM program. Now, we know the values of the grid sizes relative to the object size, for the lower and upper boundaries of the transition regime. In Figure 4.16 and Figure 4.17 that are REV plots in X and Y directions, the Y-axis of the plots is the effective permeability value and X-axis is the grid size. Plots are generated in both X and Y directions since effective values are different in X and Y

directions. As expected, the effective values converge to similar values in both directions because the model is randomly generated. For the first case, the grid size at the discrete regime is somewhere between 8 to 16m and for the upper boundary is about half of the domain that is about 256m. So, when the grid size is about half of the domain, geological features have to be presented continuously. Based on the analysis for the lower and upper boundaries of the transition regime, for the small model with bigger geological features (bigger objects), to present the discrete length, a grid size approximately equal to 16m is selected and for the continuous length, a grid size approximately equal to the length of the whole domain is the choice. The object size is large relative to the size of the domain and it shows that the representative elementary volume, in which the features are presented and modeled continuously, is close to the size of the domain for the case which even makes sense visually. Accordingly, there is a relation between the size of the grid and the size of the geological feature at different regimes.

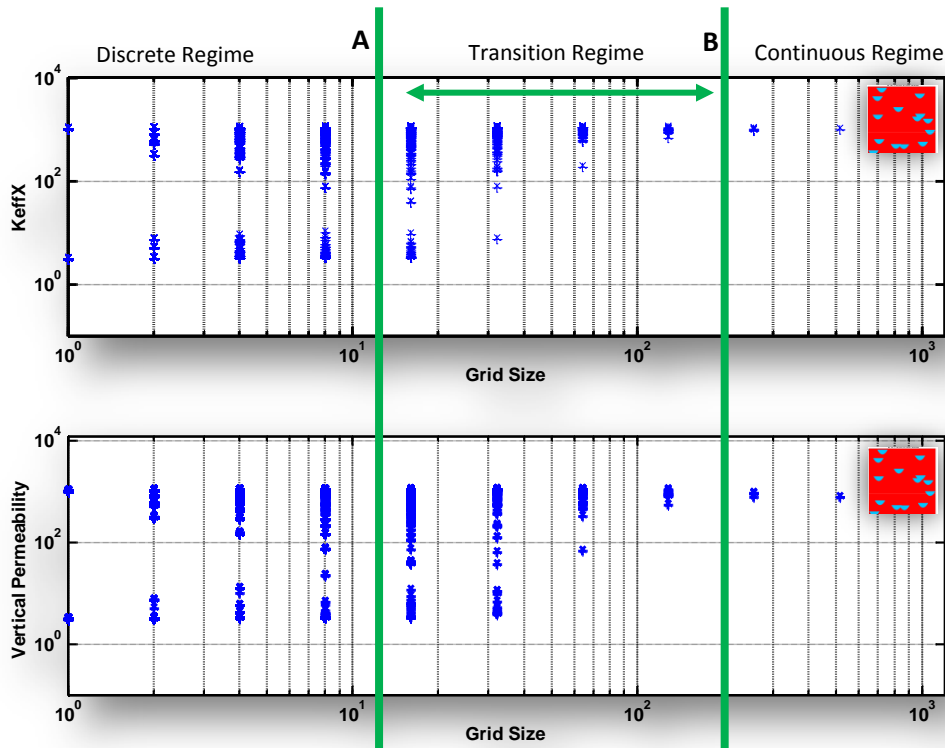


Figure 4.16: REV plots for the first model in X and Y directions (Small model with small objects), K_{effX} (mD) and K_{effY} (mD) vs. Grid size (m)

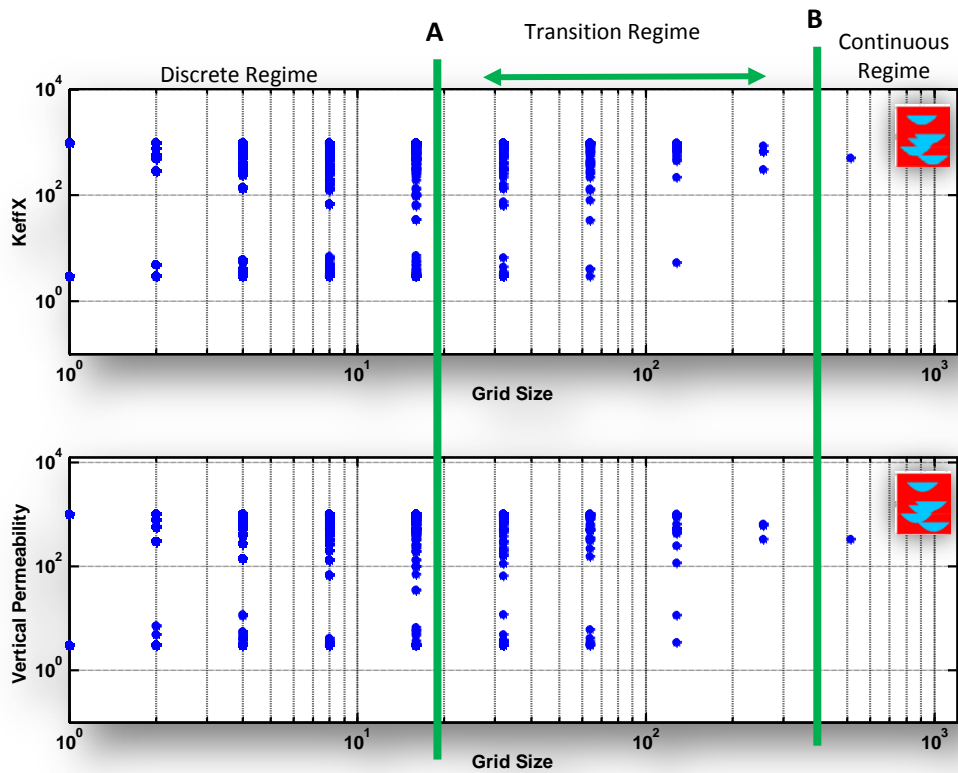
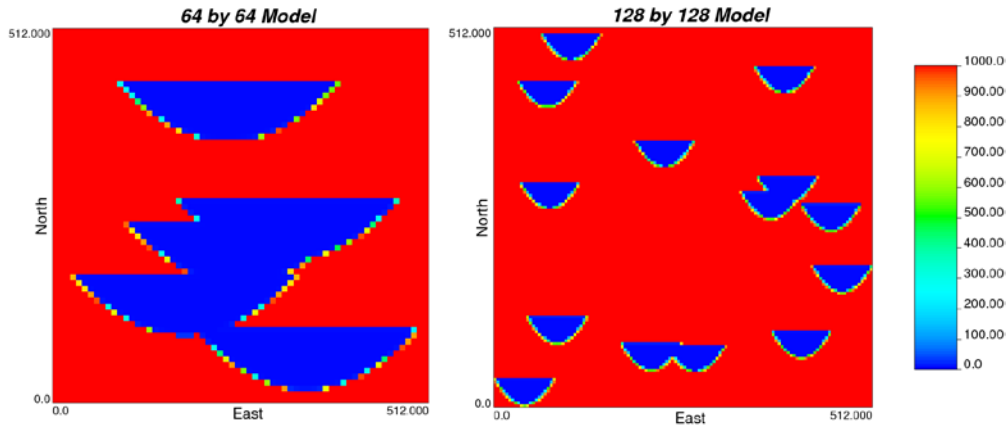


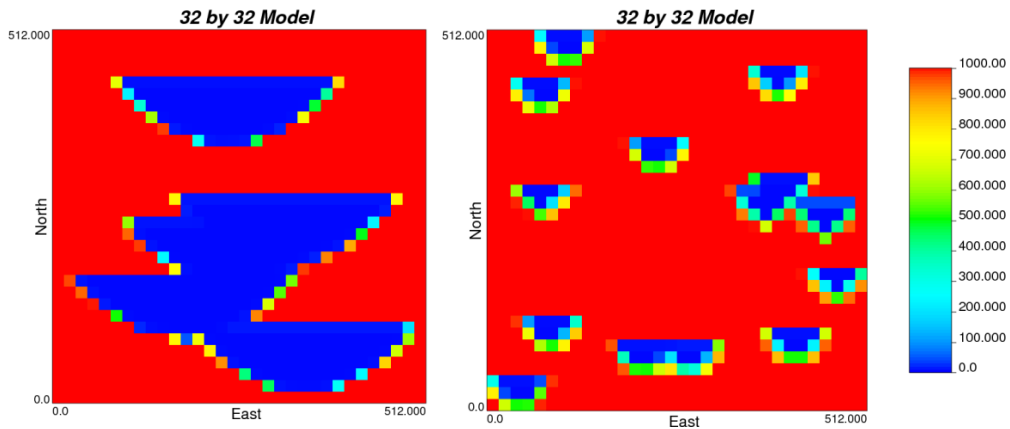
Figure 4.17: REV plots for the small model with bigger objects in X and Y directions
 K_{effX} (mD) and K_{effY} (mD) vs. Grid size (m)

Comparing Figures 4.16 and 4.17, discrete regime covers bigger area on the REV plot for the model with bigger objects.

Plots of the upscaled models are shown in Figure 4.18 in discrete and transition regimes. The transition regime starts at a smaller grid block size for the case with smaller geological objects since more mixing is observed at the same grid block size for the case with smaller objects compared to the one with bigger object size. Figure 4.18b shows the upscaled models at the identical grid size for both small models showing more mixing for the model with smaller objects. The model with big channels is still in the discrete regime and the model with the small channels is in the transition regime.



a) Upscaled models at discrete regime showing the edge effect



b) Upscaled models at grid block size 16m, LHS: in discrete regime
RHS: in transition regime

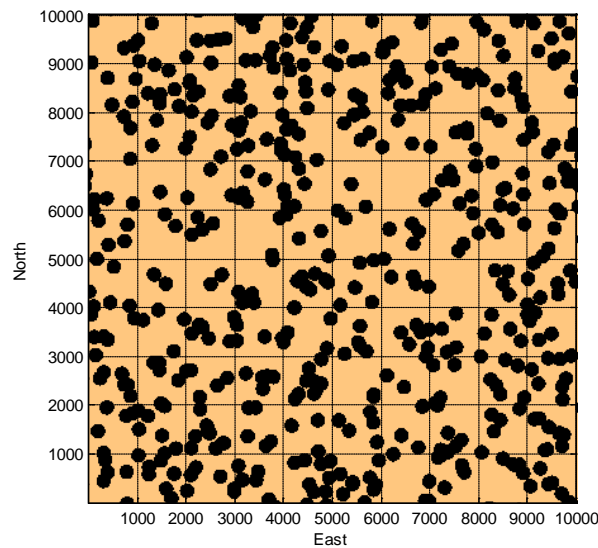
Figure 4.18: Plot of upscaled models at discrete and transition regimes

To propose the final modified REV plot and to have another evaluation of the boundaries of the transition regime, the previous workflow is conducted on a very large model with 100 million grid cells and isotropic circular geological objects.

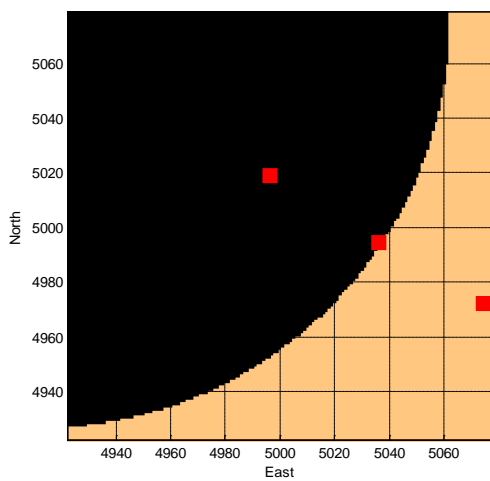
4.9 Definition of the Transition Regime on a Large Model

To analyze the REV plot for scales less than the size of the object and also bigger than the size of the object, a model with the largest possible size is preferable. It helps to evaluate the boundaries of the transition regime more realistically. For this purpose, a binary 2D model is generated by the ELLIPSIM program of GSLIB considering 100 million

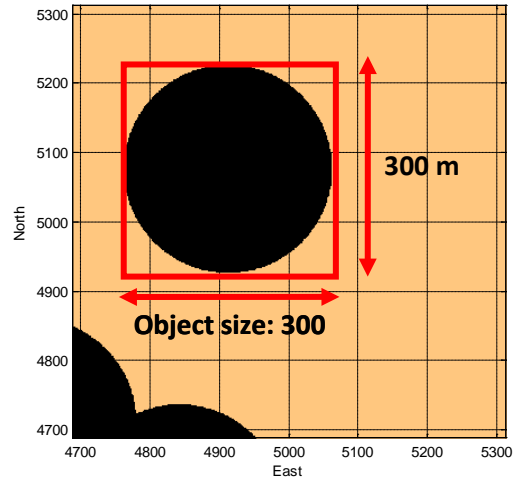
grid cells, a $10000 \times 10000 \times 1$ model with 30% low permeability objects and 70% sand. Objects are isotropic, randomly distributed in the domain and 300 grids discretize the length of the objects in X and Y directions. It's interesting to see and analyze upscaling results when the sample volume size is about 1/100 of the object size, that is, a sample volume size equal to $3\text{m} \times 3\text{m} \times 1\text{m}$. The size of the domain is 30 times bigger than the size of the object. In this model, both the object(s) and sample volume(s) are isotropic. The model is visualized in MATLAB (IMAGESC), Figure 4.19. Figure 4.19b shows a grid size about 1/100 of the object size; the geological feature is presented discretely at this scale.



a) Whole domain (10000m by 10000m)



b) Grid size = 1/100 of the object size



c) Grid size is equal to the object size

Figure 4.19: Large model with isotropic objects at 3 scales

There is always some grid resolution concerns. At scales less than the size of the object, say 1/100 of the object scale, it has a discrete nature of the object as the grid is small relative to the object size (Figure 4.19b) and the geological feature is presented discretely. To evaluate the boundary of the transition regime, the similar experiments applied on the small models in the previous sections, are conducted here as well.

Due to computational cost and memory limitations, only one realization of the model is generated. Subsequent to the construction of the object based model, permeabilities are assigned to the output of the ELLIPSIM program, 1mD for the objects' permeability and 1000mD for the background grid cells (sand). As the model is large, the arithmetic and geometric averages are analysed as upscaled values rather than applying flow based upscaling results.

The FLOWSIM program is modified to perform only arithmetic/geometric averaging over 100 million grid cells and at lower scales. The X-axis shows the dimensionless length scale and the Y-axis is the upscaled values. On the X-axis, 1 represents the size of the object on the REV plots. The difference before and after 1 on the REV plot is considerable. 24 possible isotropic sample volume sizes are considered for scaling up the model, see Table 4.6.

Table 4.6: Sample Volumes and Resulted Output Model Size

Sample Volume Size (m × m × m)	Output Model Size (# of grid cells)
10000 × 10000 × 1	1 × 1 × 1
5000 × 5000 × 1	2 × 2 × 1
2500 × 2500 × 1	4 × 4 × 1
1250 × 1250 × 1	8 × 8 × 1
625 × 625 × 1	16 × 16 × 1
125 × 125 × 1	80 × 80 × 1
25 × 25 × 1	400 × 400 × 1
5 × 5 × 1	2000 × 2000 × 1
1 × 1 × 1	10000 × 10000 × 1
2 × 2 × 1	5000 × 5000 × 1
4 × 4 × 1	2500 × 2500 × 1

$8 \times 8 \times 1$	$1250 \times 1250 \times 1$
$16 \times 16 \times 1$	$625 \times 625 \times 1$
$80 \times 80 \times 1$	$125 \times 125 \times 1$
$400 \times 400 \times 1$	$25 \times 25 \times 1$
$2000 \times 2000 \times 1$	$5 \times 5 \times 1$
$500 \times 500 \times 1$	$20 \times 20 \times 1$
$20 \times 20 \times 1$	$500 \times 500 \times 1$
$100 \times 100 \times 1$	$10 \times 10 \times 1$
$250 \times 250 \times 1$	$40 \times 40 \times 1$
$10 \times 10 \times 1$	$100 \times 100 \times 1$
$50 \times 50 \times 1$	$200 \times 200 \times 1$
$10 \times 10 \times 1$	$1000 \times 1000 \times 1$
$80 \times 80 \times 1$	$125 \times 125 \times 1$
$40 \times 40 \times 1$	$250 \times 250 \times 1$

4.9.1. Boundary A: Evaluating the Discrete Length for Large Model

During upscaling and the consequent mixing, the increasing proportion of the upscaled values in between the original extreme values of the data helps understand the correct regime. Proportion plots are presented as the ratio of the numbers of mixed values over the original data with $\pm 5\%$ tolerance at each scale, see Figure 4.20. The Y-axis is the proportion values obtained by the arithmetic averaging. The X-axis is the calculated dimensionless length scale. Table 4.7 shows the discrete length obtained by both geometric and arithmetic averaging. AA and GA stand for arithmetic and geometric averaging, respectively. The criterion is applied on both arithmetic and geometric averaged results. The results are similar; therefore the plots for arithmetic averaging are shown in subsequent sections.

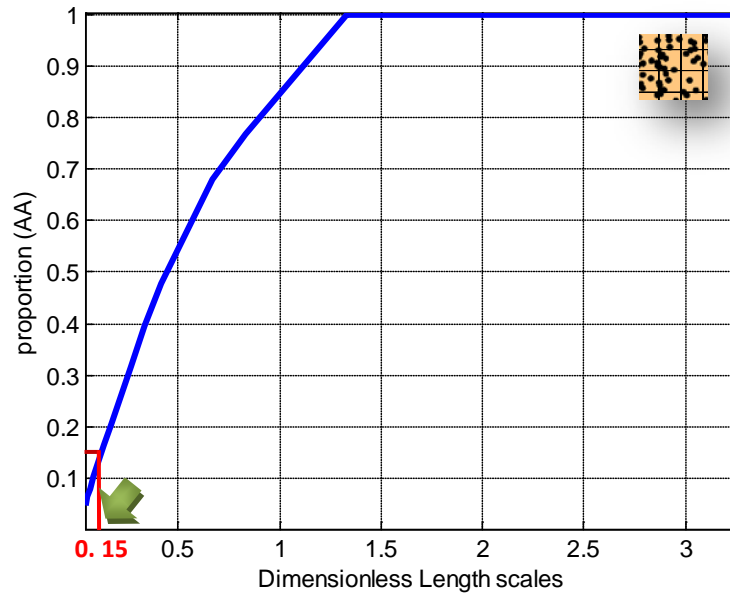


Figure 4.20: Proportion plot for arithmetic averaging

Table 4.7: Estimated Discrete Length for Large Model

		Discrete Length Approximation
	Large model (AA)	0.15 of object size
	Large model (GA)	0.17 of object size

Based on the proportion plot, where the size of the grid blocks is less than 0.15 of the geological feature, the criterion for boundary A is satisfied and the feature is represented discretely where mixing is not significant.

Selecting the criterion is not precise, but a reasonable value should be chosen. The criterion could be defined as a range as well. For example, a range of 0.1%-0.2% for the lower boundary looks reasonable. 15% mixing is at the middle of the range.

4.9.2. Boundary B: Evaluating the Continuous Length for the Large Model

Evaluation of the variance ratio helps assess the upper boundary. Consideration of larger grid cells will appear to reduce the variance. The criterion is defined as the variance of the upscaled model over the maximum variance that is the variance of the

original high-resolution model. Figure 4.21 shows the variance ratio for the upscaled values versus dimensionless length scale.

The variance ratio threshold was set at 2%. For the current model under investigation, the criterion is satisfied where the size of the grid blocks is somewhere close to 6 times the feature size. Table 4.8 shows the continuous length given by arithmetic and geometric averaging. This criterion could be defined as a range. For example, a variance ratio within the range 1% - 3% would be reasonable. The green lines on Figure 4.21 show the satisfied criterion within the range.

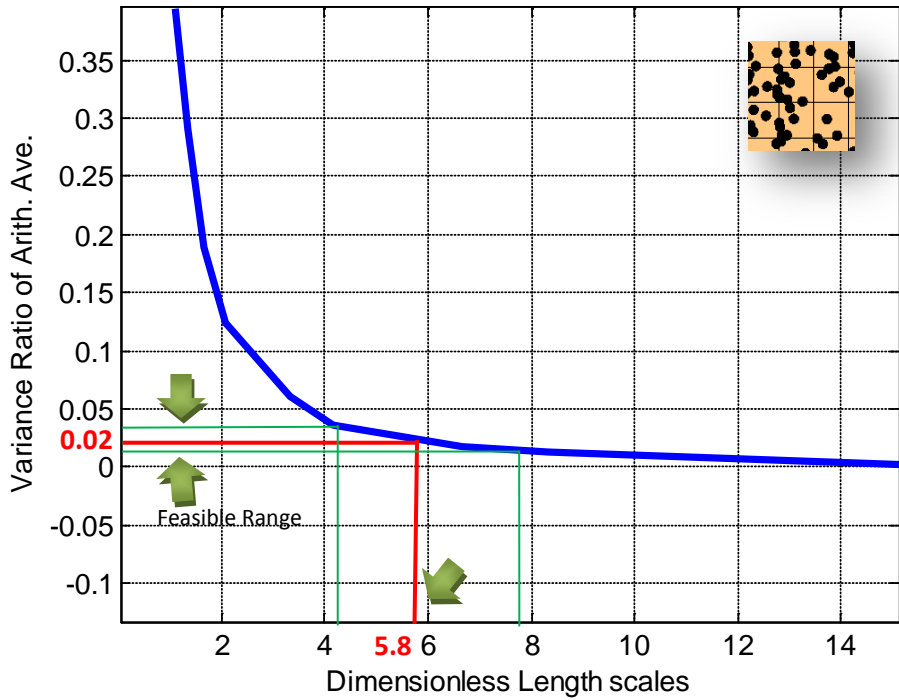
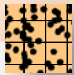


Figure 4.21: Variance ratio plot for AA results

Table 4.8: Estimated Continuous Length for the Large Model

		Continuous Length Approximation
	Large model (AA)	About 5.8 times object size
	Large model (GA)	About 6.3 times object size

4.9.3. Locating the Boundaries A and B on the REV Plot

The REV plot is presented for the arithmetic averaged values in Figure 4.22. There is about 150 million data presented on the graph. Based on the defined criteria, A and B boundaries are put on the REV plot. The grid size of $4 \times 4 \times 1$ is the threshold for the discrete regime that results in a $250 \times 250 \times 1$ model and it shows the mixing at the early stage, see Figure 4.23.

Figure 4.24 shows two models at different scales but in the transition regime. Obviously, there is more mixing for the $80 \times 80 \times 1$ model rather than the $100 \times 100 \times 1$ model since the grid size is larger in the former model. Many upscaling calculations have been conducted to help us evaluate the transition regime with respect to the geological feature size and the grid size. Among those, the results for three models are selected to be presented in this chapter.

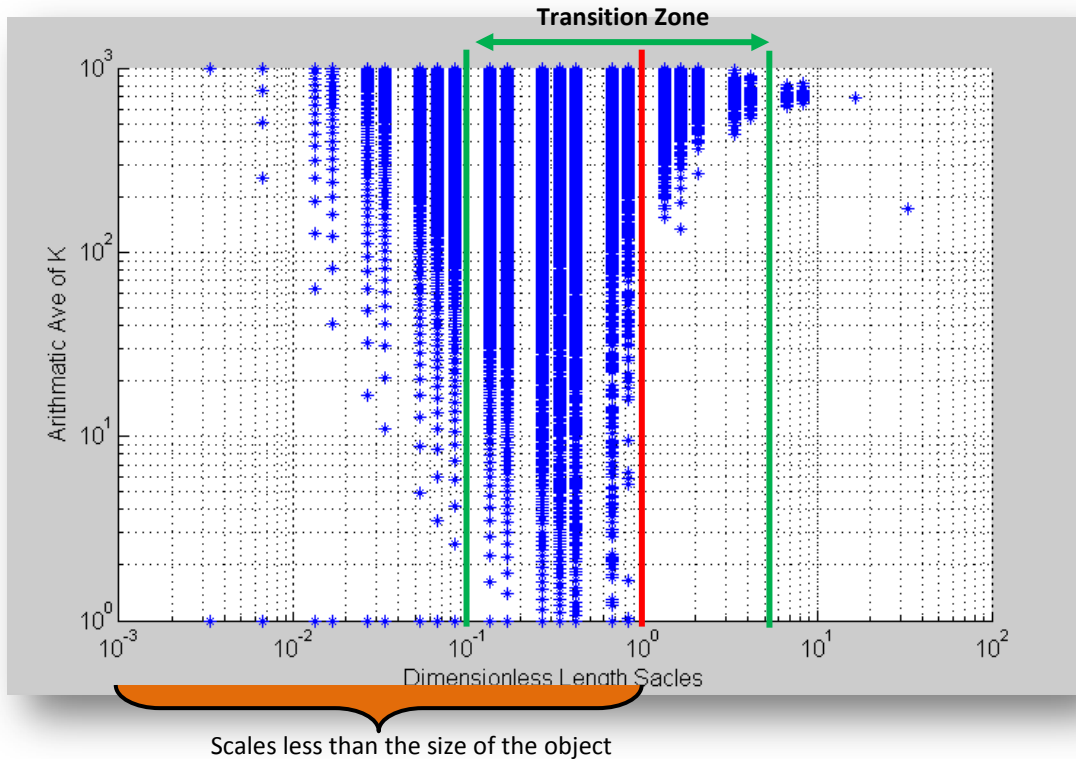


Figure 4.22: REV plot for the big model including ~150 million data (Keff (mD) vs. Dimensionless length scale)

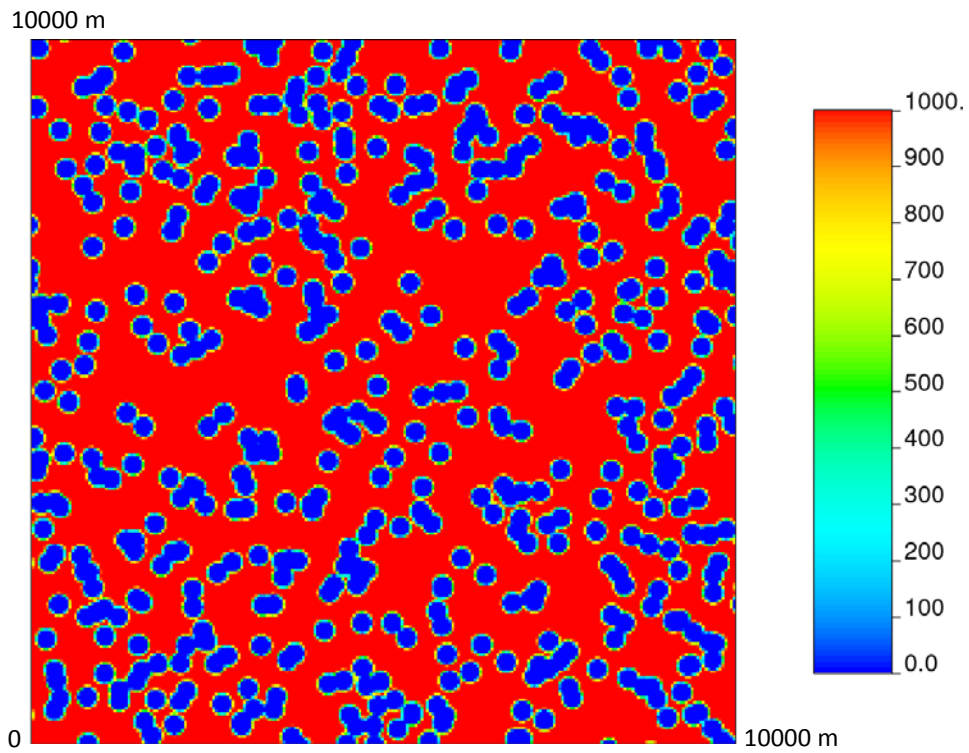
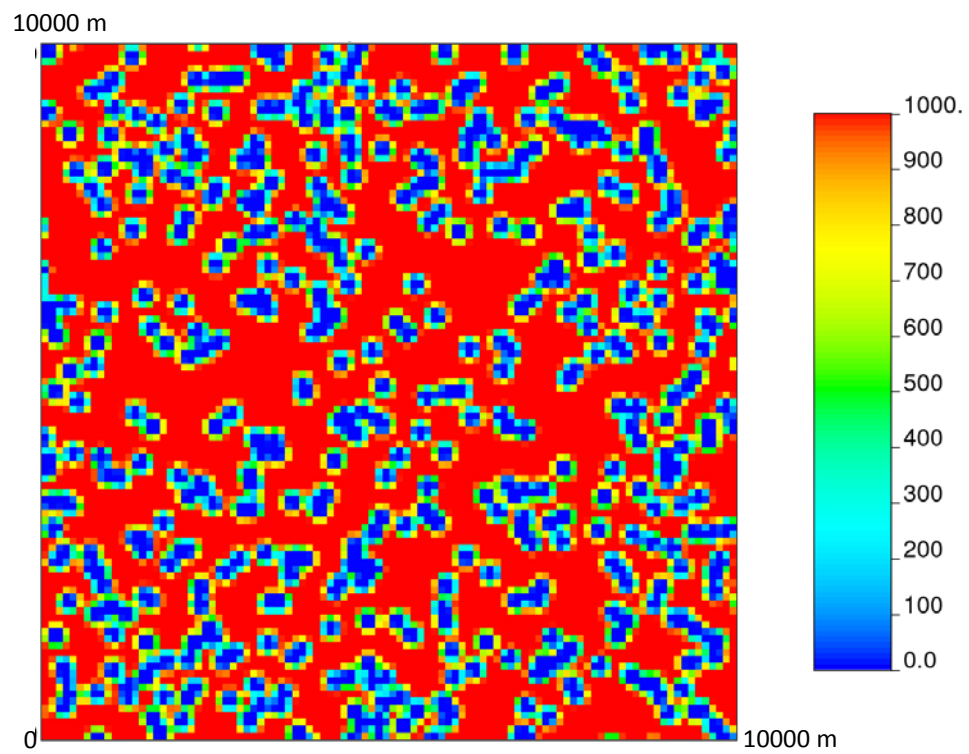


Figure 4.23: Model in the discrete regime showing edge effect, $250 \times 250 \times 1$ model

(Grid size: $4\text{m} \times 4\text{m} \times 1\text{m}$)



a) $100 \times 100 \times 1$ Model in transition, grid size: $100\text{m} \times 100\text{m} \times 1\text{m}$

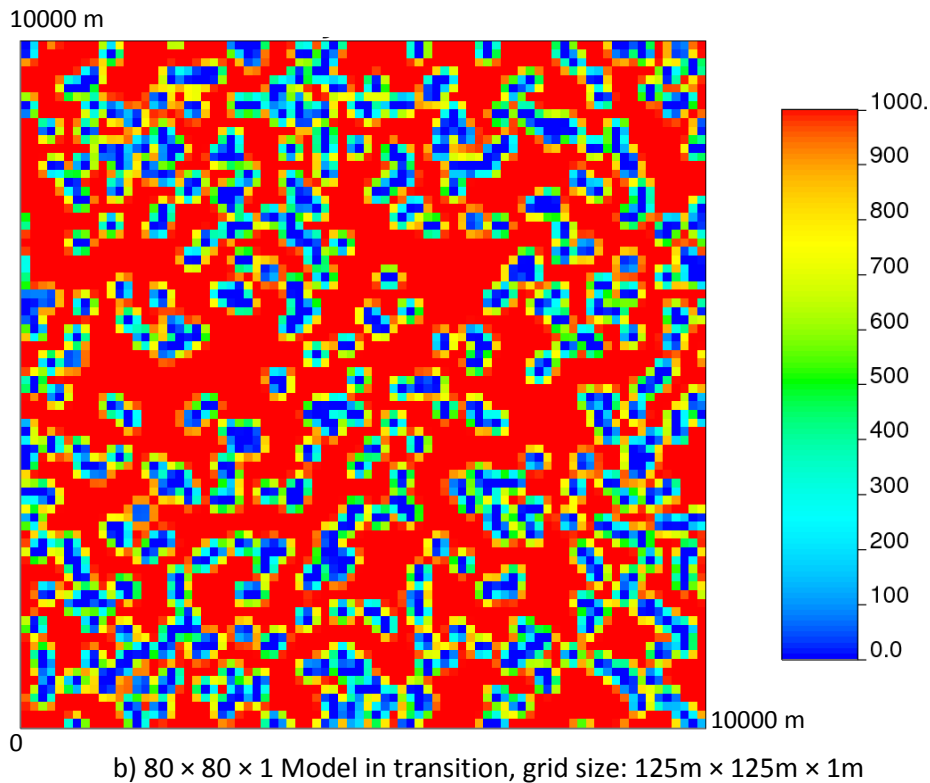


Figure 4.24: Models in the transition regime

4.10 Proposed Modified REV Plot

In the classic REV point of view, the focus has been mainly on the continuous regime, yet in this work, 3 regimes are defined. The following ranges for the lower and upper boundaries of the transition regime are summarized from the work presented above.

Table 4.9: General Range for Lower and Upper Boundaries of the Transition Regime

Grid size at Lower Boundary (A): 1/30 – 1/5 times the object size

Grid size at Upper Boundary (B): 2.5 – 7 times the object size

A threshold of 1/15 times the object size is selected for the lower boundary and 5 times the object size for the upper boundary. These thresholds help to show the proposed model for different geological systems, see Figure 4.25 for an example.

The modified REV plot is presented in the logarithmic scale. The Y-axis is the scale/size of the geological feature in meters and the X-axis is the grid size in meters. The values

found for the boundaries of the transition regime on the modified REV plot are the slopes of the two parallel blue lines on Figure 4.25.

For a fixed grid size, large features are represented discretely and small features are represented continuously and some features are in transition from discrete to continuous.

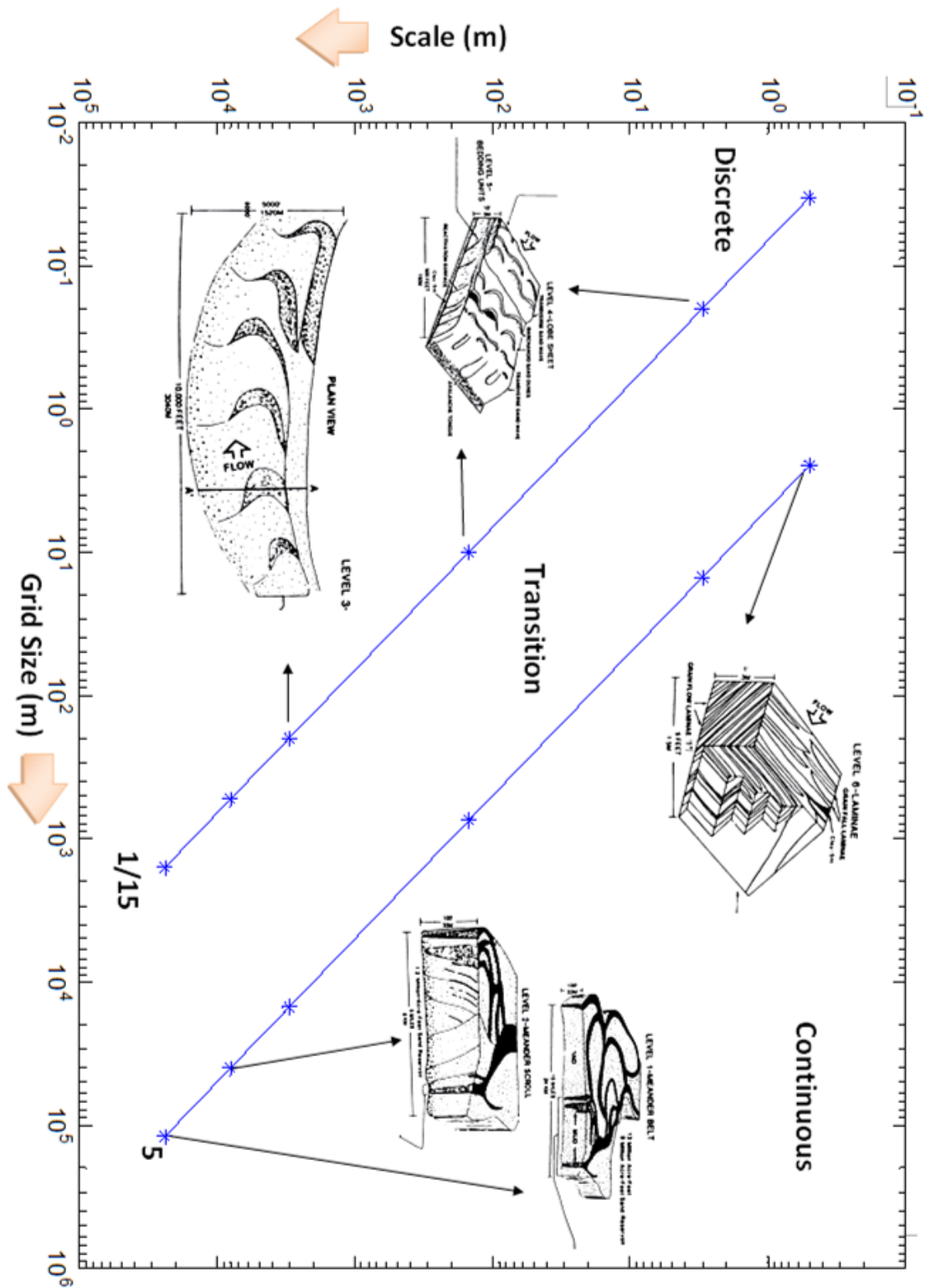
The next goal is to choose the proper modeling approach. When we are clearly in the discrete or continuous regime, we know what type of modeling approach must be used; however, the transition regime is a challenge. The variance is very high and the spatial dependence of the values is very important. This will be addressed in the next chapter.

4.11 Conclusion

This chapter developed the concept of heterogeneity being represented as discrete or continuous. There is a transition between discrete and continuous. This is linked to the notion of the representative elementary volume/REV. This leads to an extended view of the modeling regimes.

Finally, values between $1/30 - 1/5$ times the object size were established for the lower boundary of the transition regime and values between 2.5-7 times the object size were established for the upper boundary of the transition regime. In the end, the proposed modified REV plot was presented for a real petroleum system.

Figure 4.25: Proposed Modified REV Plot Considering the Levels of Reservoir Heterogeneity



- Reference for the reservoir heterogeneity images: Miall, A.D., 1996, "The Geology of Fluvial Deposits", Springer.

5 Practical Modeling Considerations for the Transition Regime

In the previous chapter, a modified REV plot is proposed that defines three regimes: discrete, transition and continuous. The objective of this chapter is to address the challenge of modeling in the transition regime when the size of the grid blocks is less than the REV scale and larger than the discrete scale.

5.1 Motivation

If geological features are represented discretely, discrete modeling techniques such as object based or indicator methods may be used. If they are represented continuously, continuous modeling approaches such as Gaussian approaches may be used. The transition regime is a challenge because there is significant variability between grid blocks and within grid blocks. There is a need to adopt a modeling approach for the transition zone that preserves these variabilities and creates models that lead to unbiased forecasts.

Considering a specific grid size and geological feature size, the feature could be partially or completely present in the grid. Moreover, there could be a variable number of features present in one grid cell, see Figure 5.1. The figure is a schematic illustration with no particular scale. The partially present case will likely have to be represented continuously rather than discretely, but acknowledging and accounting for the fact that it is still not at the REV scale and it is in the transition regime.



Figure 5.1: Feature is partially present, completely present and multiple present in the grids

A fixed grid size and variable feature sizes are considered in this chapter to establish some practical modeling methodologies in the transition regime. A mind-map for the approach is shown in Figure 5.2.

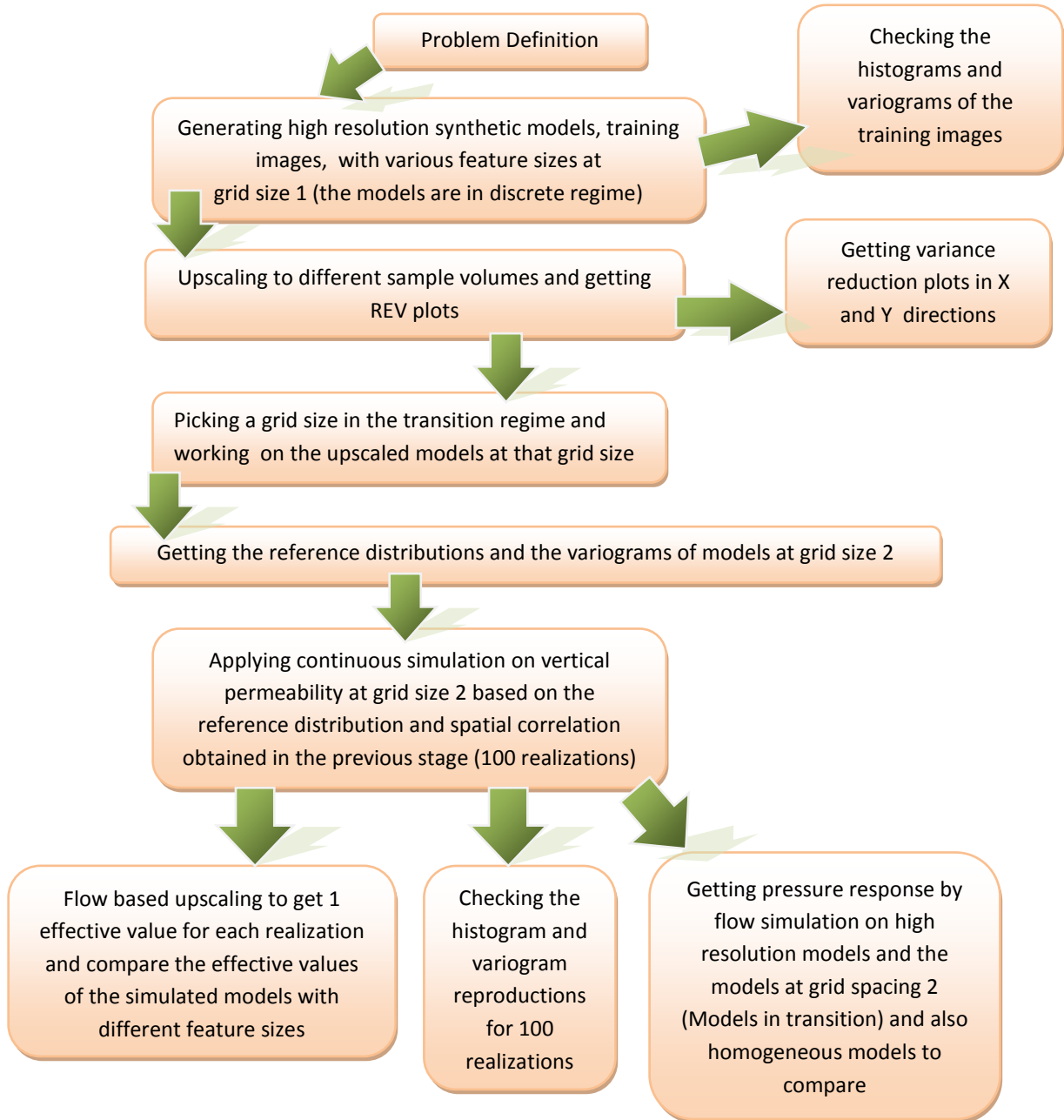


Figure 5.2: Mind-map for the practical modeling application at the transition regime

5.2 Problem Definition

For illustration, consider a 2D cross section of a schematic reservoir volume 512 meters high and 512 meters wide gridded by 1 meter by 1 meter grids, see Figure 5.3. The reservoir with the 512 by 512 grids is considered a high resolution or fine scale model, while there is a requirement to get a coarse model because of computational limitations for flow simulation purposes. Therefore, the fine model needs to be upscaled to the coarse model. A grid size in the transition regime will be selected to observe the practical implementation of modeling. The question is whether or not the heterogeneity is captured properly at the scale of coarse model.

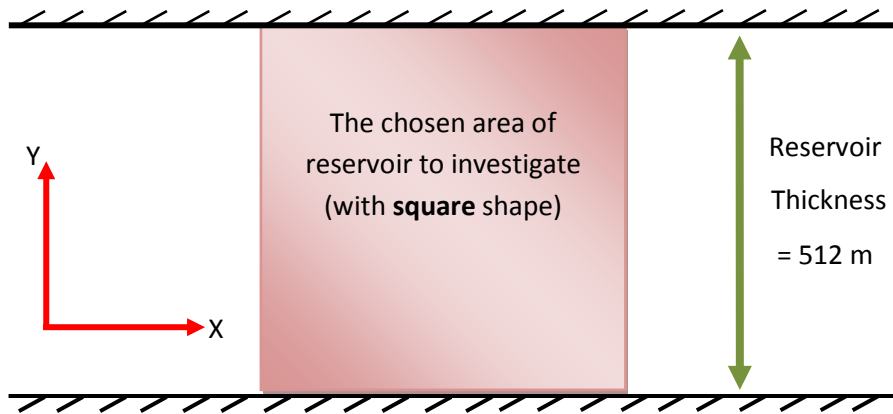


Figure 5.3: The shaded area will be replaced with different geological models

For this purpose, the high resolution model is replaced with a variety of geological models including various geological feature sizes that are shale breaks at different lengths. Some 2D training images are generated for this purpose. By considering the feature size and the selected grid size, modeling in the transition regime is investigated.

Also, the high resolution models and related coarse models are put under vertical and horizontal single phase flow flooding tests. The output is the pressure distribution on the fine and coarse grids. To compare, some homogenous geological models are generated and the horizontal and vertical flooding tests are also applied on them. The pressure distribution for fine models, coarse models and the homogeneous geological models is calculated. All cases are compared by plotting the scatter plots of pressure

distribution on fine and coarse grids and calculating the corresponding correlation coefficients. These tests are helpful to show how heterogeneity is captured by the coarse models.

In this chapter, the importance of selecting a proper grid block size is emphasized. The challenges of modeling in the transition regime are highlighted.

5.3 Generating Training Images (High Resolution Synthetic Models)

Synthetic reference models, the shaded square area in Figure 5.3, are simulated for testing. Various scenarios considering different shale breaks lengths are generated. The high resolution models, that are also called 2D training images, are generated by the ELLIPSIM program that is an object based GSLIB program. The low permeability grid cells or shales, are placed randomly in a high permeability matrix. The models are 512 by 512 square units and are discretized by 1 by 1 grid blocks. They all include 10% shale with different shale break lengths, see Figure 5.4. Three training images called A, B and C scenarios are generated with shale break lengths in the X-direction equal to 1/50, 1/10 and 1/2 of the domain size, respectively. The shale break size in the Y-direction is given as 2 units. The shale break sizes in X and Y-directions are tabulated in Table 5.1.

Table 5.1: Shale Breaks' Sizes in Training Images

Scenario	Size in X-direction (m)	Size in Y-direction (m)
A	512 / 50	2
B	512 / 10	2
C	512 / 2	2

Subsequently, permeability values are assigned to the grids; 1 mD for low permeability grids and 1000 mD for high permeability grids. The results for this model size are deemed representative of larger models.

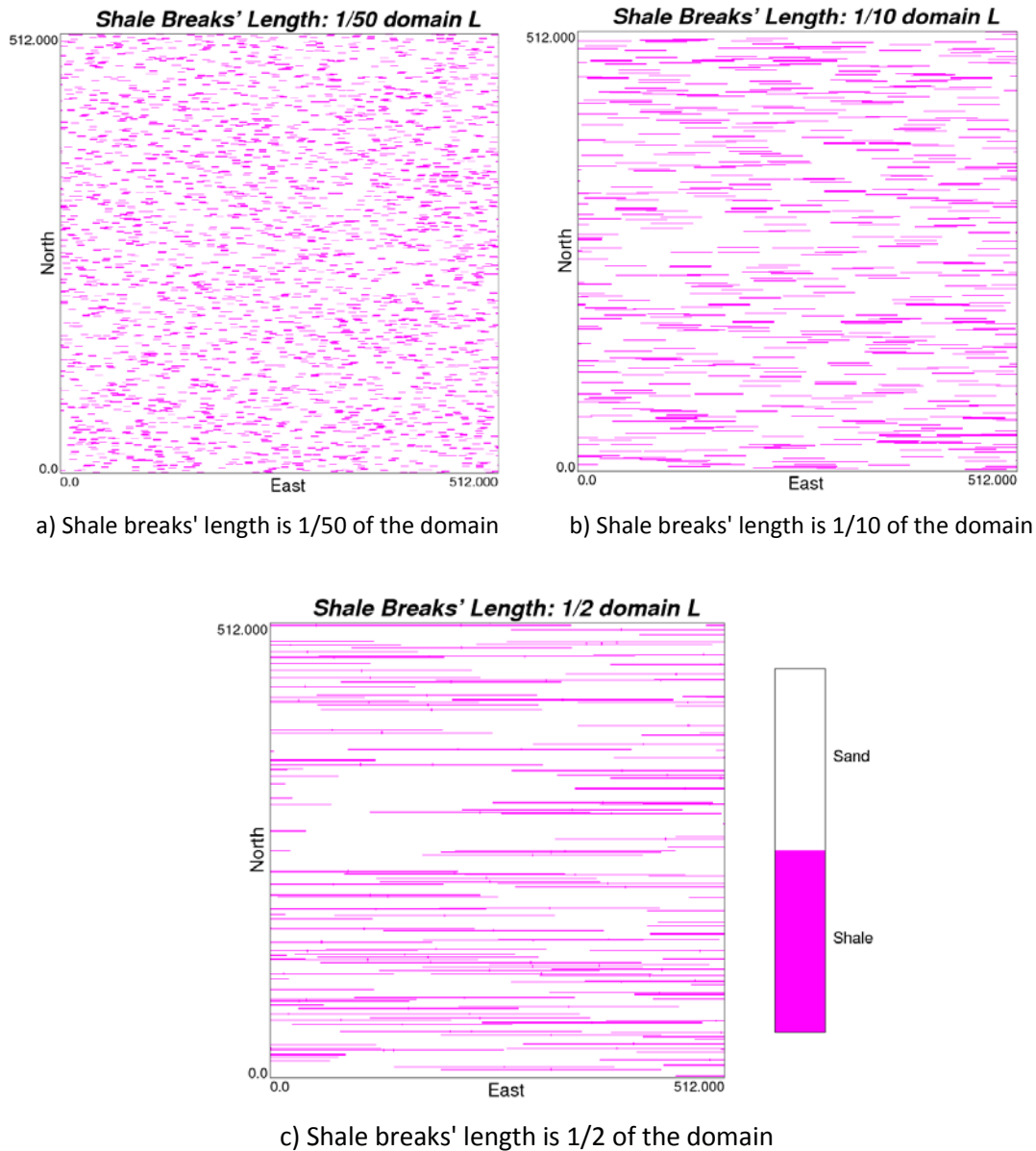


Figure 5.4: Geological synthetic models generated by ELLISPIM, scenarios A, B and C

5.4 Histograms and Variograms of Generated Training Images

The histograms and variograms of the generated training images are calculated and plotted. At the current grid block size which is 1, the histograms of the scenarios A, B and C in X and Y-directions are bimodal and exactly the same that is 10% low permeability grids and 90% high permeability grids, see Figure 5.5. The variograms,

however, of scenarios A, B and C in X and Y-directions are different. They are pure nugget effects in Y-direction, see Figure 5.6. The variograms in the X-direction, however, show structures depending on the size of the shale breaks.

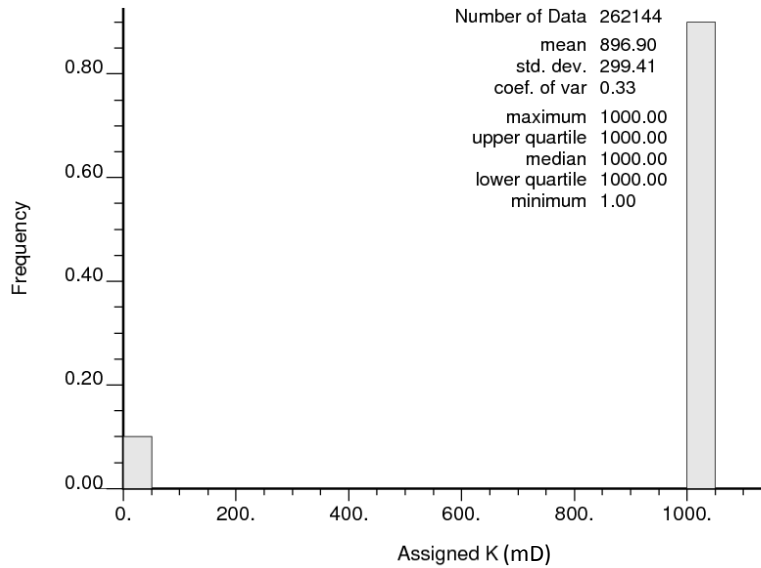
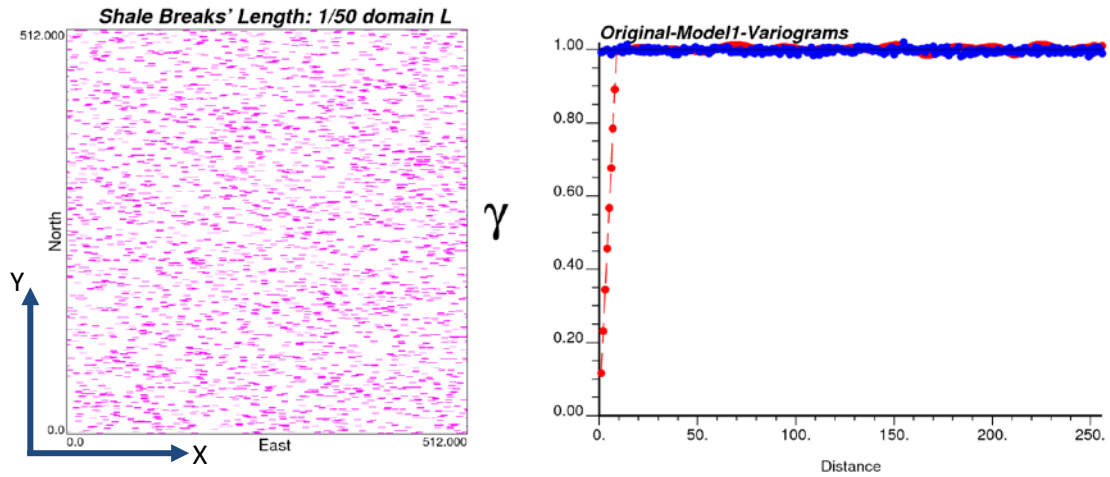
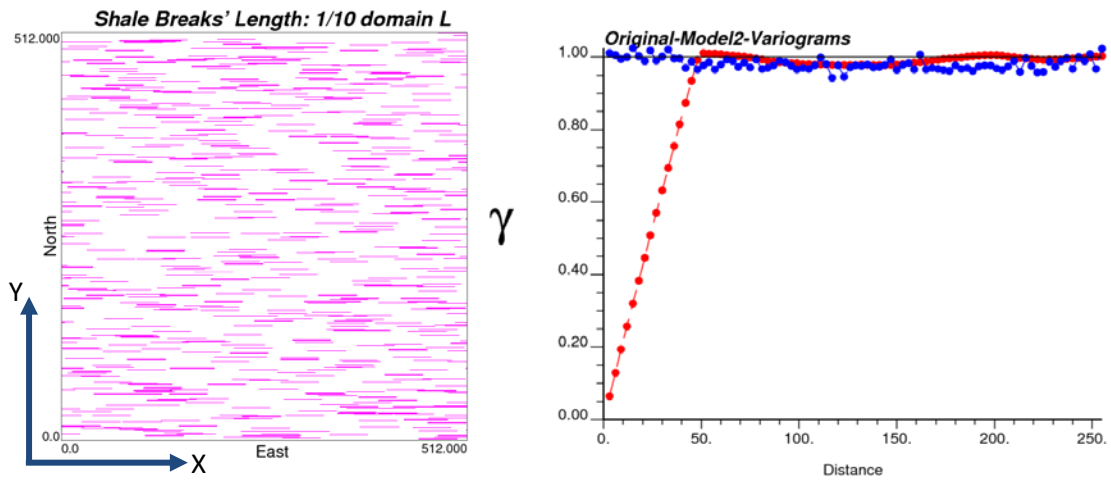


Figure 5.5: Histogram of training images, same for A, B and C scenarios

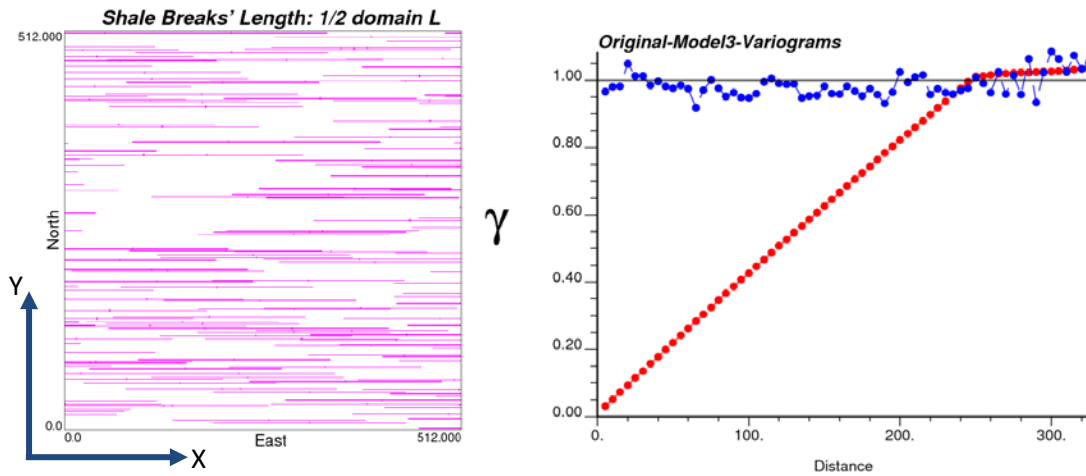
The variograms are plotted for about half of the domain size to compare scenarios A, B and C in X and Y-directions. Horizontal (X direction) and vertical (Y direction) variograms are in red and blue respectively. The variogram ranges of A, B and C scenarios in X-direction are about 10, 50 and 250 meters respectively that are equal to the feature sizes in X-direction, see Figure 5.6. The vertical variograms, that show the continuity in Y direction, are all pure nugget effect.



a) Variograms of scenario A



b) Variograms of scenario B



c) Variograms of scenario C

Figure 5.6: Variograms in X and Y-directions for scenarios A, B and C

5.5 REV Plots Applicable to Select a Grid Size in Transition Regime

In this section, the goal is to pick a grid size in the transition regime for all scenarios. Therefore, 9 isotropic sample volumes are considered to scale up scenarios A, B and C, see Table 5.2. The FLOWSIM program is applied to get the effective property values. The effective values versus the dimensionless length scale, which is defined in the previous chapter, are plotted for scenario A, see Figure 5.7.

Table 5.2: Isotropic Sample Volumes

Scale ID Number	Sample volume Grid Size (m × m)	Output Model Grid # in X and Y	Output Model Grid Size (m)
1	1 × 1	512 × 512	1
2	2 × 2	256 × 256	2
3	4 × 4	128 × 128	4
4	8 × 8	64 × 64	8
5	16 × 16	32 × 32	16
6	32 × 32	16 × 16	32
7	64 × 64	8 × 8	64
8	128 × 128	4 × 4	128
9	256 × 256	2 × 2	256
10	512 × 512	1 × 1	512

The REV plots corresponding to scenarios B and C, are very similar in the X and Y-directions to Figure 5.7. The effective values in X-direction converge to the arithmetic average for all scenarios. The effective values in Y-direction converge to the lower values for the cases with larger shale breaks' lengths, see Table 5.3. In Table 5.3, KeffH is called horizontal effective permeability that is calculated by simple arithmetic averaging between effective values in X and Y-directions shown by KeffX and KeffY. The KA, KG and KH are arithmetic, geometric and harmonic averages, respectively.

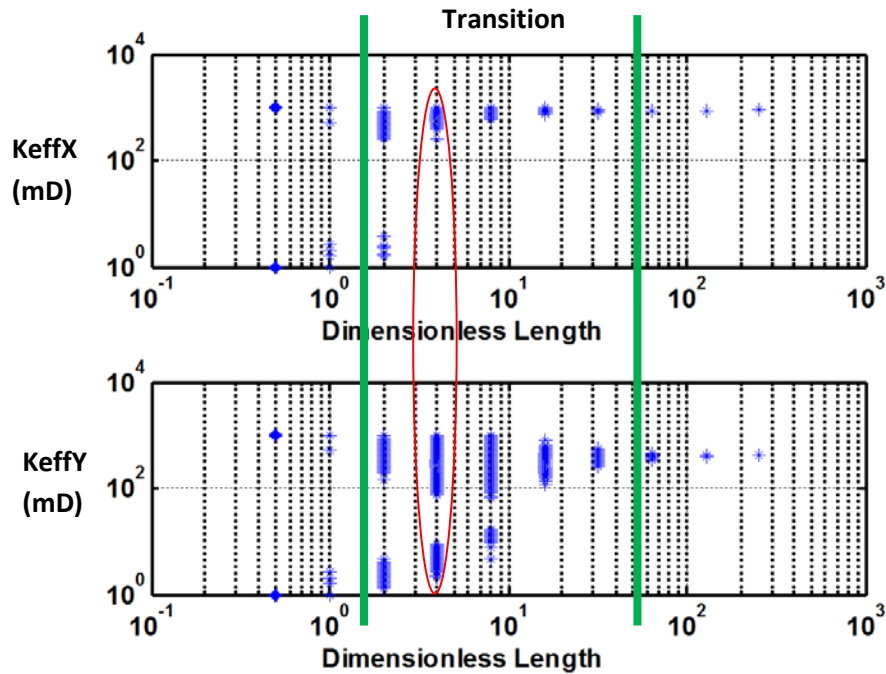


Figure 5.7: Effective values at different sample volumes for scenario A in X and Y-directions

Table 5.3: Effective Values (mD) and Averages for Scenarios A, B and C

	KeffX	KeffY	KeffH	KA	KG	KH
Scenario A	884.35	424.57	654.46	900.09	501.16	9.91
Scenario B	906.66	106.99	506.82	900.09	501.16	9.91
Scenario C	902.17	40.99	471.58	900.07	501.10	9.90

Based on the proposed model in the previous chapter, the boundaries of the transition regime is determined. The thick green lines show the boundaries for scenario A in Figure 5.7. Based on the proposed model, the lower boundary is located at the grid block size somewhere between 1/30 and 1/5 times the object size and the upper boundary is located at the grid block size somewhere between 2.5 and 7 times the object size. Considering the proposed model and the geological feature sizes on scenarios A, B and C, the scales in transition are determined for all scenarios. To calculate the boundaries, three values are selected for lower and upper boundaries in the estimated ranges, see Table 5.4.

Table 5.4: Calculating the Boundaries of Transition Regime for Scenarios A, B and C

Object size in X direction (m)	Lower boundary grid size (m)	Scale ID for lower boundary	Upper boundary grid size (m)	Scale ID for upper boundary	Scale ID in transition
	$1/6 \times \text{object size}$		$6 \times \text{object size}$		
10.24	1.71	2	61.44	7	2 to 7
51.2	8.53	4	307.2	9	4 to 9
256	42.67	6	1536	above 10	6 and above
	$1/5 \times \text{object size}$		$2.5 \times \text{object size}$		
10.24	2.048	2	25.6	6	2 to 6
51.2	10.24	4	128	8	4 to 8
256	51.2	7	640	above 10	7 and above
	$1/30 + (1/5 - 1/30)/2 = 7/60 \times \text{object size}$		$2.5 + (7 - 2.5)/2 = 4.75 \times \text{object size}$		
10.24	1.2	1	48.64	between 6 and 7	1 to 7
51.2	5.97	between 3 and 4	243.2	9	3 to 9
256	29.87	6	1216	above 10	6 and above

Based on the calculations shown in Table 5.4, scales in transition are scale IDs 2 to 6 for scenario A, scale IDs 4 to 8 for scenario B and scale IDs 7 and above for scenario C. Note that we picked common scale IDs for the three calculations. Consequently, size 8×8 , that is equivalent to the scale ID 4, is selected for the grid blocks since it is in the transition regime for scenarios A and B both, while still in discrete regime for scenario C with very large objects, Table 5.5. The red ellipse in Figure 5.7 highlights the picked grid size in transition for scenario A. The modeling at the grid block size in the transition regime is an important goal of the chapter.

Table 5.5: Picking a Grid size in Transition Regime for Training Images

Object size in X	Object size in Y	Grid Size in X & Y-directions	l_x/a_x	l_y/a_y	Dimensionless Length	Regime
$512/50 = 10.24$	2	8×8	$8/10.24$	$8/2$	4	Transition
$512/10 = 51.2$	2	8×8	$8/51.2$	$8/2$	4	Transition
$512/2 = 256$	2	8×8	$8/256$	$8/2$	4	Discrete

5.6 Quick Look at Variance Reduction through Upscaling

The variance decreases when the size of the sample volume increases. Figure 5.8 and Figure 5.9 show the variance reduction caused by increasing the sample volume size for scenarios A, B and C. While scaling up at different sample volumes in X-direction, a decreasing trend in variance at all scales is observed, Figure 5.8. There is an increasing trend for the first few scales in the Y-direction which could be interpreted as a grid artifact, see Figure 5.9. Looking at scenarios A, B and C, the permeability in Y-direction is dominated by the shale. Due to mixing the proportion of the low permeability values while applying the scale up technique, percentage of near shale permeabilities goes up and the proportions of high values goes down. Recall that flow-based upscaling is non-linear.

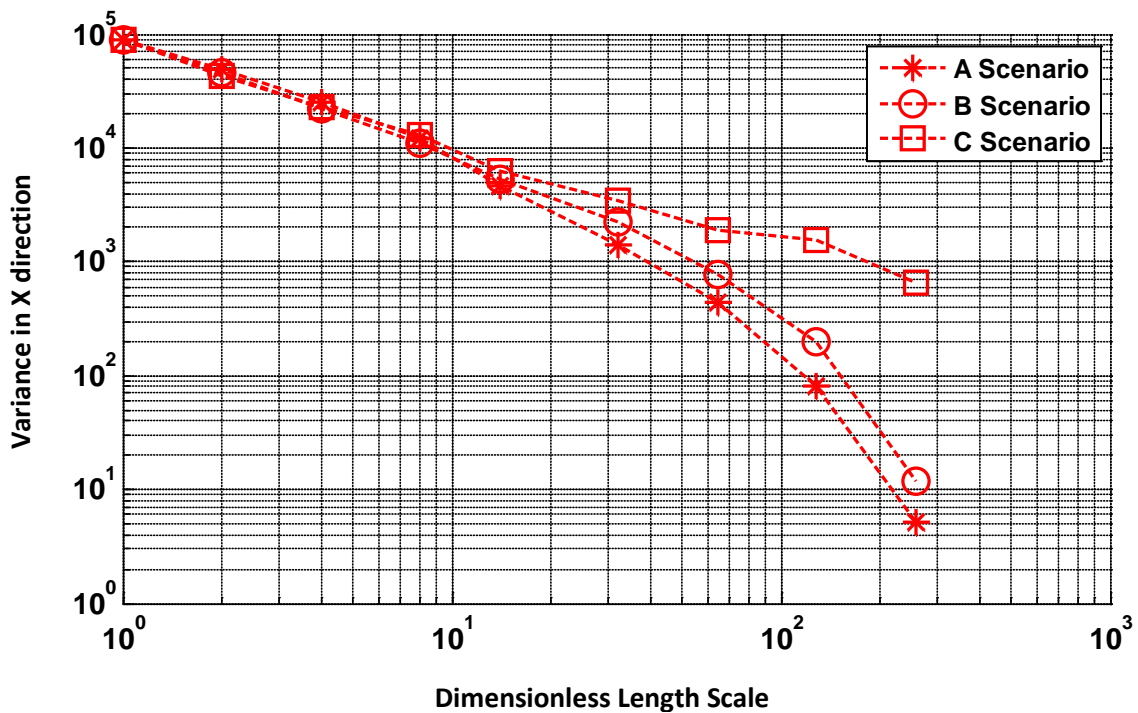


Figure 5.8: Variance versus sample volume size in X-direction

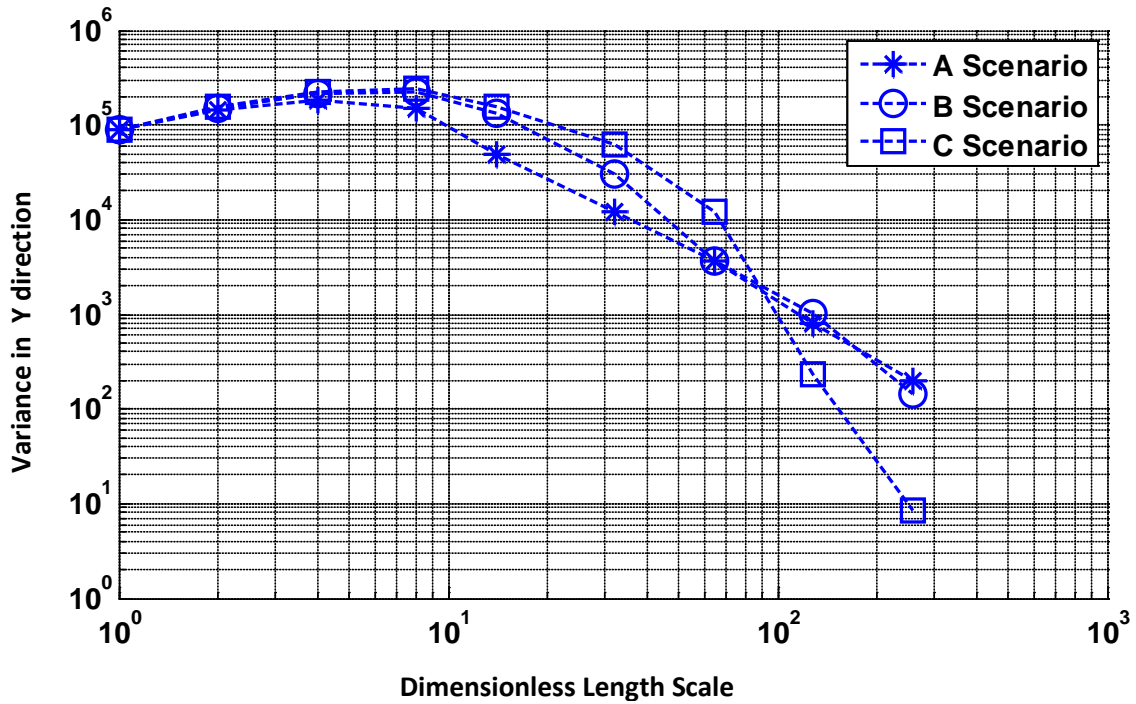


Figure 5.9: Variance versus sample volume size in Y-direction

5.7 Plots of the Models at the Selected Grid Size in Transition

The grid size 8 at the transition zone was chosen for scenarios A and B. The following discussion is aimed at practical modeling considerations in the transition regime. To begin with, the high resolution models are upscaled to coarse models by considering different sample volume sizes. The upscaled models in Y-direction and at three scales of grid size 2, 4 and 8, are presented in Figure 5.10. The 64 by 64 models, that are in the transition regime for scenarios A and B, are selected for further studies. The models are named as scenarios 1 and 2 which are obtained by upscaling scenarios A and B. A continuous simulation framework is considered at the transition regime in the upcoming sections. Scenario C is also plotted in Figure 5.10 to compare at the 3 scales and it is still in the discrete regime and not in the transition at the shown scales.

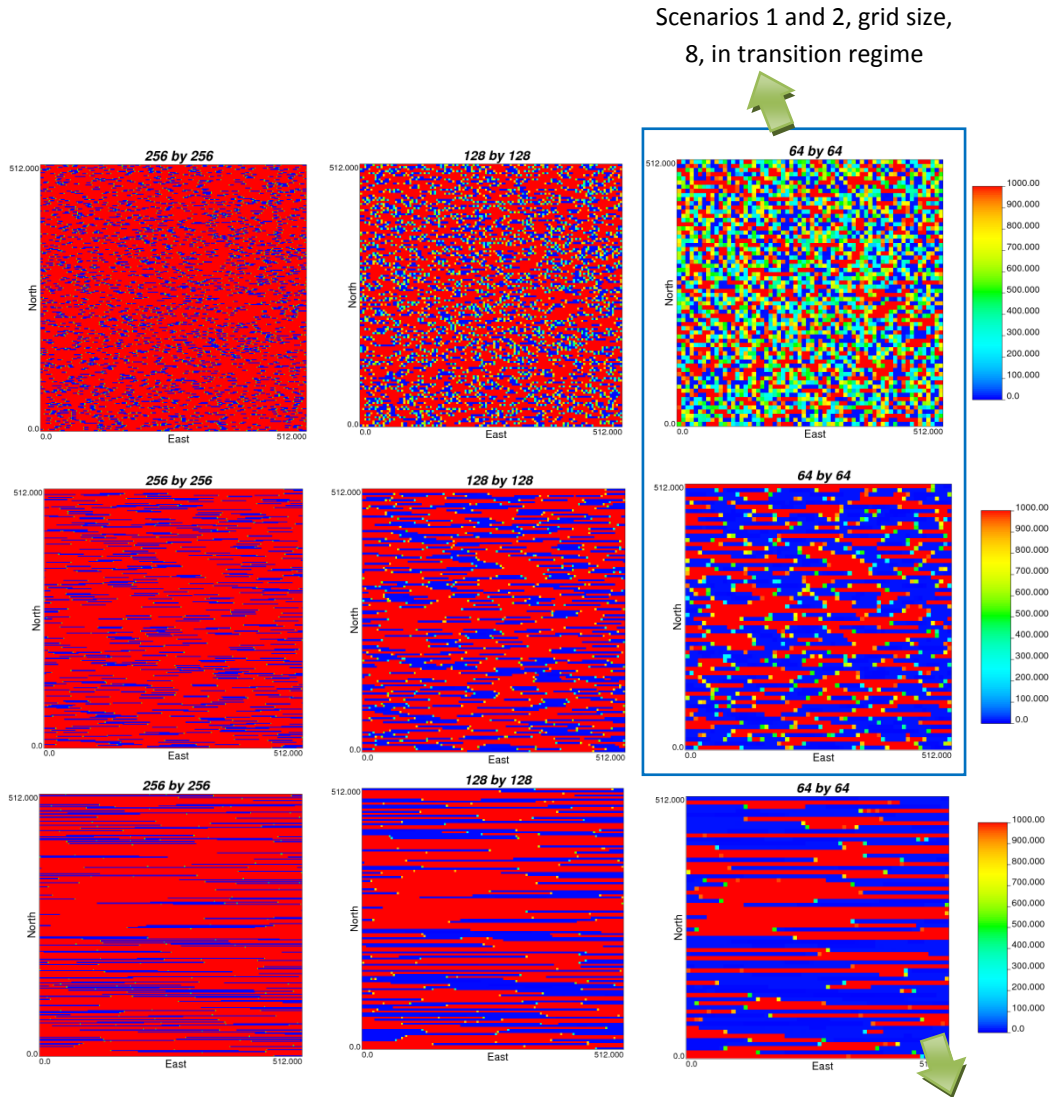


Figure 5.10: Pixel plot of the upscaled scenarios A, B and C at 3 scales in Y-direction (KeffY has been plotted)

5.8 Histograms and Variograms of the Upscaled Models in Transition, Scenarios 1 and 2

The distribution of the scenarios 1 and 2 are considered as reference distributions for simulation and also there is a need for the spatial correlation of scenarios 1 and 2 to conduct continuous simulation on the permeability. As the permeability in Y-direction is dominated by the shale, so it is more significant than X permeability. Hence, the focus

would be on the simulation of the Y permeability. There is a similar procedure to practice simulation on X permeability as well. Figure 5.11 shows the histogram, which is the reference distribution, for Y permeability of scenario 2. The histograms of the permeability in the X and Y-directions are expected to be different for the upscaled models because of averaging. Figure 5.12 to Figure 5.14 show the modeled horizontal and vertical variograms for scenarios 1, 2 and 3. The horizontal variogram is plotted for X-direction and the vertical variogram is plotted for Y-direction. Scenario 3 is in transition at grid size 8 and the variograms are just plotted for comparison and not for simulation.

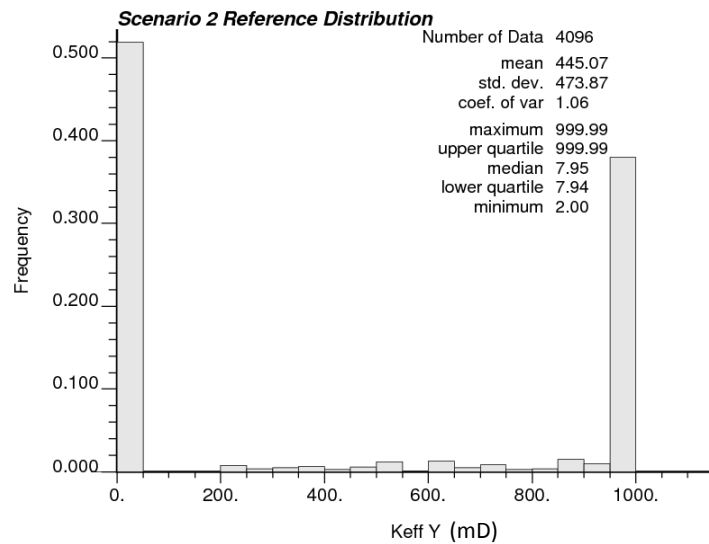


Figure 5.11: Distribution of Y permeability for scenario 2 (Reference distribution)

To fit the variogram, the first point of the variogram plays a very important role. Also, the horizontal range should be equal to the object size in the X-direction plus the block size of averaging. The vertical range would be the grid block size.

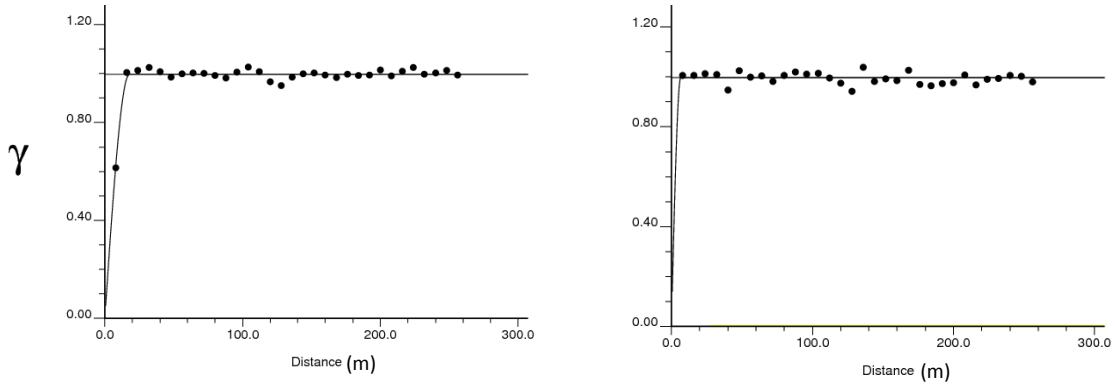


Figure 5.12: Fitted variograms for scenario 1, LHS: Horizontal variogram and RHS: Vertical variogram (in Transition)

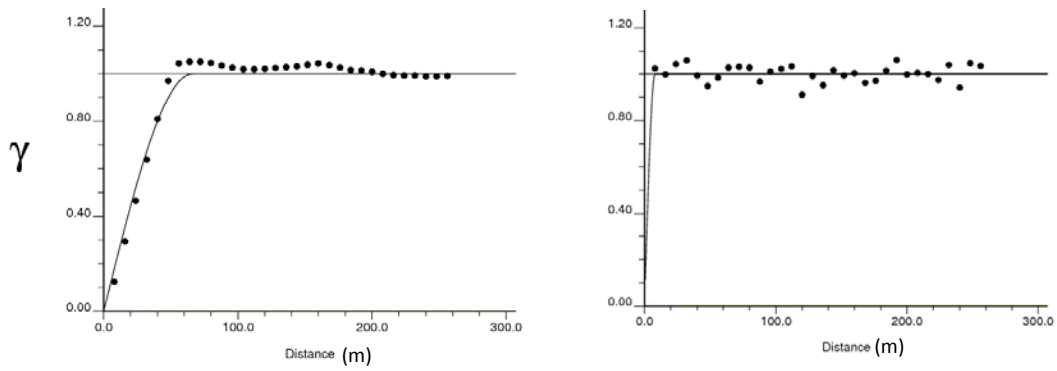


Figure 5.13: Fitted variograms for scenario 2, LHS: Horizontal variogram and RHS: Vertical variogram (in Transition)

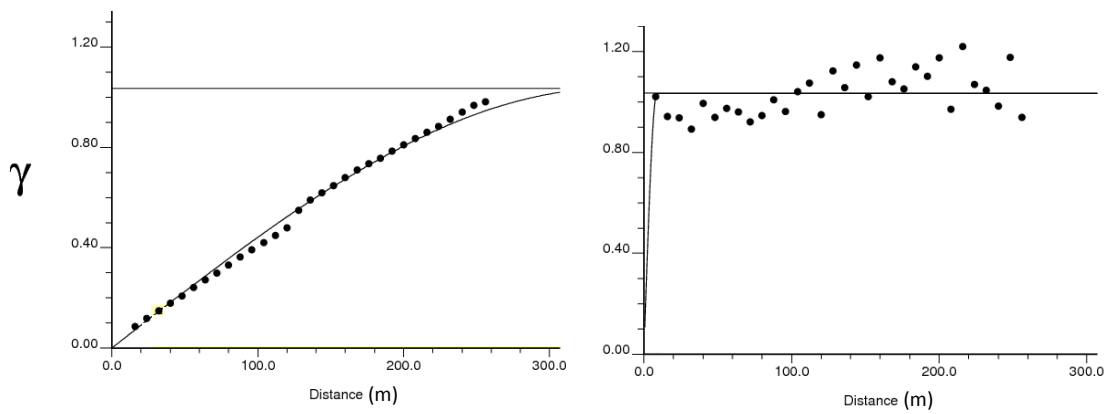


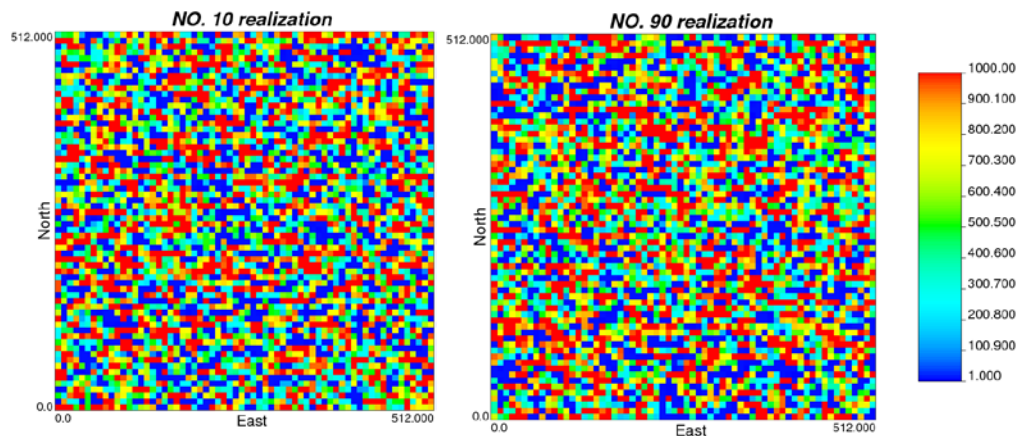
Figure 5.14: Fitted variograms for scenario 3, LHS: Horizontal variogram and RHS: Vertical variogram (in Discrete Regime)

The reference distribution and horizontal / vertical variograms of scenarios 1 and 2 are used to simulate realizations by the continuous Gaussian simulation technique which is applied through SGSIM program (GSLIB).

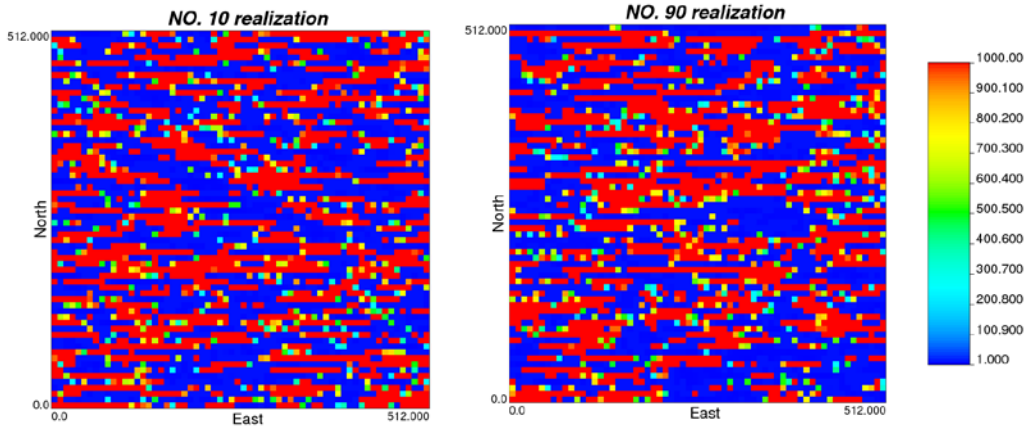
Being in the transition regime, histograms of effective values are multimodal and have very high variance. The flow character is sensitive to both histograms and the spatial structure as well. The variograms of the high variance features are significantly important to represent the spatial structure despite the fact that the histograms cannot show the spatial structure and the variograms show the spatial structure.

5.9 Continuous Simulation at Grid Size in the Transition Regime

The SGSIM program was used to simulate 100 realizations of permeability in the Y-direction considering the reference distribution in Y-direction and the variograms of the scenarios 1 and 2. The simulated models are called models 1 and 2 respectively. The realizations numbered 10 and 90 are plotted as representative ones, Figure 5.15. The plots show good agreement with the reference scenario 1 and 2. However to check the simulated models, histograms and variograms of the 100 realizations are reproduced in the next part.



a) Model 1: Simulated scenario with minimum object length

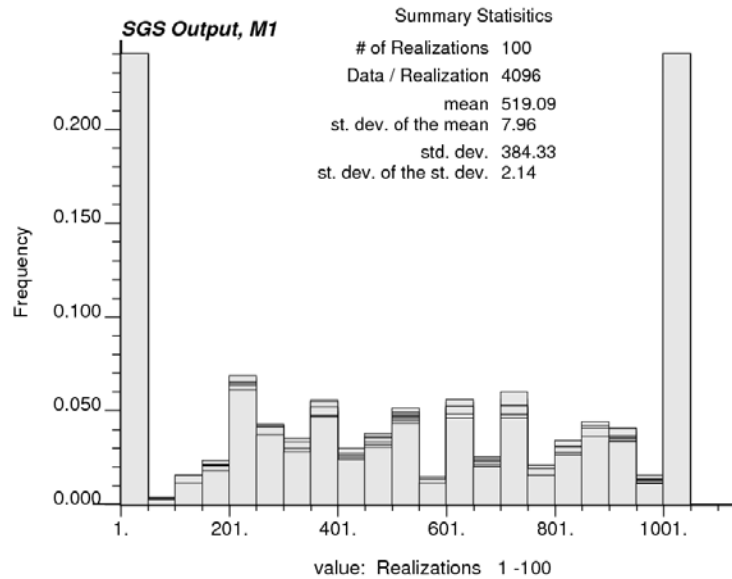


b) Model 2: Simulated scenario with medium object length

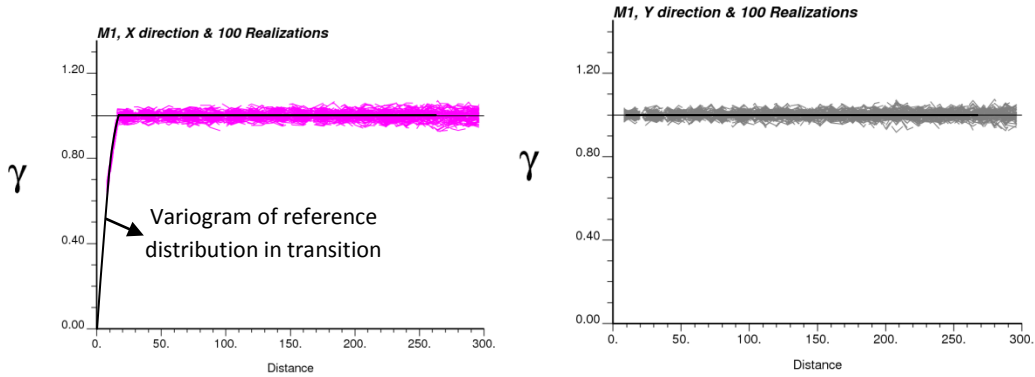
Figure 5.15: Plots of simulated Y permeability, realizations # 10 & 90

5.10 Variogram and Histogram Reproduction

The variogram of each realization was calculated to check variogram reproduction. The HISTPLTSIM, GSLIB program, is also used to calculate the histogram for each realization in the simulated models and it aids us to monitor histograms reproduction. Figure 5.16 and Figure 5.17 show the variogram reproduction in X and Y-directions and the histogram reproduction for simulated models 1 and 2.



a) Histogram reproduction for 100 realizations

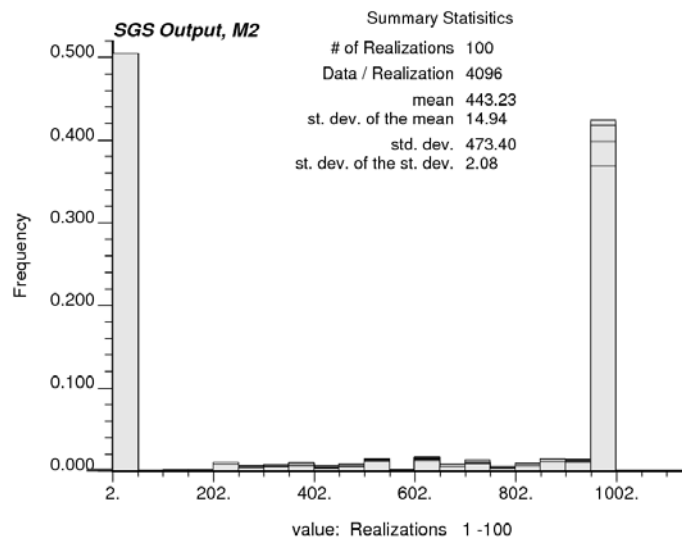


b) Variogram reproduction for 100 simulated realizations; LHS: Horizontal, RHS: Vertical

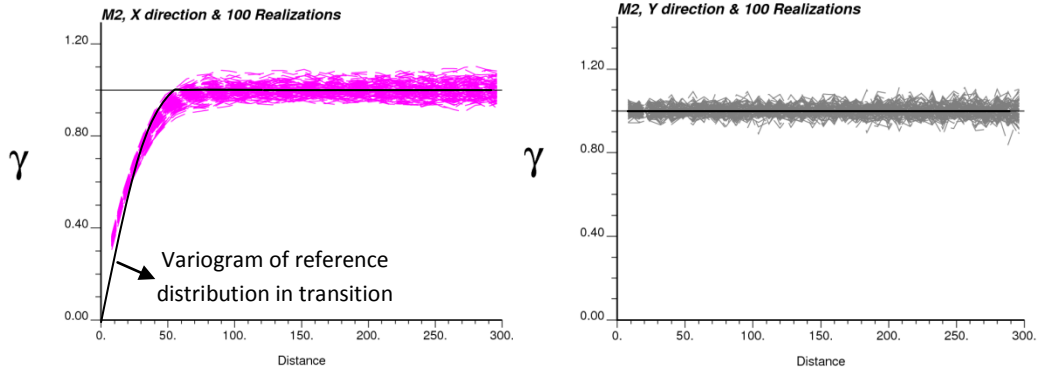
Figure 5.16: Variogram and histogram reproduction, simulated model 1

The variograms show structure very close to the original high resolution models, scenarios A and B, both in X and Y-directions. The reproduced histograms are also compatible with the reference distributions used for simulating the models.

The conclusion is that while taking care of the large variability in the univariate distribution and spatial statistics; sequential Gaussian simulation, a continuous modeling approach, has been successfully applied to simulate the geological models at grid size 8 in the transition regime. Significantly, the variogram continuity of the low values has a big impact on the simulated models.



a) Histogram reproduction for 100 realizations

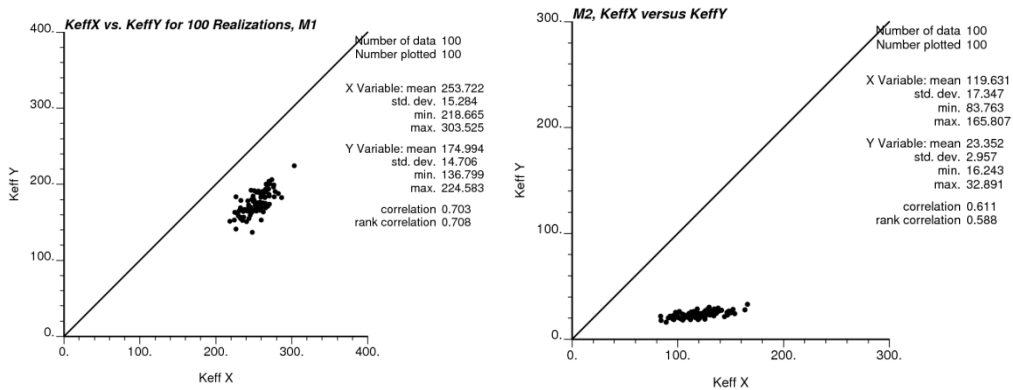


b) Variogram reproduction for 100 simulated realizations; LHS: Horizontal, RHS: Vertical

Figure 5.17: Variogram and histogram reproduction, simulated model 2

5.11 Scatter Plots of Simulated Permeability in Y-direction

By applying the FLOWSIM program, flow based upscaling is performed on the simulated realizations. Each realization is upscaled to one value to compare the effective permeability between the simulated models. The scatter plots of the effective permeabilities for 100 realizations in Y-direction versus X-direction are shown in Figure 5.18. It is apparent that the scatter plot related to the model with the larger barrier has lower effective permeability, Figure 5.18b.



a) Effective values for simulated model 1

b) Effective values for simulated model 2

Figure 5.18: Scatter plots of effective values (mD) for 100 realizations

A continuous barrier has a large influence on the results and will have an impact on flow simulation, production performance, reservoir management, well design and selection of the horizontal and vertical wells.

5.12 Flow Simulation on the Scenarios and Simulated Models to Compare

In this part of the thesis, a comparison of the different geological models is performed; high resolution training images, upscaled models and simulated models. Horizontal and vertical flooding tests are applied on each model. In case of the vertical flooding test (for the Y-direction), flow enters from the front side and in case of the horizontal flooding test (for the X-direction), flow enters from the left side of the model. The solver in MRST MATLAB toolbox is applied to solve the single phase pressure equation for a flow driven with Dirichlet and Neumann boundary conditions. The geological models are scenarios A, B, C, 1, 2, 3 and several (isotropic / anisotropic) homogeneous media to compare. The only parameters in the single phase equations are the permeability and the fluid viscosity. For all mentioned scenarios, the permeability is non-homogeneous and anisotropic.

The viscosity is specified by saying that the reservoir is filled with a single fluid, for which the default viscosity value equals unity. The viscosity is set to 1 cp and density is set to 1014 kg/m³. The initial reservoir pressure is set to 0 and single-phase saturation is equal to 0 as well. The Neumann conditions (flux of 10 m³/day) are imposed on the global left-hand side in case of horizontal flooding and also on the front side in case of vertical flooding. Dirichlet boundary conditions, $p = 0$, are also set on other sides of the models. Figure 5.19 shows the initial and boundary conditions used for horizontal and vertical flooding tests. Ultimately, the computed cell pressures with unit '**bar**' resulted by the basic flow simulation on the geological models are plotted to compare the models.

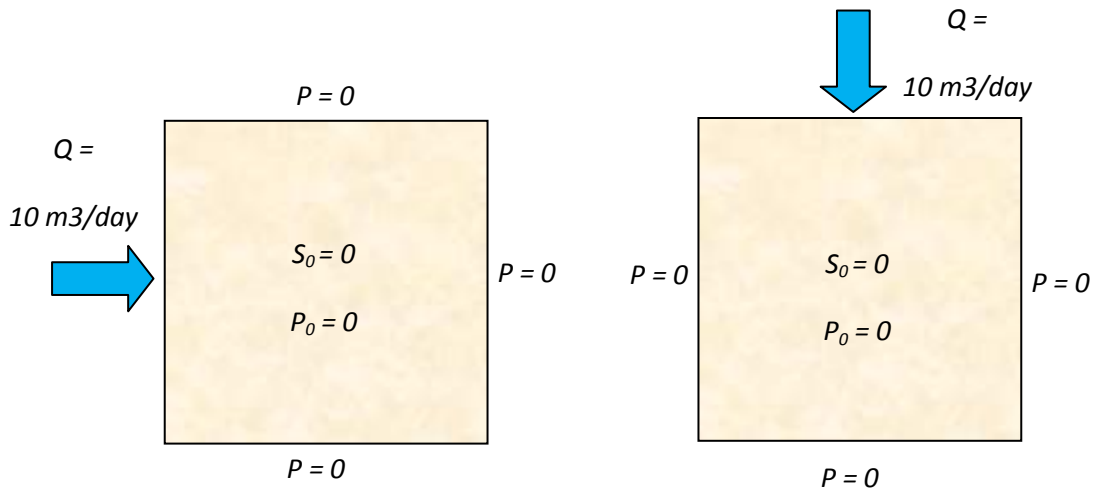


Figure 5.19: Horizontal and vertical flooding tests on a geological model

There are a couple of significant points that can be made.

POINT 1: The 512 by 512 model is similar to the 64 by 64 model.

Flow simulation has been conducted on the original high resolution models in the discrete regime, Figure 5.4 and also on the upscaled 64 by 64 models in the transition regime. As a sample case, pixel plots of effective permeability in X and Y-directions for scenario 2 are also shown in Figure 5.20. Each model is put to the horizontal and vertical flooding tests considering the initial and boundary conditions mentioned above, Figure 5.19.

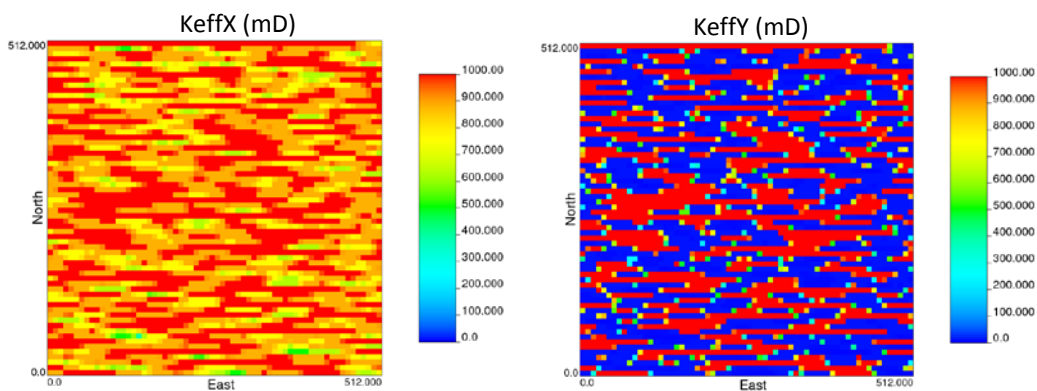


Figure 5.20: Pixel plot of Keff in X and Y-directions for Scenario 2

The flow response is shown by plotting the pressure distribution on the gridded models. The pressure distribution on scenarios B and 2 are presented in Figure 5.21. To quantify the similarities, cross plots of flow responses (pressure distribution) are presented in X

and Y-directions, Figure 5.22. The corresponding correlation coefficients are calculated and demonstrate very high correlation between the high resolution model and the upscaled one. With respect to the flow responses, it is confirmed that the 512 by 512 gridded model is similar to the 64 by 64 gridded model. Similar results are obtained for the other two models where the correlation coefficient is very close to 1 for all cases. The flow responses are compared on the 512 by 512 grid resolution models.

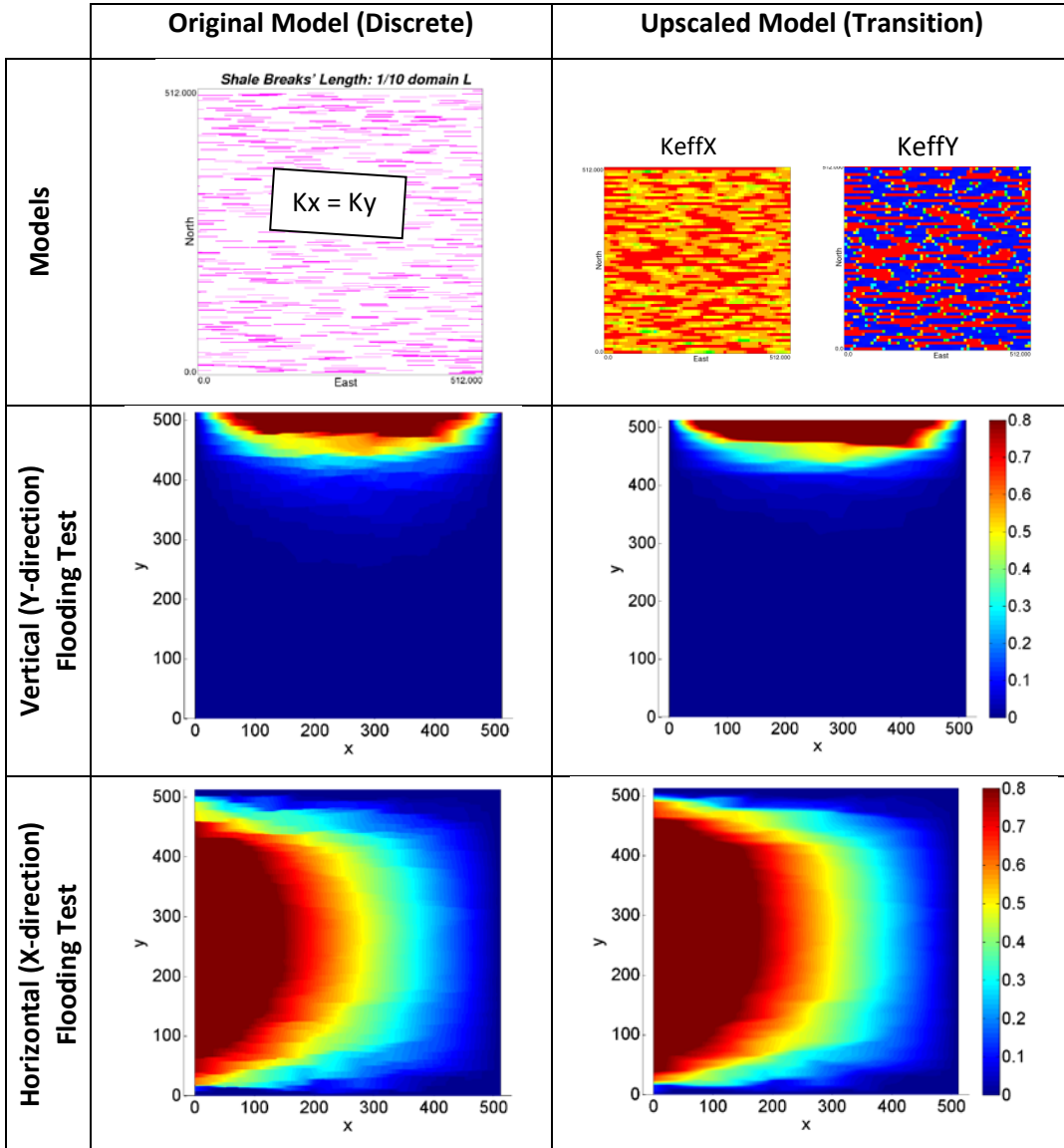


Figure 5.21: Flow response (pressure distribution (bar)), scenario B and 2 discrete vs. coarser scale under horizontal and vertical flooding tests at 512 by 512 grid resolution (Considering both KeffX and KeffY in flow simulation)

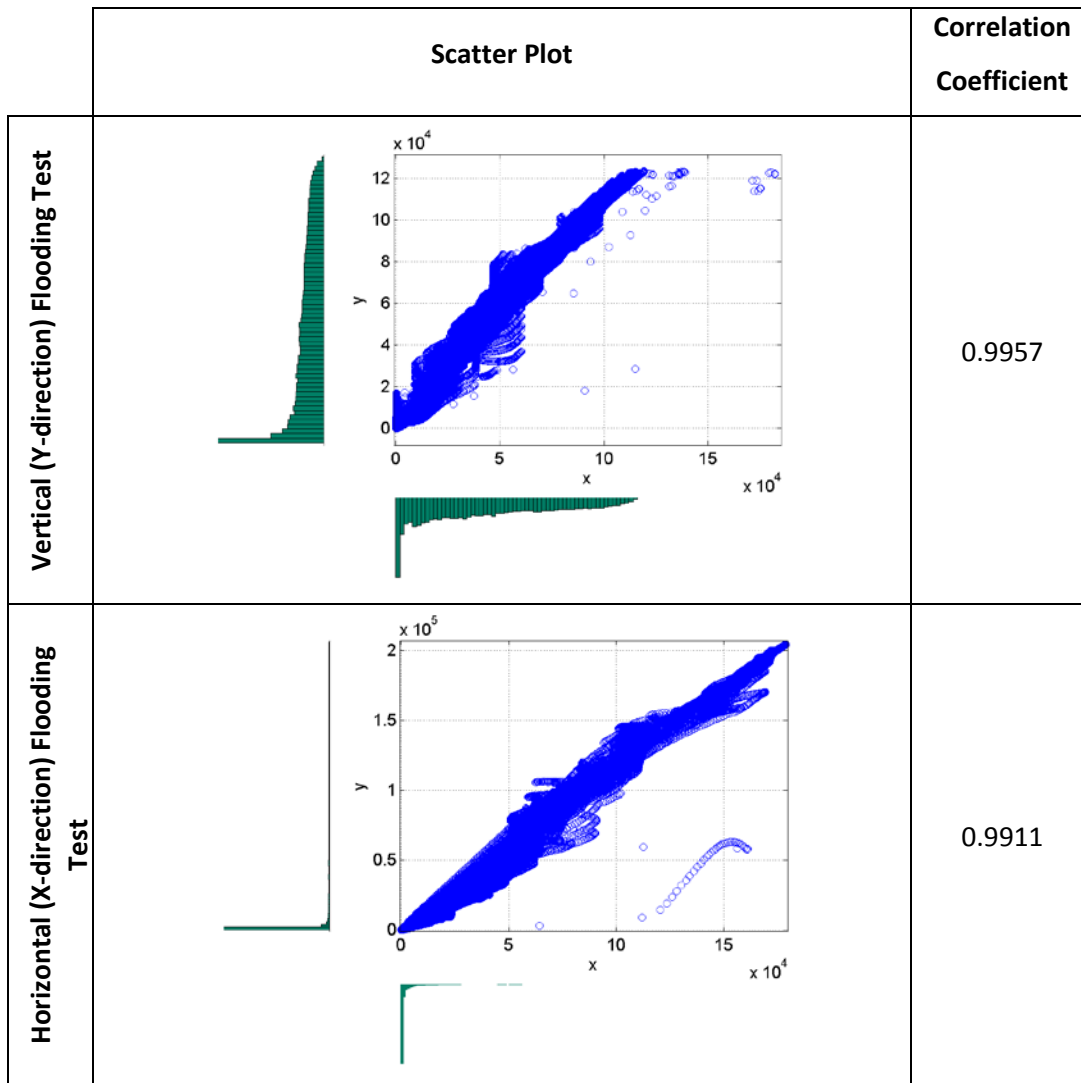
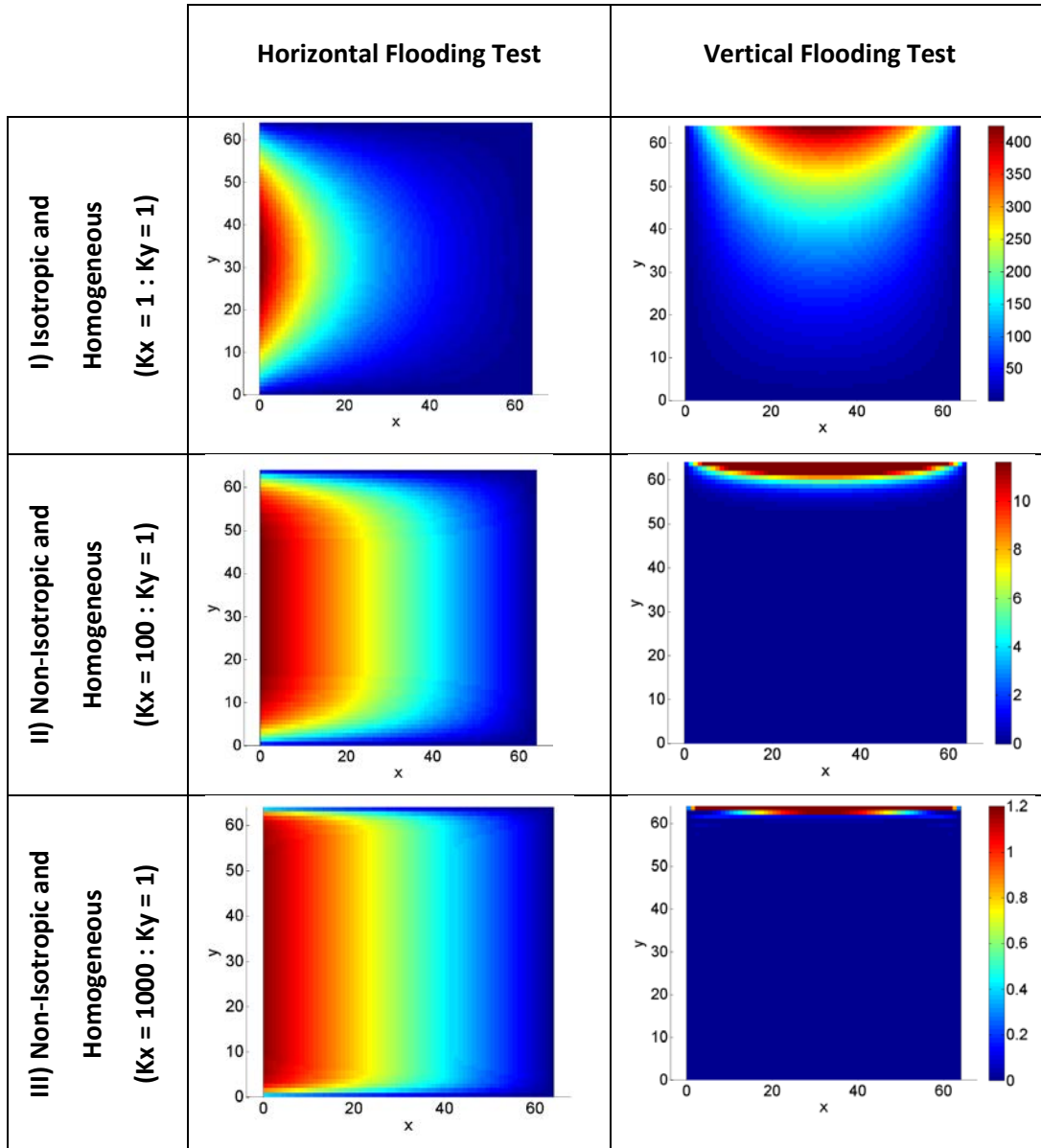


Figure 5.22: Scatter plots and correlation coefficients for flow responses, scenarios B and 2

POINT 2: Flow response on homogenous media (isotropic / non-isotropic)

In a homogenous medium, permeability is constant in each direction ($K_x = a$, $K_y = b$, $K_z = c$). In an isotropic medium, permeability at different directions is the same ($K_x = K_y = K_z = d$). Scenarios A, B and C are all non-homogenous and non-isotropic. In this section, three homogeneous media are generated with constant vertical permeability equal to 1mD and constant horizontal permeability equal to 1, 100 and 1000mD respectively. The grid resolution is 64 by 64 and the homogeneous flow response is shown in Figure 5.23. For the 1:1 case, horizontal and vertical pressure response looks exactly the same. The other two cases are homogeneous but anisotropic and we achieve different pressure responses for the vertical and horizontal flooding tests. We can observe the anisotropy

as the next dimension and see how flow can affect the larger area horizontally for the case with larger horizontal permeability (1000:1 case). In case of vertical flooding test, flow can move through larger regions of the reservoir for models with less difference between horizontal and vertical permeability and vice versa. When the model moves towards a more anisotropic state, the pressure response range is decreased as well; see the color bars ranges in Figure 5.23.



a) LHS: Horizontal flooding test

b) RHS: Vertical flooding test

Figure 5.23: Homogenous flow response (bar) on 64 by 64 grid resolution

POINT 3: Flow response on heterogeneous and anisotropic media

In this section, the grid size effect is the key point since flow simulation is performed on the upscaled models, scenarios 1, 2 and 3, in grid size 8 that is in the transition regime for scenarios 1 and 2. Pressure distributions (flow responses) are shown in Figure 5.24 on the 64 by 64 grid resolution. All scenarios are anisotropic and heterogeneous.

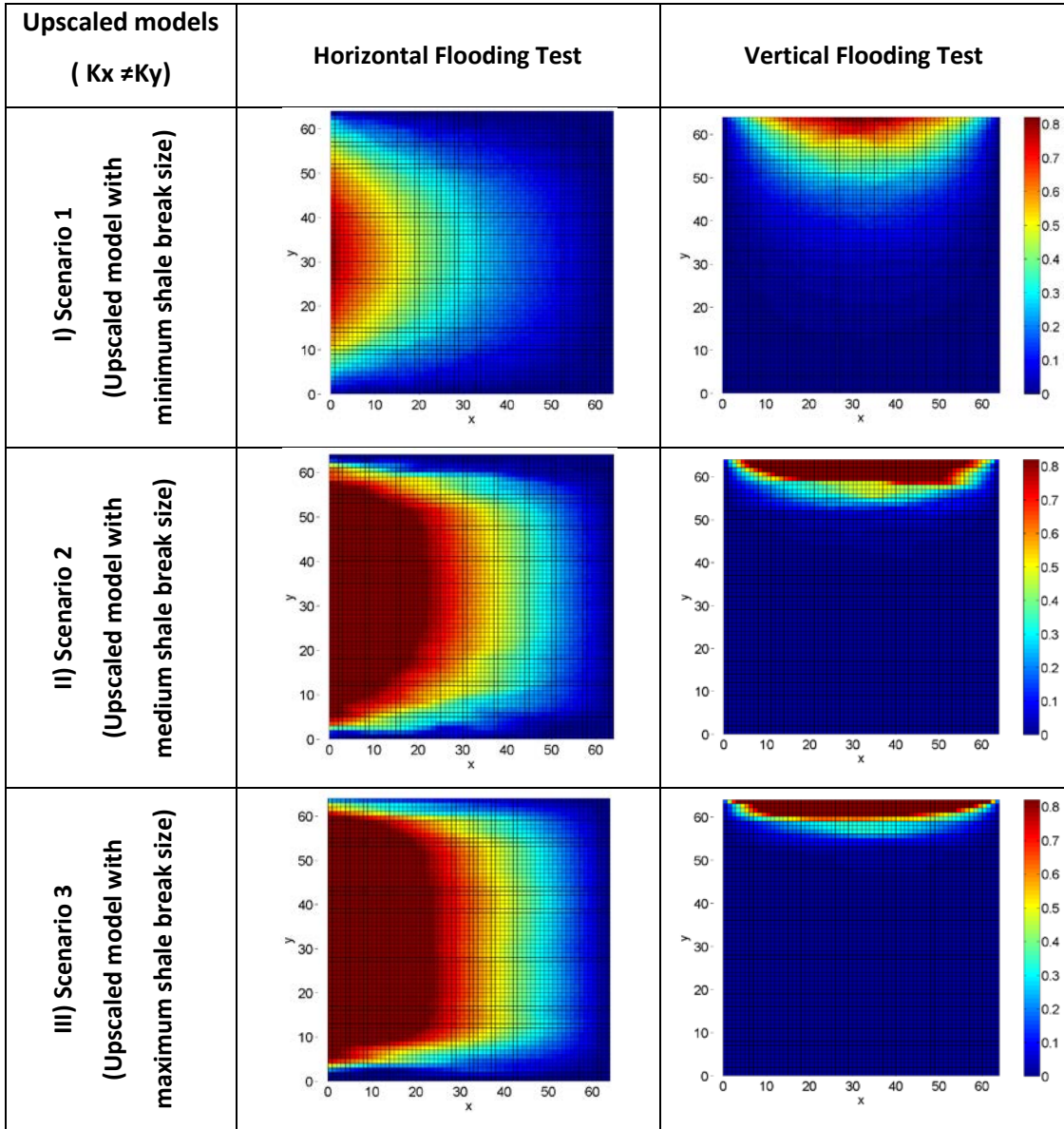


Figure 5.24: Comparison of pressure distribution (bar) on scenarios 1, 2 and 3 under horizontal and vertical flooding tests, 64 by 64 grid resolution (Considering both K_{effX} and K_{effY} of scenarios to get flow responses).

By increasing the size of the shale breaks, flow can move through larger areas of the reservoir horizontally (in X-direction) and smaller areas of the reservoir vertically in (Y-direction). There is close behavior between the flow response for scenario 1 and the homogenous isotropic case, Figure 5.24 I and Figure 5.23 I. The model with minimum shale breaks' length behaves similar to the isotropic homogeneous case. Also, scenario 2 is close to case 100 : 1 and scenario 3 is comparable to case 1000 : 1 visually. The effect of increasing the shale break size horizontally is approximately similar to the effect of increasing the horizontal permeability on the flow responses.

POINT 4: Transition modeling with an appropriate variogram and histogram converges to the original discrete model.

In this section, the flow responses are presented for the simulated models and the upscaled models at the grid block size 8 in transition. The similarity/difference between the simulated models and the upscaled models are investigated by cross plots of the pressure responses and the corresponding correlation coefficients.

The key point is that simulation has been conducted on the vertical permeability (in Y-direction) so the flow response is compared to the flow response obtained by the flow simulation on the vertical permeability of the upscaled models (Keffy).

Figure 5.21 and 5.22 confirm that the 512 by 512 model is the same as the 64 by 64 one. Therefore by finding the similarities between the simulated models and the upscaled 64 by 64 models, we can reasonably conclude that the simulated model is similar to the 512 by 512 model and transition modeling with a correct variogram and histogram successfully converges to the correct discrete model.

In Figure 5.25, one random realization of the simulated models and the upscaled models in transition (in Y-direction) are put to horizontal and vertical flooding tests for comparison.

For a real model, the correct variogram and histogram are obtained based on the core data, log data and seismic data.

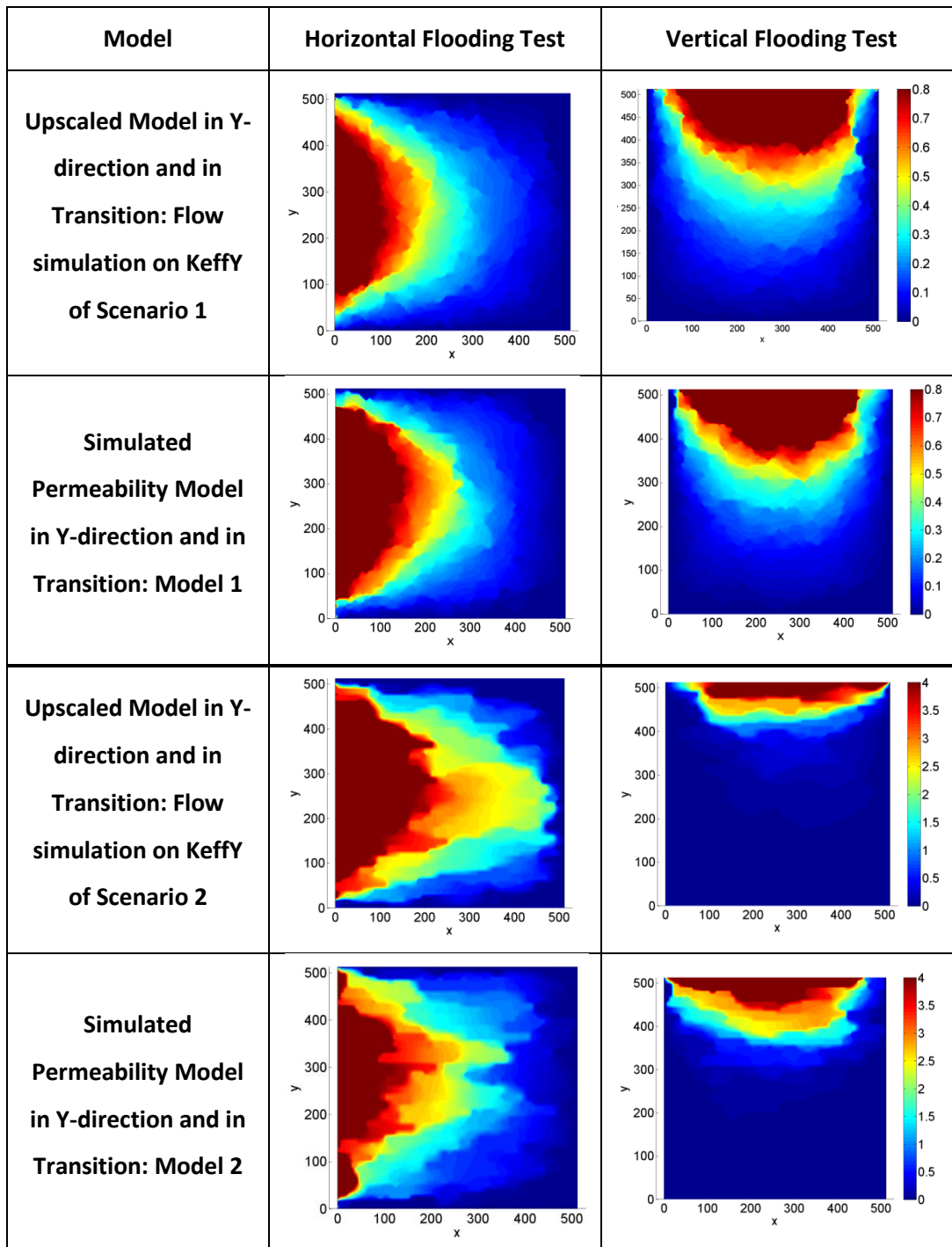


Figure 5.25: Comparison between the pressure (bar) on simulated vertical K models and scenarios 1 and 2 in Y-direction (all in transition regime) and considering JUST KeffY of scenarios to get flow responses and to compare.

To quantify the closeness between the source model and the simulated one, the correlation coefficients and cross plots of the flow responses are used. The cross plots are all positively correlated because of applying the same boundary conditions and there is strong correlation in all cases. 0.85 and more than that can be considered as acceptable values for high correlation coefficient. There is a stronger correlation in the horizontal direction compared to the vertical one. Figures 5.26 to 5.29 show the cross plots in logarithmic scale and the correlation coefficients for both horizontal and vertical flooding tests for the upscaled models and simulated models in transition regime. The scatter plots have been plotted for every 5th data points. Looking at the cross plots and corresponding correlation coefficients, the strong correlations confirm that the anisotropy is preserved in simulated models at grid block size 8 picked in the transition regime and we can say that transition modeling with a correct variogram and histogram successfully converges to the correct discrete model.

Note that the simulated models are geostatistically simulated at a 64 by 64 grid resolution but flow simulation is performed at a 512 by 512 grid resolution since the exact same grid resolution is used in the flow simulation for comparison.

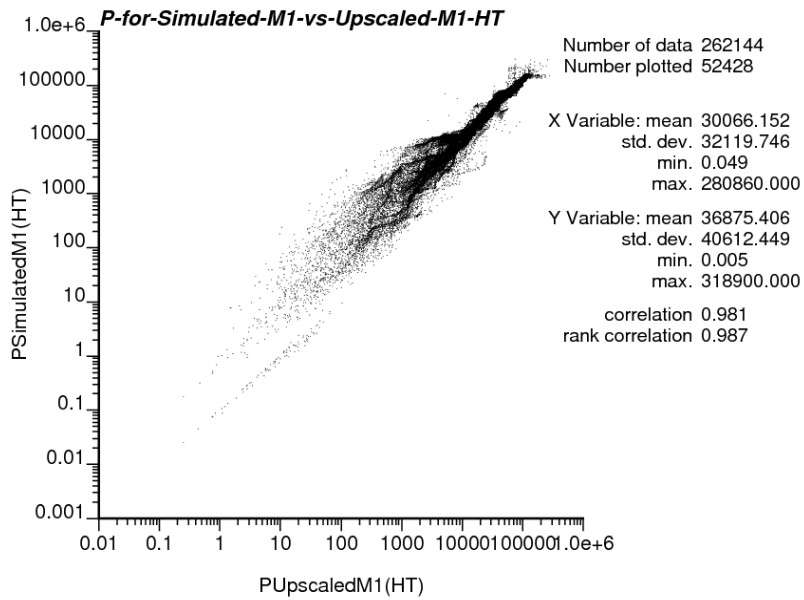


Figure 5.26: Pressure scatter (Cross) plot for scenario 1 and simulated model 1, horizontal flooding test (Considering only KeffY to get pressure distribution)

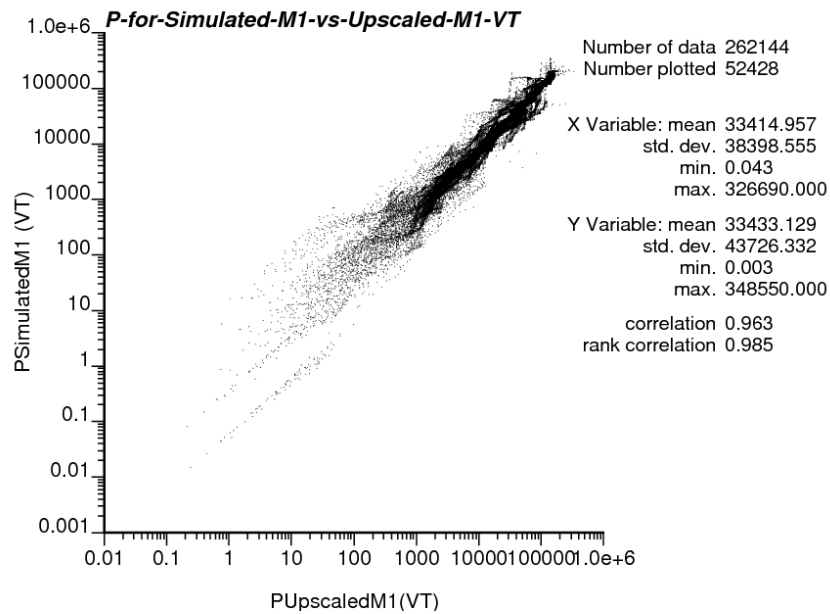


Figure 5.27: Pressure scatter plot for scenario 1 and simulated model 1, vertical flooding test (Considering only KeffY to get pressure distribution)

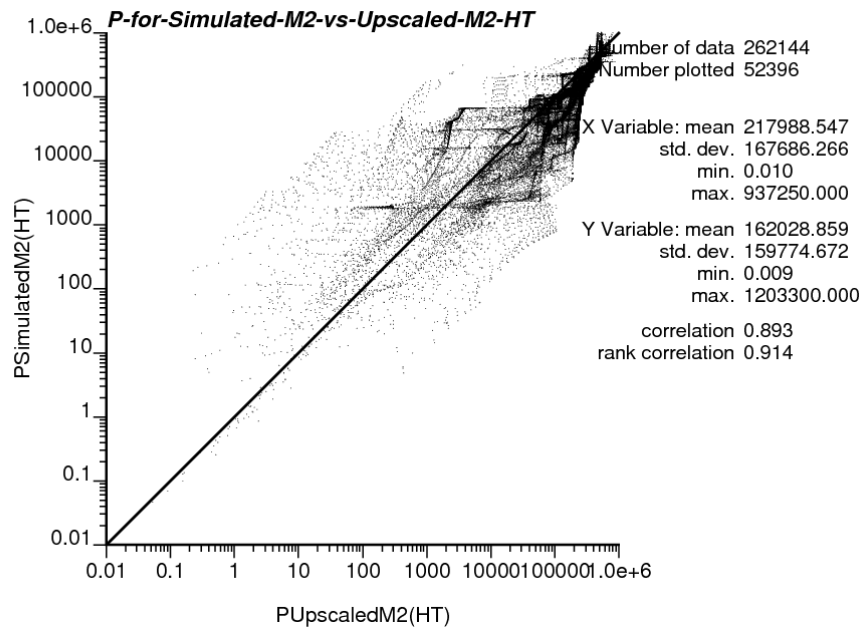


Figure 5.28: Pressure scatter (Cross) plot for scenario 2 and simulated model 2, horizontal flooding test (Considering only KeffY to get pressure distribution)

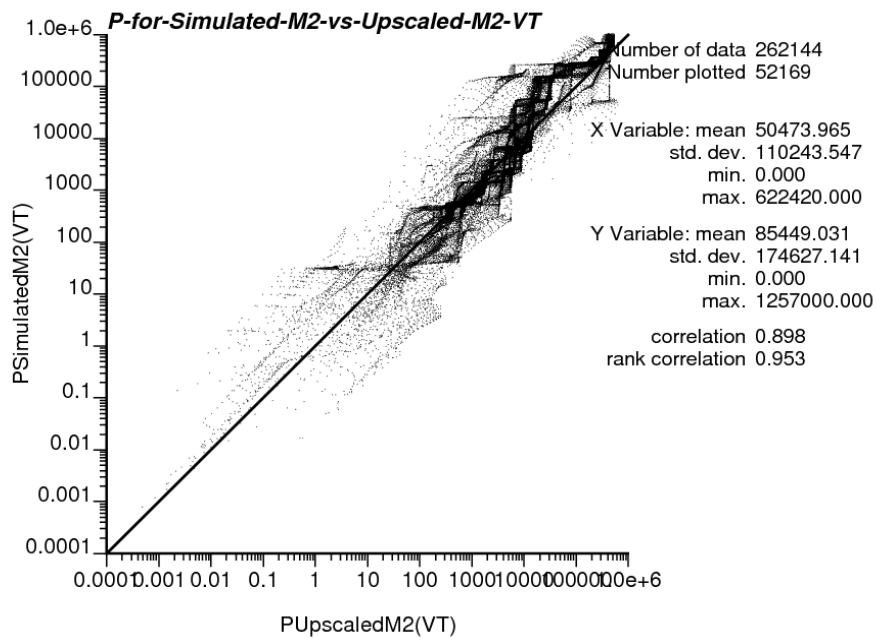


Figure 5.29: Pressure scatter plot for scenario 2 and simulated model 2, vertical flooding test (Considering only KeffY to get pressure distribution)

5.13 Conclusion

The objective of this chapter was to demonstrate the challenge of modeling in the transition regime. The experiments have been conducted on various synthetic models, three of which are original training images at high resolution (in discrete regime) which had different shale break length as flow barriers, three were upscaled models in transition regime and the last two were simulated models in transition regime by SGSIM program.

Following the upscaling section, the following points are noteworthy:

- Permeability varies with scale and variability is seen at all scales.
- Variance follows a decreasing trend when the size of the sample volume increases.
- In the horizontal direction, the effective values converge to the arithmetic average for all cases.
- At smaller sample volumes, vertical and horizontal permabilities vary significantly. Variance is reduced and variability becomes small and smaller when the scale of averaging is about 10 times the scale of the variability.
- Considering the variograms, with a fixed vertical continuity, that is pure nugget effect, it is obvious that the horizontal continuity has a dominant influence on the vertical permeability.
- Also when the scale of interest is less than the size of the features then the influence of the feature is seen in spatial continuity and not in the effective property at the scale of interest.
- There is variability at all scales, and grid scaling should be done considering engineering constraints. In reality, the scales of relevance are not entirely dictated by the scale of geology and it could be dictated by data and the flow process. Considering the engineering constraints and their impacts on the length scale could be among the future work.

Points on geostatistical simulation in the transition regime:

- Histograms cannot show the spatial structure and the variograms of the high variance features are very important.
- For simulation in the transition regime, a continuous approach is applicable and care should be taken specifying the univariate distribution and spatial statistics.
- At the transition zone, univariate distribution and spatial correlation must be preserved and it has to be modeled carefully to preserve the effective properties of the entire domain. Modeling is very sensitive to univariate distribution and spatial statistics.

With respect to the flow responses and the last section calculations:

- The 512 by 512 model in the discrete regime is similar to the 64 by 64 model in the transition regime. It means that the upscaled model at the picked grid size is an appropriate representative for the high resolution model.
- The effect of increasing the shale break size horizontally is approximately similar to the effect of increasing the horizontal permeability on flow responses.
- By applying continuous simulation, transition modeling with a correct variogram and histogram converges to the correct discrete model.
- A continuous simulation technique can be picked as the proper modeling technique in the transition regime.

6 Conclusions

Chapter One was the introduction chapter that described the problem addressed by the thesis. A literature review on various related topics; mesh types and mesh generators, solvers, reservoir modeling and upscaling and the notion of an REV was included.

Structured and unstructured grid types were reviewed in Chapter Two. The mathematical background of a flow simulator applicable for both structured and unstructured grids was explained. The finite volume form of the mass conservation law was presented to model single phase flow in the case of structured and unstructured grids. A finite volume simulator is based on connectivity lists for unstructured grids. Also, two examples of 2D and 3D discrete fracture networks meshed by unstructured grids were presented and the DFM mesh method for unstructured grids was explained. This chapter motivated applying different types of the grids in the discretization of a geological media and also looking at the flow process in the domain discretized by structured and unstructured grids. A subject of future work could be to create the connectivity lists of the sample DFMs and calculate the transmissibilities followed by solving the pressure equation on the unstructured mesh. It would be interesting to have an unstructured flow simulator and apply some upscaling calculations to find an appropriate unstructured coarse model.

The third chapter focused on upscaling and the established FLOWSIM program was modified to include a different iterative solver (SIP). The exact solution of the system of the pressure equations was obtained by applying a direct solver. The pressure convergence and permeability convergence to the exact solution were investigated. CPU time was also measured. It was shown that the direct solver generally took much longer than iterative solvers and the iterative algorithms converge to the exact pressure solution for all cases. The SIP algorithm implemented in the program was more stable and faster than the original LSOR algorithm. This chapter motivated concern for efficiency of upscaling, considering two different iterative algorithms. Investigation of the different types of boundary conditions applied in the FLOWSIM program and their

effect on the convergence of the algorithms and the efficiency of the FLOWSIM program could be in the future work item.

In Chapter Four, the concept of geological heterogeneity being represented discretely or as continuous properties was developed. The transition between discrete and continuous regimes was discussed in detail and linked to the notion of an REV. By defining three regimes, an extended view of modeling was proposed. The need to model in the transition regime below the scale of a proper REV was quantified. Finally, the lower and upper boundaries of the transition regime were studied. A modified REV plot was proposed to better represent real petroleum systems. This chapter motivated concern for upscaling and representing geological heterogeneity at different scales. Applying the workflow on a real dataset and plotting the modified REV plot for different geological systems are considered in the future work item as well.

The objective of the Chapter Five was to demonstrate the challenge of modeling in the transition regime. Experiments were conducted on several synthetic models in discrete and transition regimes and also related simulated models. It has been shown that by applying continuous simulation, transition modeling with a correct variogram and histogram converged to the correct discrete model with reasonably good approximation. Vertical permeability played the most important role in the models that were studied. The geostatistical simulation of permeability in the vertical and horizontal directions may be important in practice. Checking the results with real core data would be an interesting area of future work.

Bibliography

Aarnes J., Gimse T., Lie K.A. (2007). An Introduction to the Numerics of Flow in Porous Media Using MATLAB. *Geometric Modelling, Numerical Simulation, and Optimization Journal*.

Anggraeni S., Bowen D., Corbett P. (1999). The Use of The Probe Permeameter In Carbonates - Addressing The Problems Of Permeability Support And Stationarity. *Society of Petrophysicists and Well-Log Analysts*.

Aziz K., Settari A. (1979). Petroleum Reservoir Simulation. *Applied Science Publishers Ltd, London*.

Bajaj R. (2009), An Unstructured Finite Volume Simulator For Multiphase Flow Through Fractured-Porous Media, *MIT University*.

Bear J. (1972). Dynamics of Fluids in Porous Media. *American Elsevier Publishing Company*.

Begg S.H., King P.R. (1985). Modelling the Effects of Shales on Reservoir Performance: Calculation of Effective Vertical Permeability. *Society of Petroleum Engineers*.

Begg S.H., Carter R.R., Dranfield, P. (1989). Assigning Effective Values to Simulator Gridblock Parameters for Heterogeneous Reservoirs. *Society of Petroleum Engineers*.

Bloschl G., Grayson R.B., Sivapalan M. (1995). On the Representative Elementary Area Concept and its Utility for Distributed Rainfall-Runoff Modelling. *WILEY, Hydrological Processes*.

Brand C.W., Heinemann Z.E. (1990). A New Iterative Solution Technique for Reservoir Simulation Equations on Locally Refined Grids. *Society of Petroleum Engineers*.

Brown G.O., Hsieh H.T. and Lucero D.A. (2000). Evaluation of Laboratory Dolomite Core Sample Size Using Representative Elementary Volume Concepts. *WILEY, Water Resources Research*.

Chen T. (2009). New Methods for Accurate Upscaling with Full-Tensor Effects. *PhD Thesis, University of Texas*.

Chen T., Gerritsen M.G., Lambers J.V., Durlofsky L.J. (2010). Global Variable Compact Multipoint Methods for Accurate Upscaling with Full Tensor Effects. *Springer, Computational Geosciences*.

Clausnitzer V., Hopmans J.W. (1998). Determination of Phase-Volume Fractions from Tomographic Measurements in Two-phase Systems. *Elsevier, Advances in Water Resources*.

Corbett P., Jensen J.L. (1992). Estimating the Mean Permeability: How Many Measurements Do You Need?", *European Association of Geoscientists and Engineers*.

Corbett P., Jensen J.L., Sorbie K. S. (1998). A Review of Up-scaling and Cross-scaling Issues in Core and Log Data Interpretation and Prediction. *London, The Geological Society*.

Costanza-Robinson M.S. (2011). Representative Elementary Volume Estimation for Porosity, Moisture Saturation, and Air-water Interfacial Areas in Unsaturated Porous Media: Data Quality Implications. *WILEY, Water Resources Research*.

Dagan G. (1979). Models of Groundwater Flow in Statistically Homogeneous Porous Formation. *WILEY, Water Resources Research*.

Darman N., Pickup G.E. and Sorbie, K.S. (2002). A Comparison of Two-phase Dynamic Upscaling Methods Based on Fluid Potentials. *Springer, Computational Geosciences 6*.

Delleur J.W. (2006). *The Handbook of Groundwater Engineering: Scaling Issues*. CRC Press.

Desbarats A. (1989). Support Effects and the Spatial Averaging of Transport Properties. *Springer, Mathematical Geology*.

Deutsch C.V. (1989). Calculating Effective Absolute Permeability in Sandstone/Shale Sequences. *Society of Petroleum Engineers*.

Deutsch C.V. (1999). Reservoir Modeling with Publicly Available Software. *Computers and Geosciences*.

Durlofsky L.J. (1991). Numerical Calculation of Equivalent Grid Block Permeability Tensors for Heterogeneous Porous Media. *WILEY, Water Resources Research*.

Durlofsky L.J. (2005). Upscaling and Gridding of Fine Scale Geological Models for Flow Simulation. *Proceedings of the 8th International Forum on Reservoir Simulation, Italy*.

Eaton T.T. (2006). On the Importance of Geological Heterogeneity for Flow Simulation. *Sedimentary Geology*.

Eaton F.J. (2001). A Multigrid Preconditioner for Two-phase Flow in Porous Media. Ph.D. thesis, *University of Texas at Austin*.

Evesque P. (2000). Fluctuations, Correlation and Representative Elementary Volume (REV) in Granular Materials. *Cornell University Library*.

Farmer C.L. (2002). Upscaling: A Review. *WILEY, International Journal For Numerical Methods in Fluids*.

Ferziger J.H., Peric M. (2002). Computational Methods for Fluid Dynamics. *Book, Springer*.

Flint S.S., Bryant I.D. (2009). Sedimentary Flow Units in Hydrocarbon Reservoirs: Some Shortcomings and a Case for High-Resolution Permeability Data. *Wiley Online Library*.

Gary W.G., Miller C.T. (2004). Thermodynamically Constrained Averaging Theory Approach for Modeling Flow and Transport Phenomena in Porous Medium Systems: 1. Motivation and Overview. *Advances in Water Resources*.

Gates I.D., Wang J. (2012). Length Scales of Steam-based Oil Sands Recovery Processes such as SAGD and CSS. *Bulletin of Canadian Petroleum Geology*.

Gerritsen M.G., Durlofsky L.J. (2005). Modeling Fluid Flow in Oil Reservoirs. *Annual Review of Fluid Mechanics* 37.

Haldorsen H.H., Lake L.W. (1984). A New Approach to Shale Management in Field-scale Models. *Society of Petroleum Engineers Journal*.

Hassanizadeh M., Gray W.G. (2004). General Conservation Equations for Multi-phase Systems: 1. Averaging Procedure. *Advances in Water Resources*.

Hunt A., Ewing R. (2009). Applications of the Correlation Length: Scale Effects on Flow. *Lect. Notes Phys.* 771, 233–246.

Ito K., Seol Y. (2003). A 3Dimensional Discrete Fracture Network Generator to Examine Fracture-Matrix Interaction Using TOUGH2. *Berkeley, California*.

Jackson M.D. (2005). Three-dimensional Reservoir Characterization and Flow Simulation of Heterolithic Tidal Sandstones. *American Association of Petroleum Geologists*.

Jackson M.D. (2003). Upscaling Permeability Measurements Within Complex Heterolithic Tidal Sandstones. *Mathematical Geology*.

Karimi-Fard M., Durlofsky L., Aziz K. (2003). An Efficient Discrete Fracture Model Applicable for General Purpose Reservoir Simulator. *Society of Petroleum Engineers*.

Klaus S., Tanja C. (2007). Algebraic Multigrid Methods (AMG) for the Efficient Solution of Fully Implicit Formulations in Reservoir Simulation. *Society of Petroleum Engineers*.

Klie H., Wheeler M.F. (2005). Krylov-Secant Methods for Accelerating the Solution of Fully Implicit Formulations. *Society of Petroleum Engineers*.

Koltermann C.E., Gorelick S.M. (1996). Heterogeneity in Sedimentary Deposits: A Review of Structure-imitating, Process-imitating and Descriptive Approaches. *Water Resources Research*.

Lake L.W., Srinivasan S. (2004). Statistical Scale-up of Reservoir Properties: Concepts and Applications. *Journal of Petroleum Science and Engineering*.

Leister H.J., Peric M. (1994). Vectorized Strongly Implicit Solving Procedure for a Seven-Diagonal Coefficient Matrix. *International Journal of Numerical Methods for Heat & Fluid Flow*.

Leung J.Y., Srinivasan S. (2011). Analysis of Uncertainty Introduced by Scale up of Reservoir Attributes and Flow Response in Heterogeneous Reservoirs. *Society of Petroleum Engineers*.

Leung J.Y. (2009). Reservoir Modeling Accounting for Scale-Up of Heterogeneity and Transport Processes. *PhD Thesis, University of Texas*.

Liseikin V.D. (2010). Grid Generation Methods. *Book, Springer, Second Edition*.

Mallison B.T., Chen Y. (2006). Non-linear Two Point Flux Approximations for Simulating Subsurface Flows with Full Tensor Anisotropy. *Springer, Computational Geosciences*.

Manchuk J. (2010). Geostatistical Modeling of Unstructured Grids for Flow Simulation. *PhD thesis, University of Alberta.*

McKinley J.M., Lloyd C.D., Ruffell A.H. (2004). Use of Variography in Permeability Characterization of Visually Homogeneous Sandstone Reservoirs With Examples From Outcrop Studies. *Mathematical Geology.*

Müller Ch., Siegesmund S., Blum Ph. (2010). Evaluation of the Representative Elementary Volume (REV) of a Fractured Geothermal Sandstone Reservoir. *Environmental Earth Sciences.*

Mustapha H. (2010). G23FM: a tool for meshing complex geological media. *Springer.*

Nachabe M.H., Morel H.J. (1999). Scaling the Ground Water Flow Equation. *Journal of Hydrology.*

Netinger B. (1994). The Effective Permeability of a Heterogeneous Porous Medium. *Transport in Porous Media.*

Nordahl K., Ringrose P.S., Wen R. (2005). Petrophysical Characterization of a Heterolithic Tidal Reservoir Interval Using a Process-based Modelling Tool. *Petroleum Geoscience.*

Nordahl K., Ringrose P.S. (2008). Identifying the Representative Elementary Volume for Permeability in Heterolithic Deposits Using Numerical Rock Models. *Springer, Mathematical Geosciences.*

Ozdemir M., Ozguc A.F. (1997). Porosity Variation and Determination of REV in porous Medium of Screen Meshes. *International Communications in Heat and Mass Transfer.*

Persson P., Strang G. (2004). A Simple Mesh Generator in MATLAB. <http://persson.berkeley.edu/distmesh/>.

Peter I., Gedeon D. (1991). Upscaling of Permeability of Heterogeneous Formations. Part 1: General Approach and Application to Isotropic Media. *Society of Petroleum Engineers*.

Pickup G.E. (1994). Geology, Geometry, and Effective Flow. *Society of Petroleum Engineers*.

Quintard, M. (1989). Two Phase Flow in Heterogeneous Porous Media: The Method of Large Scale Averaging Applied to Laboratory Experiments in a Stratified System, *Society of Petroleum Engineers*.

Razavi S.F., Boisvert J., Leung J. (2011). Unstructured Grid Generation in 2D and 3D. *Paper 213, CCG Annual Report 13, University of Alberta*.

Razavi S.F., Leung J., Boisvert J. (2011). Flow Simulation on Unstructured Grid Generation. *Paper 214, CCG Annual Report 13, University of Alberta*.

Ringrose P.S. et al (2012). Multiscale Geological Reservoir Modelling in Practice. *Statoil Research Center*.

Falgout R.D., Yang U.M. (2002). Hypre: A Library of High Performance Preconditioners.

Rooji G.H. (2008). Averaging Hydraulic Head, Pressure Head, and Gravitational Head in Subsurface Hydrology, and Implications for Averaged Fluxes, and Hydraulic Conductivity. *Hydrology and Earth System Sciences*.

Si H. (2006). A Quality Tetrahedral Mesh Generator and Three-Dimensional Delaunay Triangulator. <http://tetgen.berlios.de/>.

Sorek S., Ronen D., Gitis V. (2010). Scale-dependent Macroscopic Balance Equations Governing Transport Through Porous Media: Theory and Observations. *Transport in Porous Media*.

Stanley C. Eisenstat, Howard C. Elman, Martin H. Schlutz, Yale U. (1988). Block-Preconditioned Conjugate-Gradient-Like Methods for Numerical Reservoir Simulation. Society of Petroleum Engineers.

Stone H.L. (1968). Iterative Solution of Implicit Approximations of Multidimensional Partial Differential Equations. *SIAM Journal on Numerical Analysis*.

Thompson K.E. (2002). Fast and Robust Delaunay Tessellation in Periodic Domains. *Wiley Publication*.

Vazquez, J.L. (2007). The Porous Medium Equation: Mathematical Theory. *Oxford University Press*.

Vogel J.R., Brown G.O. (2003). Geostatistics and the Representative Elementary Volume of Gamma Ray Tomography Attenuation in Rock Cores. *The Geological Society of London*.

Watts III, James W. (1981). A Conjugate Gradient-Truncated Direct Method for the Iterative Solution of the Reservoir Simulation Pressure Equation. *Society of Petroleum Engineers*.

Weinstein H.G., Stone H.L., Kwan T.V. (1969). Iterative Procedure for Solution of Systems of Parabolic and Elliptic Equations in Three Dimensions. *Esso Company, Houston, Texas*.

Wellman T.P., Poeter E.P. (2005). Estimating Spatially Variable Representative Elementary Scales in Fractured Architecture Using Hydraulic Head Observations. *Water Resources Research*.

Worthington P.F. (1993). Effective Integration of Core and Log Data. *Marine and Petroleum Geology*.

Worthington P.F. et al (2004). The Effect of Scale on the Petrophysical Estimation of Intergranular Permeability. *Society of Petrophysicists and Well-Log Analysts*.

Yong Z. (2004). Upscaling Conductivity and Porosity in Three-dimensional Heterogeneous Porous Media. *Chinese Science Bulletin*.

Zhang D. et al (2000). Pore Scale Study of Flow in Porous Media: Scale Dependency, REV, and Statistical REV. *Geophysical Research Letters*.